

Doctorate Dissertation

Magnetohydrodynamic Simulation Study
on Fast Magnetic Reconnection

磁気リコネクションの高速化機構に関する
電磁流体力学シミュレーション研究

Takuya Shibayama

柴山 拓也

Graduate School of Science,
Division for Integrated Studies,
Institute for SpaceEarth Environmental Research,
Nagoya University

Supervisor: Dr. Kanya Kusano

1 Abstract

Magnetic reconnection is a fundamental process of energy conversion in astronomical, space, and laboratory plasmas. Magnetic reconnection changes the connectivity of a magnetic field and converts magnetic energy into kinetic and thermal energy. Fast magnetic reconnection is necessary to explain the explosive energy release occurring during solar flares, magnetospheric substorms, and tokamak plasma disruptions. The speed of the energy conversion is measured by magnetic reconnection rate M , which is a non-dimensional number given by normalizing the inflow velocity V_{in} with the upstream Alfvén velocity V_A , $M = V_{in}/V_A$. The necessary magnetic reconnection rate to explain various phenomena is on the order of 0.01. One of the goals of magnetic reconnection theory is to explain this reconnection rate.

The Sweet-Parker and Petschek models are well-established magnetohydrodynamics (MHD) models of 2D steady magnetic reconnection. The Sweet-Parker reconnection rate, however, is too low to explain solar flares because the electric resistivity η in the solar corona plasma is very low, in other words, Lundquist number $S = LV_A/\eta$ is very large such as 10^{12} , where L is the size of the system. The predicted reconnection rate M_{SP} of Sweet-Parker model is the inverse square root of Lundquist number $M_{SP} = S^{-1/2}$, which is very small in the solar corona. Petschek model can explain fast magnetic reconnection supported by a small diffusion region and energy conversion occurring within slow-mode MHD shock layers. The predicted reconnection rate is almost independent on Lundquist number. In systems with uniform resistivity, however, it is pointed out that Petschek model has difficulty in maintaining the small diffusion region. It is, therefore, unclear whether the Petschek model is applicable in plasmas with uniform resistivity.

For non-steady case, magnetic reconnection with plasmoids is considered to be a fruitful model of MHD fast reconnection under uniform resistivity. Long current sheets are divided into several secondary current sheets by closed magnetic field structures, or plasmoids, due to tearing instability. If there are sufficient number of plasmoids, the intervening Sweet-Parker diffusion region can accommodate fast reconnection. For this reason, plasmoid magnetic reconnection is based on the Sweet-Parker reconnection model.

In this research, we investigate the other possible fast reconnection scenario, non-steady Petschek-type reconnection. We conduct a series of MHD numerical simulations of large scale magnetic reconnection region and point out that Petschek-type small diffusion regions spontaneously appear in the dynamic evolution of plasmoid reconnection even under uniform resistivity. This regime appear especially when Lundquist number is larger than some threshold. The reconnection rate is almost independent on Lundquist number. The detailed mechanism of the formation of the Petschek-type diffusion regions is, however, poorly understood partly because the evolution of the system is highly dynamic, and to fully develop this theory it is necessary to uncover the mechanism of the formation of Petschek-type reconnection regions

under nonlinear evolution.

In order to solve the problem, we construct a model of the elementary process of the Petschek-type diffusion region formation. We successfully find an initial condition to reproduce a single Petschek-type diffusion region associated with a plasmoid. We find that the separation of the magnetic null point and flow stagnation point plays an important role in localizing Petschek-type diffusion region. The reconnection rate is independent on Lundquist number because the similar diffusion-scale process realize in systems with different Lundquist number. According to these results, we propose the *dynamical Petschek reconnection* regime, in which small Petschek-type diffusion regions appear in close contact with the ends of plasmoids and drive fast reconnection.

We furthermore discuss the application of this study to the reconnection process of solar flares. For the comparison between solar flare observation and our reconnection model, it is important to understand observational effects and three-dimensional effects. Some of the diagnosis of solar flares are conducted using spectroscopic observations of emission lines of ionized Fe ions. We solve ionization equation together with MHD equation and pointed out that there is a threshold of plasmoid area under which we can not use an assumption of ionization equilibrium. In addition, we point out an possibility of new method to infer the history of plasma heating in the era of next-generation satellite. We also perform three-dimensional MHD simulation of current sheet and reconfirm that oblique tearing instability dominate the system. We do not find the evolution of Petschek-type diffusion region in the 3D current sheet. However, the Lundquist number of the three-dimensional simulation is smaller than that of two-dimensional models due to the limitation of computational power. If the separation of reconnection point and flow stagnation point sufficiently evolve in a larger system, it is possible that the motion of X-point is restricted and the diffusion region is localized in the same way as two-dimensional case.

Contents

1	Abstract	2
2	Introduction	6
2.1	Magnetic Reconnection in the Solar Corona	6
2.2	Governing Equations	9
2.3	Static Diffusion of Magnetic Field	10
2.4	2D Steady Models of Magnetic Reconnection	10
2.4.1	Sweet-Parker Reconnection Model	12
2.4.2	Petschek Reconnection Model	13
2.5	2D Non-Steady Model of Magnetic Reconnection	17
2.6	Motivation of this study	18
3	Method	22
3.1	Numerical Scheme	22
3.2	Initial Condition	23
3.3	Boundary Condition	23
4	Global Model	26
4.1	Model	26
4.2	Result	27
4.3	Discussion	32
5	Local Model	34
5.1	Model	34
5.2	Results	35
5.3	Discussion on Local Model	39
5.4	Conclusion of Local Model	43
6	Simulated Observation	44
6.1	Ionization Equation	44
6.2	Ionization Equilibrium	44
6.3	Time Dependent Ionization	46
6.4	Solar-C_EUVST	48
6.5	Governing Equations and Numerical Method	49
6.6	Initial Condition and Normalization	50
6.7	Results and Discussion	52

7	3D Models	56
7.1	Introduction to 3D Magnetic Reconnection	56
7.2	Simulation Settings	58
7.3	Results and Discussions	59
8	Discussion	65
8.1	Scenario of Dynamical Petschek Reconnection	65
8.2	Observation of Magnetic Reconnection in the Solar Corona	67
9	Conclusion	69

2 Introduction

2.1 Magnetic Reconnection in the Solar Corona

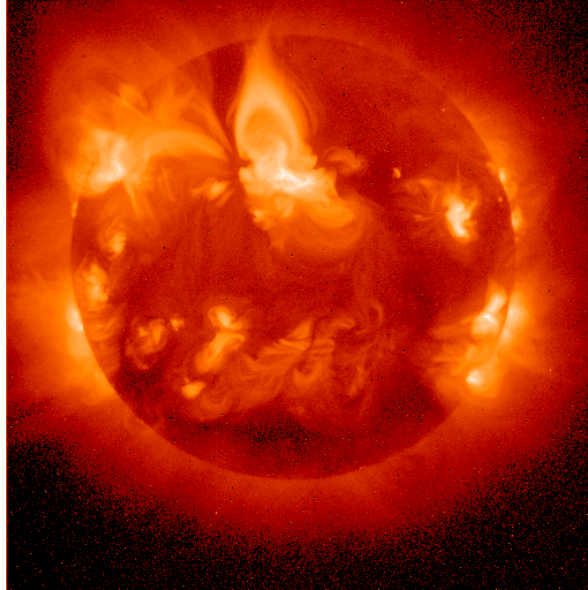


Figure 2.1: Solar corona observed with X-ray.

Solar corona, the outer atmosphere of the Sun, is filled with thin million-Kelvin plasma. Solar flares are sporadic explosions in the solar corona which causes sudden increase in brightness in a wide wavelength range from infrared to X-ray. Solar flare is caused by magnetic reconnection of strong magnetic field around active region and generate high temperature plasma of a few tens of million Kelvin. Fig.2.1 shows an X-ray image of the Sun and solar flare observed by Japanese solar X-ray satellite “Yhokho”, in which the solar flare is seen as a cusp-shaped structure at the center of the upper hemisphere. The structure of the solar flare is modeled as shown in Fig.2.2, which is referred as CSHKP model. The thin solid lines represents magnetic field lines, which exhibit magnetic reconnection at the cross point. The closed, circular-shaped magnetic field structure above the reconnection point is referred as a plasmoid in a two-dimensional system, and a flux rope in a three-dimensional system. The lower loop-like structure is post flare loop and the foot point of the loop at the solar surface is called flare ribbons. Fig.2.1 observes bright post flare loop filled with high temperature plasma.

Several research groups conduct quantitative measurements of magnetic reconnection of solar flares. Yokoyama et al. (2001) obtains inflow velocity by measuring the inflowing plasma feature to the reconnection point, which corresponds to obtaining V_{in} in Fig.2.2. The results are shown in Fig.2.3 in which the right panel shows the temporal variation of the plasma

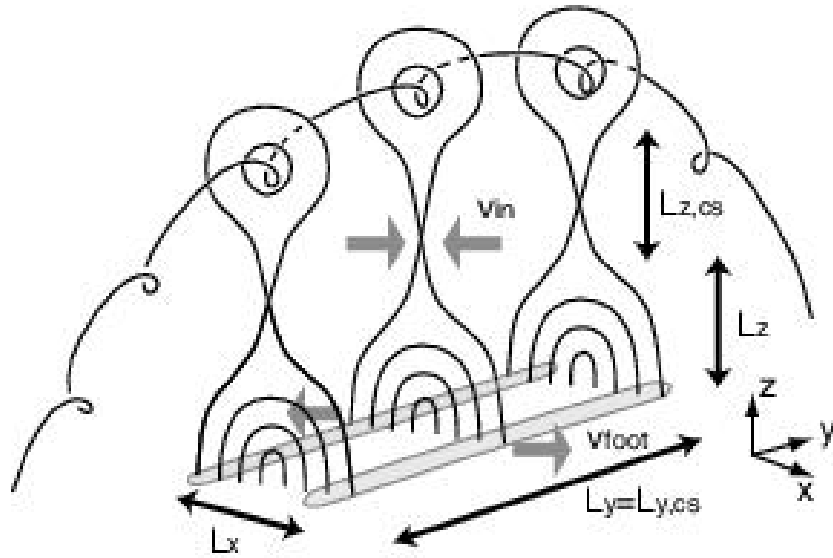


Figure 2.2: CSHKP flare model in three-dimensional space (Isobe et al., 2005).

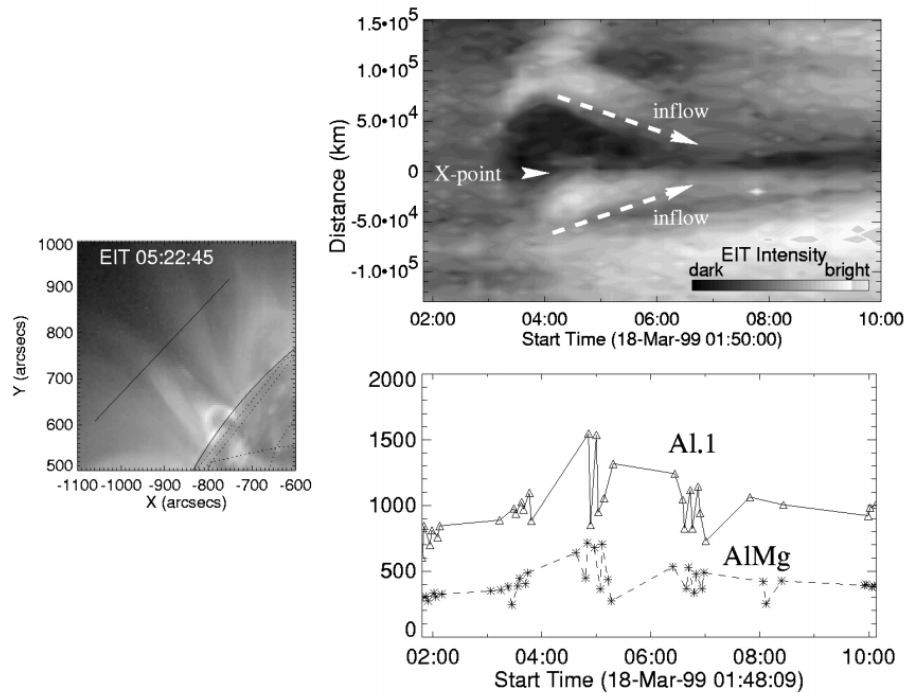


Figure 2.3: Observation of inflow feature to the reconnection region (Yokoyama et al., 2001).

structure at the virtual slit shown in the left panel. They show the Alfvén Mach number of the inflow, or reconnection rate, ranges from 0.001 to 0.03. Isobe et al. (2005) derived

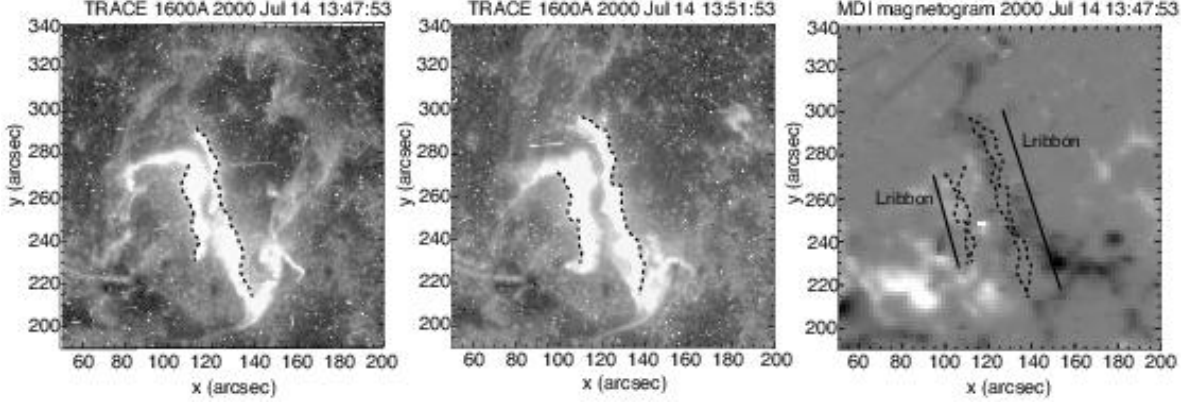


Figure 2.4: Apparent motion of flare ribbons (Isobe et al., 2005).

magnetic flux by observing the apparent motion of flare ribbons, which corresponds to V_{foot} in Fig.2.2. It is seen from Fig.2.4 that the interval between the flare ribbons increase as the solar flare evolve. The reconnected magnetic flux is derived by integrating magnetic field strength between flare ribbons in the beginning and the at end of the flare. They observed several flare events and the derived reconnection rate ranges from 0.015 to 0.071. Both of these studies show the reconnection rate of the solar flare is on the order of 0.01.

In the solar corona, the energy density of the magnetic field, magnetic pressure $p_m = B^2/(8\pi)$, is typically larger than the thermal energy density, plasma pressure p , by orders of magnitudes. The ratio of these two energy densities is called plasma beta $\beta = (8\pi p)/B^2$. If magnetic reconnection happens in a low-beta plasma like in the solar corona, thermal pressure suddenly goes up and explosive phenomenon happen. The typical fluid parameters of solar corona in the inflow region is shown in Tab.1. Bottom five parameters are calculated from top four parameters. Here, we use the following constants: proton mass $m_e = 1.7 \times 10^{-24}g$, Boltzman constant $k_B = 1.4 \times 10^{-16}erg/K$ and assume that the equation of state of an ideal gas is applicable.

Assuming the Spitzer conductivity, electric resistivity η is given as the following(Aschwanden, 2004),

$$\eta = \frac{1}{\sigma} \quad (2.1)$$

$$\sigma = \frac{n_e e^2}{m_e \nu_e} \approx 6.96 \times 10^7 \ln(\Lambda)^{-1} Z^{-1} T_e^{3/2}. \quad (2.2)$$

The typical value of η in the solar corona is

$$\eta \approx 3 \times 10^{-16}, \quad (2.3)$$

Physical quantities	Typical value
Magnetic field strength	10 <i>G</i>
Density	10 ⁹ #/ <i>cm</i> ³
Length scale of reconnection region	10 ⁷ <i>cm</i>
Plasma beta	0.05
Alfven velocity	10 ⁸ <i>cm/s</i>
Alfven time	0.5 <i>s</i>
Magnetic pressure	4 <i>dyn/cm</i> ²
Gas pressure	0.1 <i>dyn/cm</i> ²
Temperature	10 ⁶ <i>K</i>

Table 1: Typical parameter of inflow region of solar flare.

where $\ln(\Lambda) \approx 20$, $Z = 1$, $T_e \approx 10^6$ are used. As a result, the Lundquist number S is

$$S = \frac{4\pi}{c^2} \frac{LV_A}{\eta} \approx 3 \times 10^{13}, \quad (2.4)$$

where we assume $L \approx 10^9 \text{cm}$, $V_A \approx 10^8 \text{cm/s}$. Lundquist number S is a non-dimensional parameter and often used to characterize reconnecting current sheets.

2.2 Governing Equations

Theoretical studies of magnetic reconnection have been conducted to explain the reconnection rate and the timescale of reconnection events. One of the important goal of theoretical studies is to explain the reconnection rate of 0.01. There are many approaches to this problem including MHD (Magnetohydro dynamic), kinetic, two fluid, extended MHD and so on. The governing equations we use in this study are the following compressible resistive MHD equations.

$$\frac{\partial \rho}{\partial t} + \nabla \cdot (\rho \mathbf{V}) = 0 \quad (2.5)$$

$$\rho \frac{d\mathbf{V}}{dt} = -\nabla p + \frac{1}{c} \mathbf{J} \times \mathbf{B} \quad (2.6)$$

$$\frac{\partial \mathbf{B}}{\partial t} = -c \nabla \times \mathbf{E} \quad (2.7)$$

$$\frac{d}{dt} \left(\frac{p}{\rho^\gamma} \right) = \frac{(\gamma - 1)}{\rho^\gamma} \eta J^2 \quad (2.8)$$

$$\nabla \cdot \mathbf{B} = 0 \quad (2.9)$$

$$\mathbf{E} = -\frac{1}{c} \mathbf{V} \times \mathbf{B} + \eta \mathbf{J} \quad (2.10)$$

$$\mathbf{J} = \frac{c}{4\pi} \nabla \times \mathbf{B} \quad (2.11)$$

2.3 Static Diffusion of Magnetic Field

As the initial trial to quantitatively evaluate magnetic reconnection, a static ($\mathbf{V} = 0$) model is developed. We will estimate how long the magnetic reconnection process take. Eq.2.10 becomes $\mathbf{E} = \eta\mathbf{J}$ and Eq.2.7 is rewritten as follows:

$$\frac{\partial \mathbf{B}}{\partial t} = -c\nabla \times \mathbf{E} = \frac{c^2}{4\pi}\eta\nabla \times \nabla \times \mathbf{B} = \frac{c^2}{4\pi}\eta\nabla^2\mathbf{B}. \quad (2.12)$$

The evolution of magnetic field is, therefore, follows the diffusion equation. The typical timescale τ_{diff} of this diffusion process is

$$\tau_{\text{diff}} \sim \frac{4\pi}{c^2} \frac{\delta^2}{\eta} \text{ sec}, \quad (2.13)$$

where δ denotes the thickness of the current layer. Using the typical values of the solar corona, $\eta = 3 \times 10^{-16}$, $\delta = 100$ km, $\tau_{\text{diff}} \sim 4 \times 10^9\text{s} = 100\text{year}$, which is too long compared with the timescale of solar flares. Accordingly, the static diffusion cannot explain energy conversion process of solar flares.

2.4 2D Steady Models of Magnetic Reconnection

The next possible model is 2D steady ($\partial/\partial z = \partial/\partial t = 0$) model.

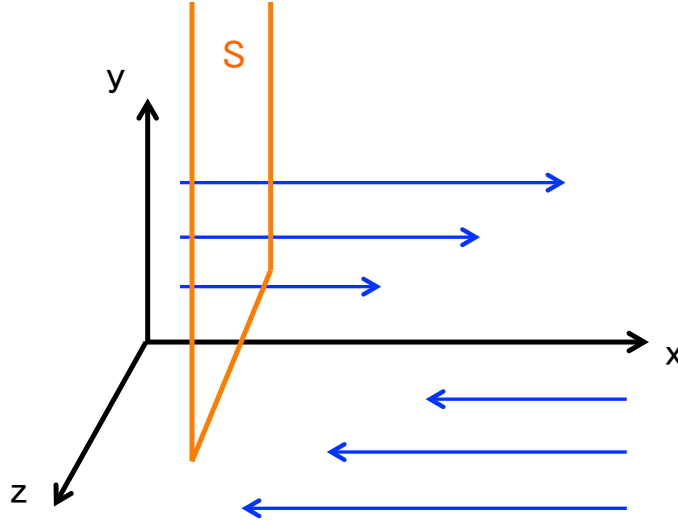


Figure 2.5

Suppose there is magnetic field with only x -component which is a function of y and changes its sign at $y = 0$. The $x - z$ plane is called neutral plane. The total magnetic flux Φ in the $y > 0$ region is calculated by the surface integral of \mathbf{B} on the closed surface S .

$$\Phi = \int_S \mathbf{B} \cdot d\mathbf{s}. \quad (2.14)$$

The temporal evolution of Φ is derived using Eq.2.7 along with Gauss's theorem (divergence theorem) as a line integral along δS , the edge of S as follows:

$$\frac{\partial \Phi}{\partial t} = \int_S \frac{\partial \mathbf{B}}{\partial t} \cdot d\mathbf{s} = - \int_S c \nabla \times \mathbf{E} \cdot d\mathbf{s} \quad (2.15)$$

$$= - \int_{\delta S} c \mathbf{E} \cdot d\mathbf{l}. \quad (2.16)$$

As a result of symmetry in z direction and the infinitesimally far boundary of S in $y \rightarrow \infty$, the evolution of Φ is

$$\frac{\partial \Phi}{\partial t} = c E_z. \quad (2.17)$$

In addition, $\mathbf{E} = \eta \mathbf{J}$ at reconnection point, which leads to the fact that we can measure the reconnected magnetic flux in a unit time by measuring J_z at the reconnection point.

From Eq.2.7,

$$\frac{\partial}{\partial t} \begin{pmatrix} B_x \\ B_y \end{pmatrix} = -c \begin{pmatrix} \frac{\partial E_z}{\partial y} \\ -\frac{\partial E_z}{\partial x} \end{pmatrix} = \begin{pmatrix} 0 \\ 0 \end{pmatrix}. \quad (2.18)$$

Accordingly, E_z is spatially uniform, which means we can acquire the value of reconnected magnetic flux by measuring $\mathbf{E} = -1/c \mathbf{V} \times \mathbf{B} + \eta \mathbf{J}$ at some point when we assume two dimensional steady system. It is easier to measure the electric field in the inflow region, $\simeq \mathbf{V} \times \mathbf{B} \simeq B_{in} V_{in}$, than in at the reconnection point or neutral line, which are just a point or line. For a comparison of magnetic reconnection in different system with different magnetic field strength or density, it is convenient to normalize the electric field with typical value of each system. Let us define normalized magnetic reconnection rate M as motional electric field in the inflow region $\mathbf{V} \times \mathbf{B}$ divided by the magnetic field strength and Alfvén velocity in the inflow region $B_{in} V_{Ain}$, which is a practical upper limit of the electric field. Normalized reconnection rate is identical to the Alfvén Mach number in the inflow region.

$$M = \frac{B_{in} V_{in}}{B_{in} V_{Ain}} = \frac{V_{in}}{V_{Ain}}. \quad (2.19)$$

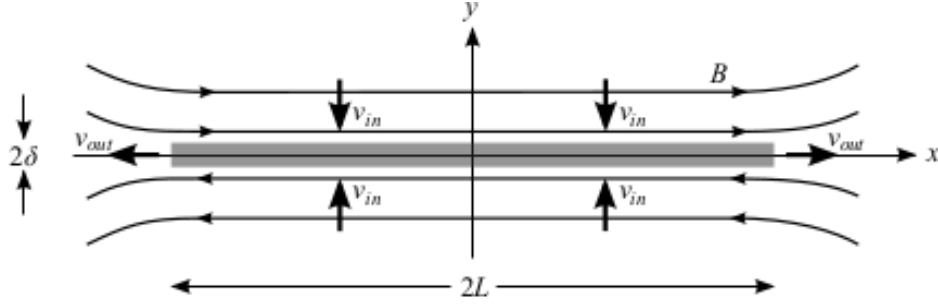


Figure 2.6: Spatial structure of Sweet-Parker model (figure from [Comisso and Asenjo \(2014\)](#))

2.4.1 Sweet-Parker Reconnection Model

The first successful 2D steady reconnection model is the Sweet-Parker model proposed by [Sweet \(1958\)](#); [Parker \(1957\)](#). Fig.2.6 illustrates the schematic picture of Sweet-Parker current sheet ([Comisso and Asenjo, 2014](#)) in which gray shaded area is called diffusion region where strong electric current in the out-of-plane direction is flowing. The inflow V_{in} flows into the diffusion region from $\pm y$ directions and outflow goes to $\pm x$ directions. In the inflow region ($y \gg 1$) the electric current is negligible and the first term is larger compare to the second term in the z -component of the right-hand side of Eq.2.10, while second term is dominant in the diffusion region. As z -component of the electric field is spatially uniform, from z -component of Eq.2.10 we get,

$$V_{in} B_x \sim \frac{c^2}{4\pi} \eta \frac{B_x}{\delta}. \quad (2.20)$$

Solving this for δ ,

$$\delta \sim \frac{c^2}{4\pi} \frac{\eta}{V_{in}}. \quad (2.21)$$

From mass conservation law in an assumption of incompressibility,

$$L V_{in} = \delta V_{out}. \quad (2.22)$$

Eliminating δ from Eqs.2.21, 2.22 and solving for V_{in} , we get

$$V_{in} = \sqrt{\frac{c^2}{4\pi} \frac{\eta V_{out}}{L}}. \quad (2.23)$$

The outflow velocity V_{out} can be derived from the acceleration process in the diffusion region. After entering at the center of the diffusion region, plasma is accelerated up to V_{out} by Lorentz force $(\mathbf{J} \times \mathbf{B})_x$.

$$(\mathbf{J} \times \mathbf{B})_x = J_z B_y \quad (2.24)$$

$$\approx \frac{c}{4\pi} \frac{B_x B_y}{\delta} \quad (2.25)$$

The total work by the Lorentz force is equal to the kinetic energy of the outflow plasma:

$$\frac{c}{4\pi} \frac{B_x B_z}{\delta} L = \rho V_{out}^2 \quad (2.26)$$

$$V_{out} = \sqrt{\frac{c}{4\pi} \frac{B_x B_z L}{\rho \delta}}. \quad (2.27)$$

As we can approximate $B_x/L \approx B_z/\delta$ from $\nabla \cdot \mathbf{B} = 0$,

$$V_{out} \approx \sqrt{\frac{c}{4\pi} \frac{B_x^2}{\rho}} = V_{Ain}. \quad (2.28)$$

From Eqs.2.23, 2.28 we get

$$M = \frac{V_{in}}{V_{Ain}} = \sqrt{\frac{c^2}{4\pi} \frac{\eta}{LV_{Ain}}} = S^{-\frac{1}{2}}, \quad (2.29)$$

where $M = V_{in}/V_{Ain}$ is the normalized reconnection rate and

$$S = \frac{4\pi}{c^2} \frac{LV_{Ain}}{\eta} \quad (2.30)$$

is Lundquist number. Accordingly, we can conclude that reconnection rate is determined only by the system size L when we fix the upstream plasma parameter and electric resistivity. As the typical Lundquist number in the solar corona is $S \sim 10^{14}$, typical magnetic reconnection rate is $M \sim 10^{-7}$, which much smaller than that of solar flares. Consequently, Sweet-Parker model cannot explain fast magnetic reconnection in the solar corona. Using Eqs.2.22, 2.29 we get

$$M = \frac{V_{in}}{V_{Ain}} = S^{-\frac{1}{2}} = \frac{\delta}{L}, \quad (2.31)$$

which means the reconnection rate is determined by δ and L . The ratio between two values L/δ is called aspect ratio, whose inverse is equal to the reconnection rate.

2.4.2 Petschek Reconnection Model

Petschek proposed another steady reconnection model (Petschek, 1964) to explain fast reconnection in high Lundquist number systems, which is not possible by Sweet-Parker model. The reason why Sweet-Parker model has difficulty is the following. In order to keep fast

reconnection in a steady state, large amount of magnetic flux should be transported to the diffusion region by the sufficiently large inflow. This magnetic flux have to be compensated in the diffusion region, which is done by diffusion process in Sweet-Parker model. In a high Lundquist number system, however, the speed of diffusion is slow (see Fig.2.7(a)). In the Petschek model they introduce wave propagation process which is faster than the diffusion process and solve this difficulty (Fig.2.7(b)). In this case, slow mode MHD shock layers form at the wave front, where the magnetic field lines bent in Fig.2.7(b).

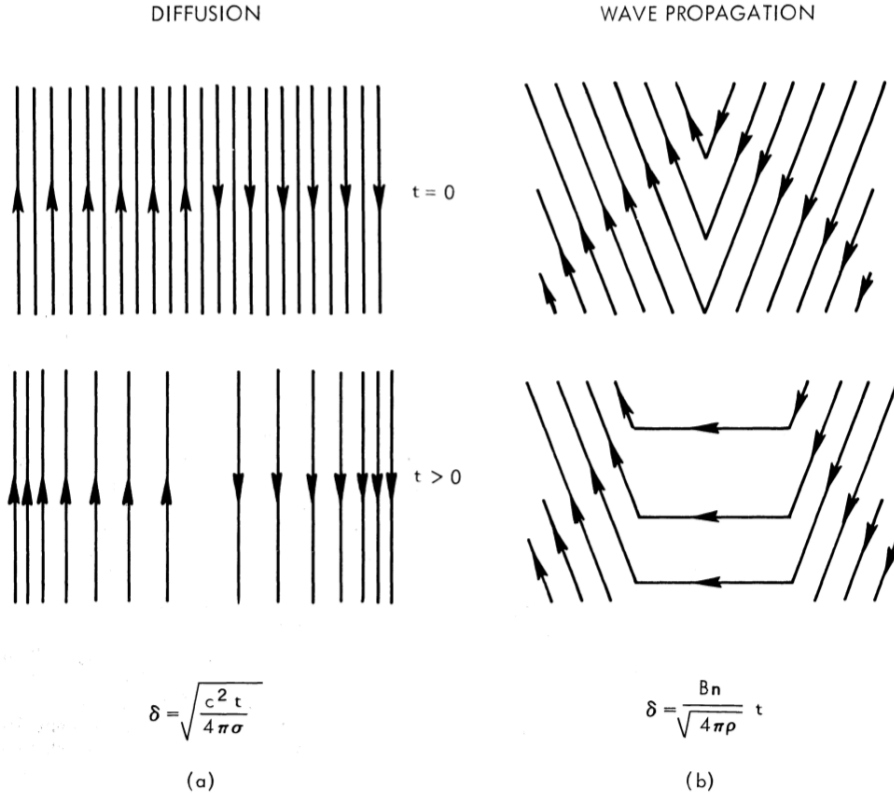


Figure 2.7: Difference of the propagation speeds (Petschek, 1964).

Fig.2.8 illustrates the structure around the diffusion region of Petschek model. The dashed lines shows the slow mode shock layers. In the Sweet-Parker model, all the outflow plasma pass the diffusion region and get accelerated, while in the Petschek model it's only a part of plasma and the rest goes through the slow shocks. Balancing the upward wave propagation speed and inflow speed to keep steady state, we get

$$V_{in} = \frac{B_y}{\sqrt{4\pi\rho}}. \quad (2.32)$$

The reason that Petschek model has larger reconnection rate can be understood from

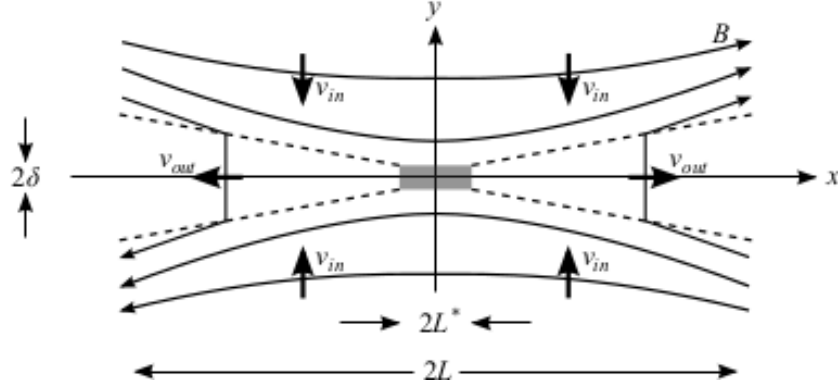


Figure 2.8: Structure of Petschek model. (Comisso and Asenjo, 2014)

Eq.2.22, which describes conservation of mass flowing into and out of the diffusion region. V_{out} in the right-hand side is constant according to Eq.2.28, which makes it difficult to increase the mass flux. Accordingly, V_{in} and magnetic reconnection rate are small in Sweet-Parker model. By contrast in Petschek model, plasma can be accelerated out of the constraint of Eq.2.22, without passing through the diffusion region.

Let us now estimate reconnection rate of Petschek model. The structure of gray-shaded diffusion region is similar to the one of Sweet-Parker mode, but the length of that L^* is shorter than that in Sweet-Parker model L . As we discussed with Eq.2.31, reconnection rate is inversely proportional to the aspect ratio of diffusion region. Therefore, reconnection rate increase when the length of the diffusion region is short. The reconnection rate corresponding to the aspect ratio δ/L^* is

$$M = \frac{\delta}{L^*} = \frac{L}{L^*} \frac{\delta}{L}, \quad (2.33)$$

which means as the diffusion region is shorten, reconnection rate goes up being proportional to L/L^* . L^* is treated as a free parameter in Petschek (1964) and the lower limit of L^* is discussed based on the criteria that electric current of slow mode shock does not significantly weaken the magnetic field in the inflow region as follows:

$$L^* > \frac{L}{S} (\ln S)^2. \quad (2.34)$$

Now the upper limit of reconnection rate is

$$M = \frac{V_{in}}{V_{Ain}} = \frac{1}{\ln S}. \quad (2.35)$$

This reconnection rate is often referred as a reconnection rate of Petschek model. However, this is just an upper limit and it is not appropriate to compare this value with Sweet-Parer

reconnection rate. The reconnection rate should be derived from Eq.2.33 with some other constraint on L^* . It is not discussed in Petschek (1964) how to localize the diffusion region.

There is no mechanism in MHD equations to localize diffusion region. For numerical simulation of Petschek-type reconnection, therefore, some ad hoc approach such as anomalous resistivity (e.g. Ugai and Tsuda, 1977) or local forced inflow to a part of current sheet (e.g. Hayashi and Sato, 1978). Petschek-type reconnection is reproduced with numerical simulation by using these effects to localize diffusion region. These are, however, not self-consistent effects of MHD equations. Anomalous resistivity models effects of small scale interaction of electrons and ions (Yamada et al., 2010).

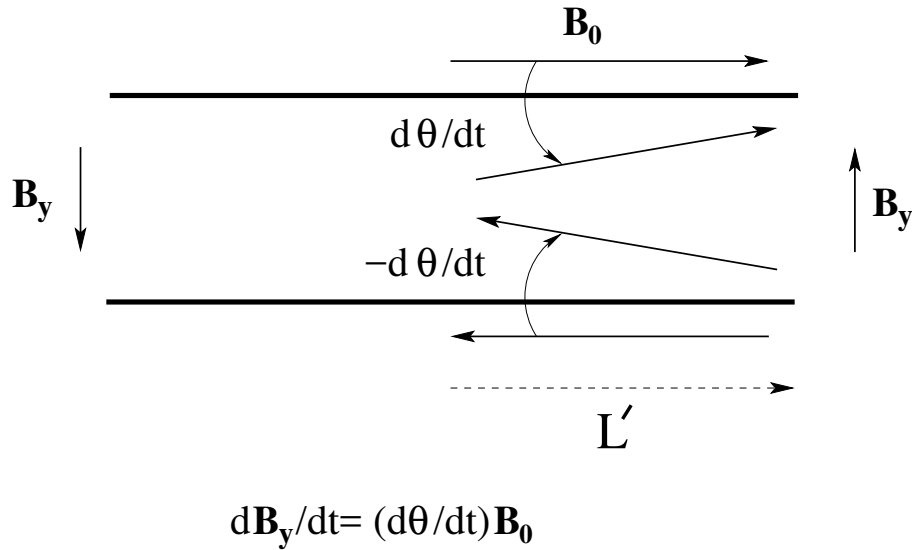


Figure 2.9: Generation process of cross field (B_y) in the diffusion region (Kulsrud, 2001).

Kulsrud (2001, 2011) discuss that Petschek model does not realize in spatially uniform electric resistivity. The reason is the following (See Fig.2.9). At the edge of diffusion region, there should be sufficiently large B_y for the connection of the solution in outflow region. This B_y component should be generated in the diffusion region. The constraint for L^* is derived from this requirement. The temporal evolution of B_y is described by the y -component of Eq.2.7:

$$\frac{\partial B_y}{\partial t} = -\partial_x(V_x B_y) + c\eta\partial_x J_z. \quad (2.36)$$

Here, $\partial_x(V_y B_x)$ term is negligible because V_y is small in the diffusion region. We can qualitatively understand this equation as follows; the second term in the right-hand side generate B_y by the gradient of J_z in the x direction, while the first term represents convection of B_y out of the diffusion region. In a steady state these two terms balance. Let us evaluate each term in a diffusion region. The first term in the right-hand side is $\partial_x(V_x B_y) \sim V_A B_y / L^*$, while the

second term is $c\eta\partial_x J_z \sim -V_{in}\partial_x B_x$ using Eqs.2.11, 2.20. Assuming upstream magnetic field B_x as the following function of x

$$B_x(x) = B_0 \left(1 - \frac{x^2}{L^2}\right), \quad (2.37)$$

$\partial_x B_x \sim -\frac{L^*}{L^2} B_0$. Then Eq.2.36 is rewritten

$$\frac{\partial B_y}{\partial t} \sim \frac{V_{in} L^{*2}}{L^* L^2} B_0 - B_y \frac{V_A}{L^*}. \quad (2.38)$$

In the steady state, this is equal to zero. Solving this for B_y we get

$$B_y = \frac{V_{in} L^{*2}}{V_A L^2} B_0. \quad (2.39)$$

With using Eq.2.32,

$$V_{in} = \frac{V_{in} L^{*2}}{V_A L^2} \frac{B_0}{\sqrt{4\pi\rho}} = V_{in} \frac{L^{*2}}{L^2}, \quad (2.40)$$

which results in

$$L^* = L. \quad (2.41)$$

Consequently, the length of the diffusion region L^* and the system size L must be the same, which is Sweet-Parker reconnection. This is the discussion in [Kulsrud \(2001\)](#), which shows Petschek model does not realize under uniform resistivity and steady state. The important assumption in their discussion is, however, the upstream profile of B_x (Eq.2.37). If the profile is different, the result is different. Especially when the profile is steeper, we have shorter diffusion region, which may support realization of Petschek model.

2.5 2D Non-Steady Model of Magnetic Reconnection

Apart from steady model, non-steady models are considered in this section. Harris-type equilibrium current sheet is unstable to tearing instability under a certain condition ([Furth et al., 1963](#)). [Tajima and Shibata \(1997\)](#); [Loureiro et al. \(2007\)](#) derived the scalings of the largest growth rate ω_{max} and largest growth wavelength λ of tearing instability as follows,

$$\omega_{max} \sim \tau_A^{-1} R_m^{1/4} \quad (2.42)$$

$$\frac{\lambda}{L} = 2\pi R_m^{-3/8}. \quad (2.43)$$

[Samtaney et al. \(2009\)](#) reproduces this relation using numerical simulation. [Shibata and Tanuma \(2001\)](#) discusses a repeated occurrence of tearing instability results in a fractal structure with smaller scale current sheet. When a current sheet becomes short and thin enough,

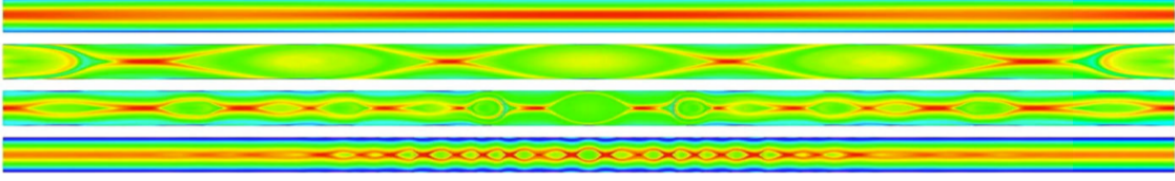


Figure 2.10: [Samtaney et al. \(2009\)](#)

kinetic or collisionless physics accelerate reconnection process.

Current sheets whose Lundquist number is larger than $\sim 10^4$ is unstable to tearing instability. This value is referred as a critical Lundquist number of tearing instability $S_c \sim 10^4$. According to Sweet-Parker model, reconnection rate M of a diffusion region with $S = S_c$ is $M = S^{-1/2} \sim 0.01$, which is high enough to explain explosive energy conversion during solar flares. Consequently, it is believed that even if Lundquist number of a current sheet is large $S > 10^4$, tearing instability breaks the current sheet into shorter ones and the local Lundquist number can become as small as S_c , which results in fast reconnection. [Bhattacharjee et al. \(2009\)](#) conducted a numerical simulations of high-Lundquist-number current sheets in a highly non-linear phase and concluded that the reconnection rate does not follow Sweet-Parker scaling in high Lundquist number and saturate at ~ 0.01 . [Huang and Bhattacharjee \(2010\)](#) points out the same saturation continues at least up to $S = 3 \times 10^6$. Although they does not mention, the results of [Bhattacharjee et al. \(2009\)](#); [Huang and Bhattacharjee \(2010\)](#) show interesting structure of diffusion region. Figs.2.14(f), 2.12(c) show current density during reconnection, in which some of the current structures show asymmetric structure in horizontal direction, which is a similar to Petschek model rather than Sweet-Parker model. Whether this structure is related to Petschek model is, however, not discussed.

2.6 Motivation of this study

In this paper, we attempt to explain fast reconnection with Petschek-type diffusion region even under uniform resistivity. Tab.2 shows the relationship between reconnection models. Our model is corresponding to the bottom right part of the table. As we discussed in the preceding sections, Sweet-Parker model is possible but too slow in coronal parameter, while Petschek model is fast enough but difficult to realize under uniform resistivity. Although plasmoid reconnection is a potential mechanism of fast reconnection in the solar corona, the

	Diffusion region is elongated	Diffusion region is localized
Steady	Sweet-Parker	Petschek
Non-steady	Plasmoid	This work

Table 2: Matrix of reconnection regimes.

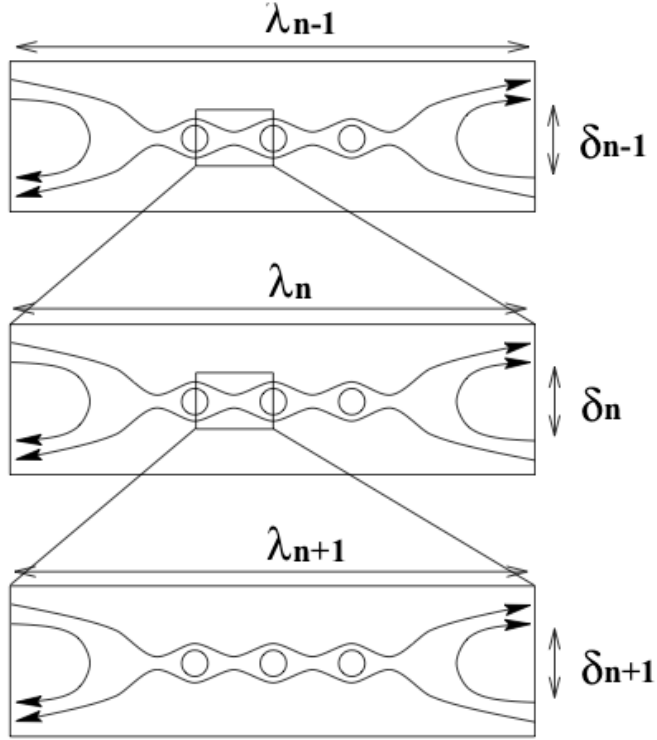


Figure 2.11: Fractal reconnection [Shibata and Tanuma \(2001\)](#)

diffusion region structure is not well understood in particular in high-Lundquist number and highly non-linear regime. We tackle the problem in the following ways.

- In [Sec.4](#), we elucidate whether the localized diffusion region structure in plasmoid reconnection is Petschek-type or not, and analyse the characteristics of reconnection process.
- A local model of the diffusion region is built in [Sec.5](#). We investigate the relation between flow and magnetic field structure in the formation process of localized diffusion region.
- Study for the comparison with observation of the solar corona is given in [Sec.6](#) and [Sec.7](#)

The physical model in this study is summarized in [Sec.3](#). The important parameter is the value and the spatial profile of electric resistivity, which is uniform in space in our model. The resistivity in resistive MHD system is a model of microscopic processes beyond MHD. In reality, it is possible to have anomalous resistivity and it is reported that such anomalous resistivity localizes the diffusion region and support fast reconnection with Petschek model (e.g. [Birn et al. \(2001\)](#)). It is, however, important to construct a fast reconnection model under uniform resistivity, which is a minimal model of reconnection system.

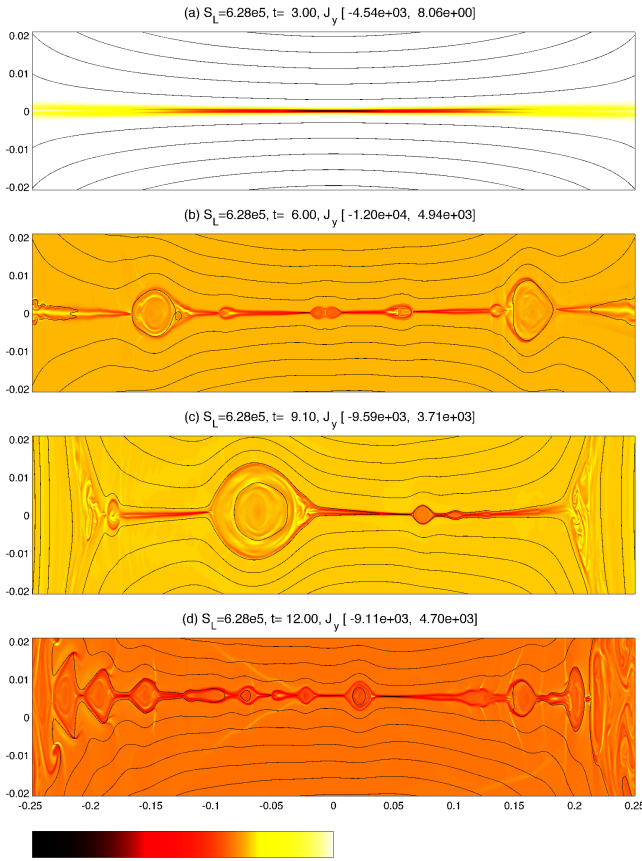


Figure 2.12: [Bhattacharjee et al. \(2009\)](#)

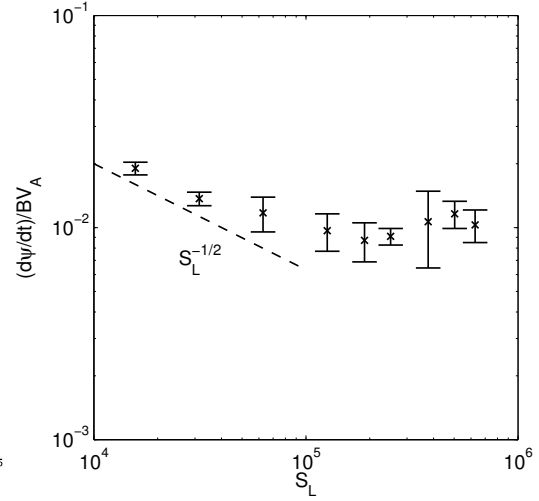


Figure 2.13: [Bhattacharjee et al. \(2009\)](#)

In the latter part of this paper, we investigate observational effect on magnetic reconnection study of the solar corona, which is a unique target of among other reconnection systems such as magnetotail or laboratory experiment. Laboratory experiment has a limitation for the system size because the plasma is generated in a vacuum chamber. Although the magnetotail does not have artificial limitation for the system size, the observations are conducted as a in-situ observations by small number of satellites. By contrast in the solar corona case, whole structure of large-scale current sheet and generated plasmoids are sometimes observed at once. Therefore, solar corona is a suitable target to study the interaction between processes in different scales. The problem of solar corona is, however, that the observation is conducted as remote sensing. The information is obtained from light emitted from ions and electrons with line-of-sight integration. It is important to understand processes such as ionization and three-dimensional structure formation for the interpretation of observational results.

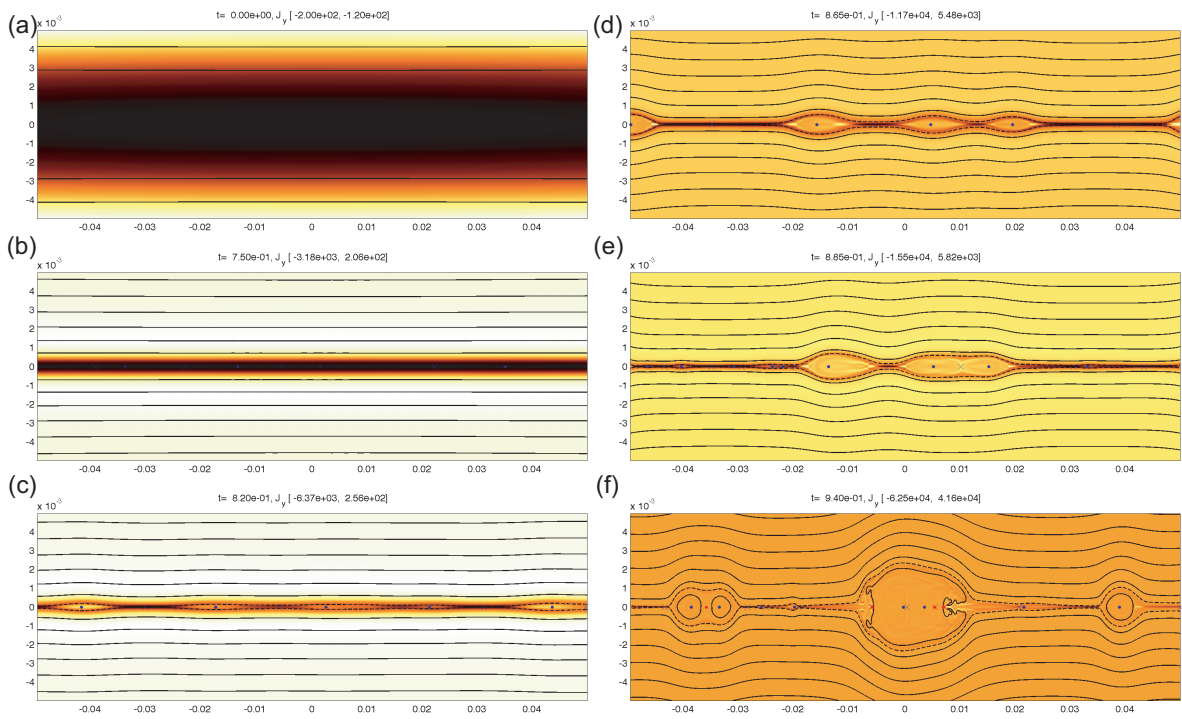


Figure 2.14: Huang and Bhattacharjee (2010)

3 Method

Aiming to solve questions discussed in Sec.2, we conduct MHD simulation of high-Lundquist-number current sheet and try to analyze detailed structure of diffusion region. In this section we will show the method of our research.

3.1 Numerical Scheme

We use the following resistive MHD equations in the conservation form for the numerical simulation.

$$\frac{\partial \rho}{\partial t} + \nabla \cdot (\rho \mathbf{V}) = 0, \quad (3.1)$$

$$\frac{\partial \rho \mathbf{V}}{\partial t} + \nabla \cdot \left[\rho \mathbf{V} \mathbf{V} + \left(p + \frac{B^2}{2} \right) \mathbf{I} - \mathbf{B} \mathbf{B} \right] = 0, \quad (3.2)$$

$$\frac{\partial \mathbf{B}}{\partial t} + \nabla \cdot (\mathbf{V} \mathbf{B} - \mathbf{B} \mathbf{V}) + \eta \nabla \times \mathbf{J} = 0, \quad (3.3)$$

$$\frac{\partial e}{\partial t} + \nabla \cdot \left[\left(e + p + \frac{B^2}{2} \right) \mathbf{V} - (\mathbf{V} \cdot \mathbf{B}) \mathbf{B} + \eta \mathbf{J} \times \mathbf{B} \right] = 0, \quad (3.4)$$

$$(3.5)$$

where $e = p/(\gamma - 1) + \rho v^2/2 + B^2/2$ is the total energy density. The polytropic index is set to $\gamma = 5/3$. All other symbols have their standard meanings. We use the following generalized Ohm's law to derive the MHD equations,

$$\mathbf{E} = -\mathbf{V} \times \mathbf{B} + \eta \mathbf{J}. \quad (3.6)$$

These equations are normalized by the following quantities: upstream magnetic field strength B_0 , upstream density ρ_0 , thickness of the current sheet L_0 . Depending on these three normalization constants, other quantities are normalized: upstream Alfvén velocity $V_{A0} = B_0/\sqrt{\rho_0}$, upstream magnetic pressure $p_{m0} = B_0^2/2$, Alfvén transit time of current sheet thickness $t_0 = L_0/V_{A0}$. Normalization constants are summarized in Tab.3 with typical values.

We use finite volume for discretization and HLLD scheme (Miyoshi and Kusano, 2005) for calculating numerical flux. Magnetic field is a divergence free field, however, this constraint is not explicitly used for solving MHD equations and induction equation (Eq.3.3) is used. Due to the numerical error, nonphysical $\nabla \cdot B$ may be generated. When finite $\nabla \cdot B$ exists, non-realistic force makes the system nonphysical. For keeping divergence free property of magnetic field, we use Flux-CT method (Miyoshi and Kusano, 2011).

Physical quantities	Symbol	Typical value
Length scale	L_0	10^7 cm
Mag. field strength	B_0	10 G
Density	ρ_0	10^9 \#/cm^3
Alfven velocity	$V_{A0} = \frac{B_0}{\sqrt{\rho_0}}$	10^8 cm/s
Time	$t_0 = L_0/V_A$	0.1 s
Pressure	$p_0 = \frac{B_0^2}{2}$	$\sim 4 \text{ dyn/cm}^2$

Table 3: Normalization constants

3.2 Initial Condition

The initial equilibrium condition of numerical simulation is the following Harris type current sheet (Harris, 1962).

$$\mathbf{B}(x, y) = \mathbf{B}_0 \tanh(y/L_0), \quad (3.7)$$

$$p(x, y) = p_0 \left[\cosh^{-2}(y/L_0) + \beta \right], \quad (3.8)$$

The upstream plasma beta β is set $\beta = 0.2$. Magnetic field is initially perturbed with a vector potential $\mathbf{A} = A(x, y)\hat{\mathbf{e}}_z$ for increasing reproductivity and saving computation power. Fig.3.1 shows initial profile of physical quantities such as \mathbf{B} and p . At $y = 0$, magnetic pressure is zero because $\mathbf{B} = 0$ and the current sheet is supported by gas pressure, which is maximum at $y = 0$. Fig.3.2 is a two dimensional illustration of the initial magnetic field line with a red dashed line representing the neutral line where the magnetic field strength is zero. Note that in the global model in Sec.4, the coordinate is 90 degree rotated. We need to swap the axis in the following ways to change from this coordinate to that in global model: $y \rightarrow z, z \rightarrow -y$.

3.3 Boundary Condition

The boundary condition of simulation box must be set consistent with the initial condition, symmetry, and physical process to solve. Possible simulation boundaries in this study is shown as 1 – 3 in Fig.3.3: 1. reflecting boundary, 2. conducting wall, 3. reflecting boundary. These boundary conditions are summarized in Tab.4. We cannot solve outside of the boundary, but we need quantities just outside of the boundary. At the margin region, all physical quantities should be set consistent with the symmetry of the boundary. Vector quantities such as \mathbf{B} and \mathbf{V} is sometimes required to multiply -1 to meet the condition. Boundary condition of electric field also need to be consistent with the symmetry of \mathbf{B} and \mathbf{V} . Furthermore, electric field has two component of $\mathbf{V} \times \mathbf{B}$ and $\nabla \times \mathbf{B}$. These two terms need to have the same symmetry. These criteria are sometimes difficult to meet at once especially in three dimensional system, which have larger degree of freedom. The boundaries 1 and 3 in Fig.3.3 are not appropriate

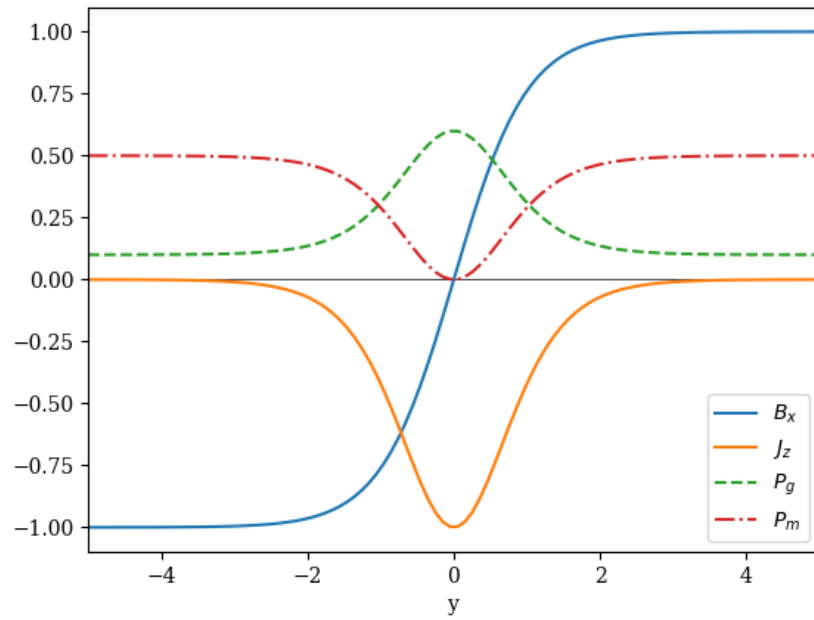


Figure 3.1: Harris equilibrium current sheet.

as a boundary in three dimensional simulation of current sheet with guide field (out-of-plane component of magnetic field).

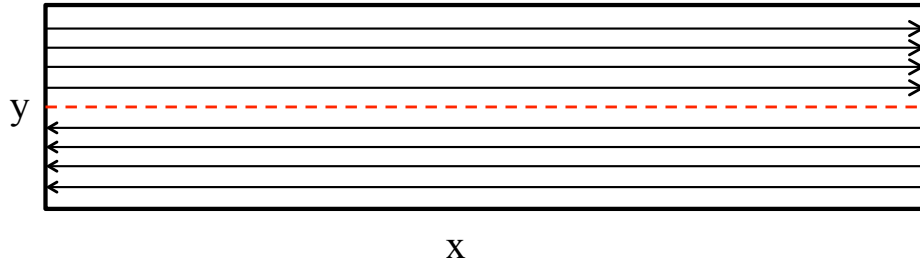


Figure 3.2: 2D illustration of the initial condition

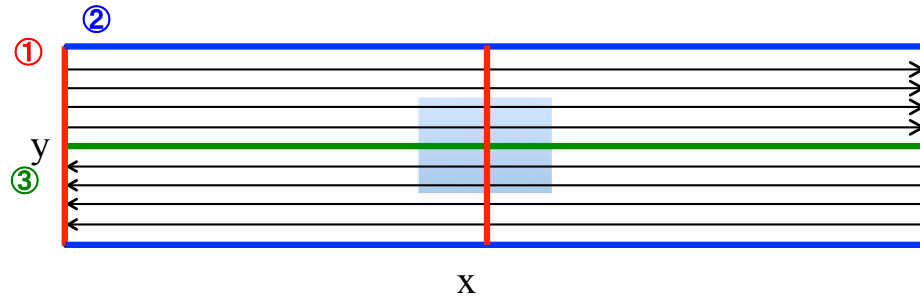


Figure 3.3: 2D illustration of the boundary condition

Physical quantities	1. reflecting boundary	2. conducting wall	3. reflecting boundary
B_x	+	+	-
B_y	-	-	+
V_x	-	+	+
V_y	+	-	-
E_z	+	-	+

Table 4: symmetry and anti-symmetry of the boundary condition

4 Global Model

4.1 Model

We perform two-dimensional resistive MHD simulation of reconnection in an anti-parallel magnetic field configuration of the Harris current sheet (Ji and Daughton, 2011). We solved the standard set of compressible resistive MHD equation, where viscosity and thermal conductivity are ignored. The initial magnetic field is given by

$$\mathbf{B} = (B_0 \tanh(z/L_0), 0, 0), \quad (4.1)$$

where L_0 is the current sheet half-thickness. The size of the simulation box, which is $0 < x < 600L_0$, $0 < z < 25L_0$, is set to be large enough for allowing nonlinear evolution and motion of plasmoids with a little effect of boundaries. Assuming symmetry, only the upper half of the system is followed in computation. Reconnection is triggered by a small initial magnetic field perturbation, which is localized at the center, $275L_0 < x < 325L_0$. In order to resolve fine structure of the current sheet and plasmoids, we used a refined grid size that is almost uniform within the domain $220L_0 < x < 380L_0$, $z < 0.8$ but gradually stretches toward the boundaries. The boundary conditions are as follows: a conducting wall at the top boundary, and mirror symmetry at all others. A typical spatial resolution for the case of the Lundquist number $S_0 = L_0 V_{A0} / \eta = 10^4$ is $\Delta x = 9 \times 10^{-3} L_0$, $\Delta z = 8 \times 10^{-4}$ at the center of current sheet. The magnetic diffusivity η is assumed to be spatially uniform and not varying with time, and the plasma beta is $\beta = 0.2$ in a uniform plasma far from the current sheet. The presented below results correspond to three particular values of the Lundquist number: $S_0 = 10^4$, 10^5 and 10^6 , all of which are above the plasmoid instability threshold S_c . Aiming to clarify the mechanism of fast reconnection, in this paper we concentrate mainly on the case of $S_0 = 10^4$. Note that under the above given normalization the value of Lundquist number is defined by the current sheet thickness. However, in all preceding studies of the plasmoid instability (Loureiro et al., 2007; Bhattacharjee et al., 2009; Lapenta, 2008; Uzdensky et al., 2010; Huang and Bhattacharjee, 2010) the current sheet length rather than its thickness is used as a scale length. Therefore, in order to make a proper comparison, one should re-calculate the Lundquist number accordingly. Thus, our case of $S_0 = 10^4$, where the current sheet length is about $100L_0$, corresponds to $S = 10^6$ for the simulations reported in Bhattacharjee et al. (2009); Lapenta (2008); Uzdensky et al. (2010); Huang and Bhattacharjee (2010).

The normalized reconnection rate (Fig.4.1) is defined as the time derivative of the reconnected magnetic flux divided by the product of the Alfvén velocity and the horizontal magnetic field (B_x) strength at the inflow boundary of diffusion region. The reconnected flux is calculated as the difference between the maximum and the minimum values of the magnetic flux function along the current sheet (line $z = 0$ on Fig.4.2). The inflow boundary is assumed

to be located above the X-point where the current density is one order of magnitude smaller than at the X-point itself.

4.2 Result

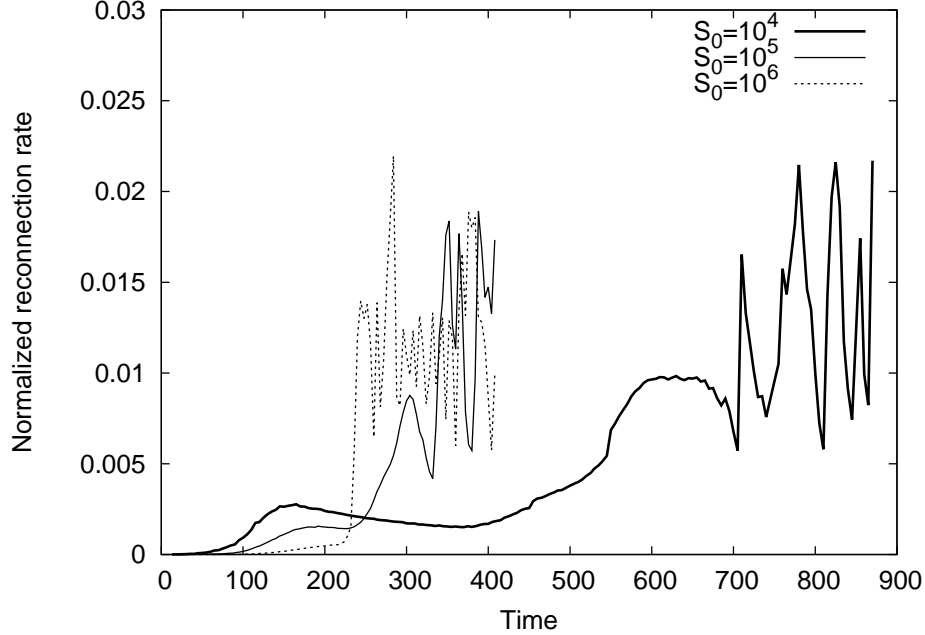


Figure 4.1: Temporal evolution of the normalized reconnection rate for different values of the Lundquist number S_0 .

Fig.4.1 shows temporal evolution of the scaled reconnection rate for the cases of $S_0 = 10^4$, 10^5 and 10^6 . Initially, at $t \leq 200$, the reconnection rate is slower for higher Lundquist numbers. At this stage an elongated Sweet-Parker type current sheet is formed as shown in Fig.4.2, which represents temporal evolution of the magnetic field and the electric current structure for the case of $S_0 = 10^4$. Then, as time progresses, the aspect ratio of the current sheet becomes too large, and the sheet breaks up due to plasmoid instability ($t \approx 400$, Panel (c)). After that, a further growth of plasmoids increases the reconnection rate up to 0.01 at $t = 500$ –600 (Panels (d), (e)).

Consider now in more detail evolution of four particular plasmoids (labeled as Plasmoids 1–4 on Fig.4.2), which are located just to the right of the current sheet center. As seen from Fig.4.2, between $t \sim 600$ and 700 the central three plasmoids (including Plasmoid 1) collide and merge, creating the next-generation ones such as Plasmoid 2. At about the same time (after $t \sim 700$, see Fig.4.1) an intermittent fast reconnection with the rate up to 0.02 becomes established, which is caused by strong electric currents concentrated adjacent to

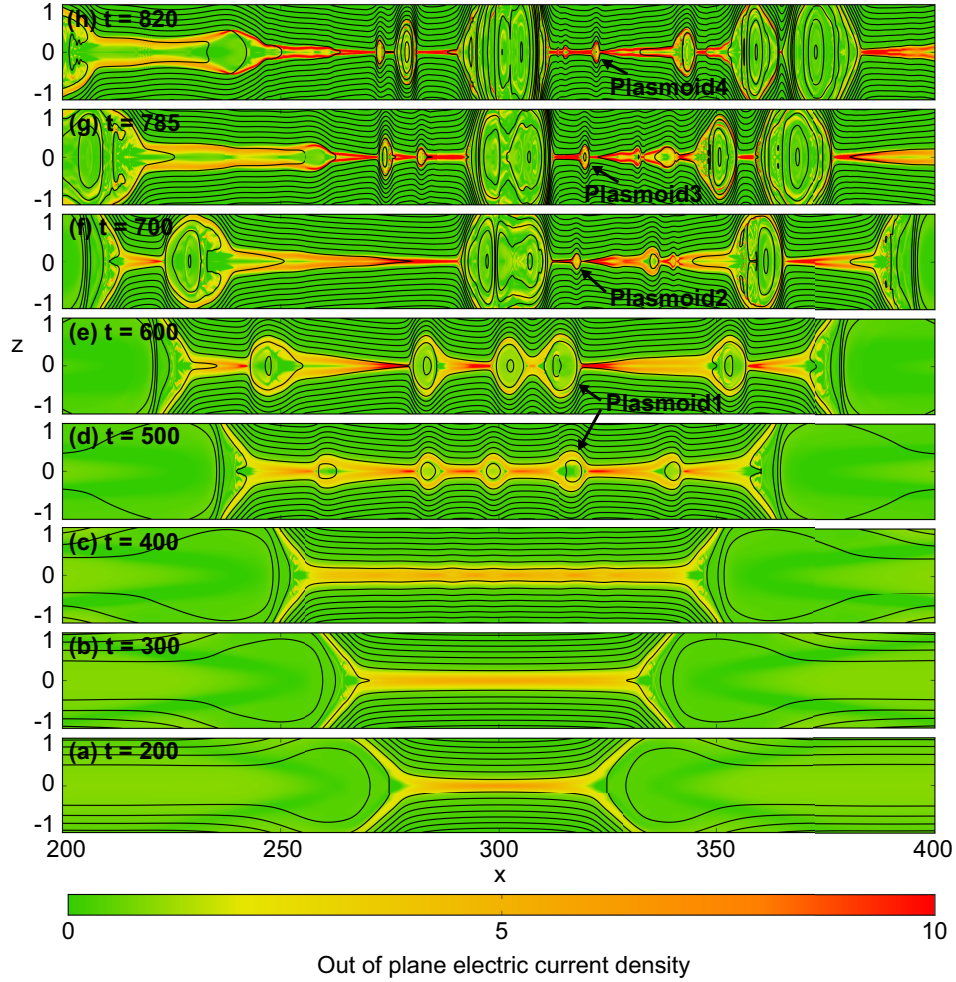


Figure 4.2: Magnetic field (solid lines) and electric current density at various stage of reconnection for $S_0 = 10^4$.

plasmoids. According to Panels (e–h), the electric current density peaks just outside of the right-hand side edges of Plasmoids 1–4, and this strong current drives the reconnection rate maxima at the moments of $t = 630$, 710 , 780 and 825 respectively. Importantly, at this stage

the global current sheet becomes bifurcated, forming V-shaped structures with the vertexes facing plasmoids. The appearances of V-shaped current patterns well coincide with the peaks of the reconnection rate.

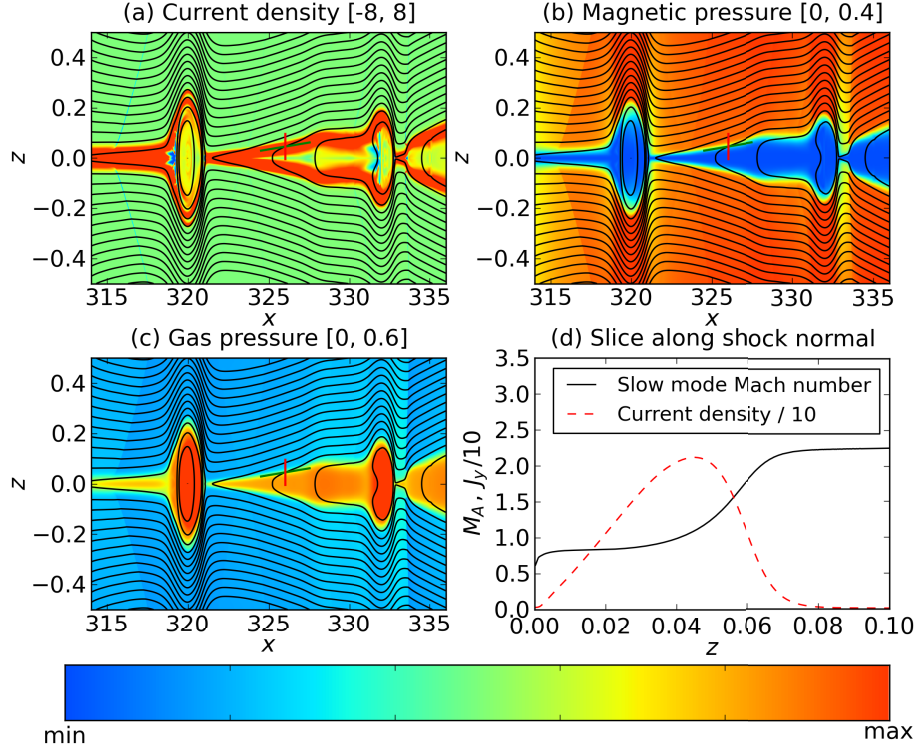


Figure 4.3: Pseudo-color plots of electric current (Panel (a)), magnetic pressure (Panel (b)), and gas thermal pressure (Panel (c)) around the shock in front of Plasmoid 3 at $t=785$ for $S_0 = 10^4$. On Panel (d) we plotted variations across the shock of the local slow mode Mach number (black solid line) and the current density (red dotted line) across the shock. The current density is scaled down by a factor of 10 for a better visualization.

In order to verify the nature of these V-shaped structures, on Fig.4.3 we depict detailed distribution of the electric current as well as the magnetic and thermal pressure for such a structure in front of the Plasmoid 3. As seen from Panels (b) and (c), the magnetic pressure dominates in the upstream region, while in the downstream one the thermal pressure is higher. Thus, conversion of magnetic energy into heat occurs inside the narrow separation layer with

a strong current, which turns out to be a slow-mode MHD shock. Indeed, consider Panel (d), which shows variation of the slow-mode Mach number (black solid line) and the out-of-plane current density (red dotted line) across the shock. It indicates the Mach number above unity upstream, and the one below unity downstream. Therefore, the observed discontinuity is a slow-mode shock predicted in the Petschek reconnection model. Other bifurcated current layers that appear adjoining large plasmoids on Fig.4.2 also show characteristics of the slow-mode shock, although some of them look quite diffusive because of a relatively large plasma resistivity ($S_0 = 10^4$). Note, however, that unlike Petschek model of steady reconnection, here they are of a transient nature, and form only on the one side of magnetic X-points. Therefore, each peak of the reconnection rate corresponds to fast ejection of plasma caused by these slow mode shocks.

The relationship between the structure of electric currents and the dynamics of plasmoids is shown on Fig.4.4, where we plot time-distance diagram of the current density near the center of the current sheet. Here white and black thin solid lines show locations of magnetic O-points and X-points respectively. Plasmoids can be seen there as green bands where the electric current density is quite low, while regions of strong current around X-points (black lines) are shown as red bands. Thus, at $t = 550$ there are three large plasmoids, whose O-points are located at $x = 300, 317$ and 346 . One of them moves rightward and is ejected out of the center, while the two others collide at $t \approx 610$. This collision creates a new-generation plasmoids such as Plasmoid 2 formed at $t \approx 670$. The newly formed plasmoids start to move rightward, and the intense current density in front of them provides for fast reconnection. Such a structure resembles the one observed in [Baty \(2012\)](#), although the simulation there was performed for a non-uniform plasma resistivity.

Note that as the reconnection proceeds, Plasmoids 2–4 decelerate and eventually turn around. This is due to the reconnection outflow from the X-points located in front of them. When Plasmoids 2–4 are turned around and move away from the respective X-points, the current sheets on their right-hand side become elongated (the distance between the white and black lines on Fig.4.4 increases), and the current density there goes down together with the rate of reconnection. Eventually, these plasmoids collide with a larger one closer to the center, giving birth to plasmoids of the next generation (see Plasmoids 2, 3, 4 at $t \approx 680, 780, \text{ and } 820$). A repetitive nature of this process makes magnetic reconnection fast but intermittent.

A similar dynamics for a larger Lundquist number, namely $S = 10^6$, can be seen on Fig.4.5, which depicts time-distance diagrams of the horizontal plasma velocity (Panel (a)) and the current density (Panels (b) and (c)). According to Fig.4.1, the respective reconnection rate goes up at $t \approx 240$, and this roughly coincides with the qualitative change of the plasmoids evolution (see Panel (b)). Initially plasmoid instability creates a large number of individually evolving small plasmoids and X-points. On the contrary, at this moment each X-point starts

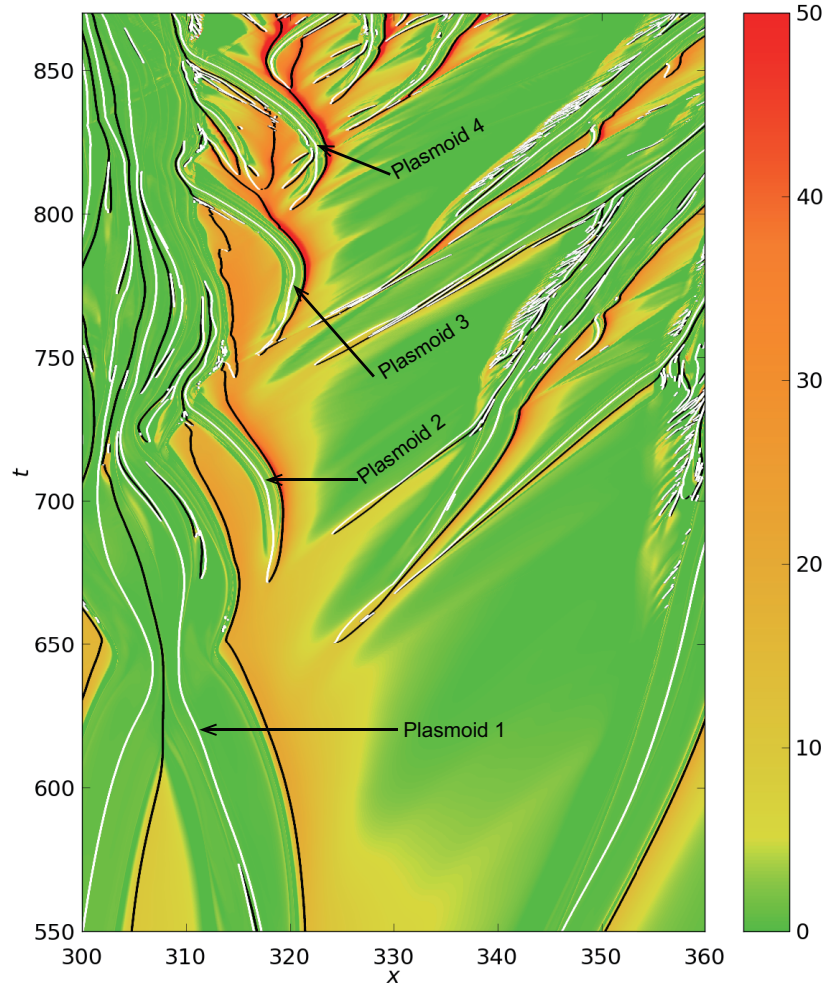


Figure 4.4: Time-distance diagram of the electric current and plasmoid dynamics at the equatorial plane ($z=0$) of the current sheet for $S_0 = 10^4$.

to produce the next generation ones in succession, forming a sort of a “ family tree ”. As time goes by, plasmoids merge, and only a few separated families survive. As seen on Panel (a), such a reduction enables formation of a coherent global outflow at $t \sim 300$. Note also that the time-distance diagram of the current density and the X-points evolution for a single family confined inside the rectangle on Panel (c) resembles the one plotted on Fig.4.4 for the case of $S_0 = 10^4$. This similarity in the micro-scale dynamics demonstrates why the rate of reconnection is not sensitive to the actual value of the Lundquist number.

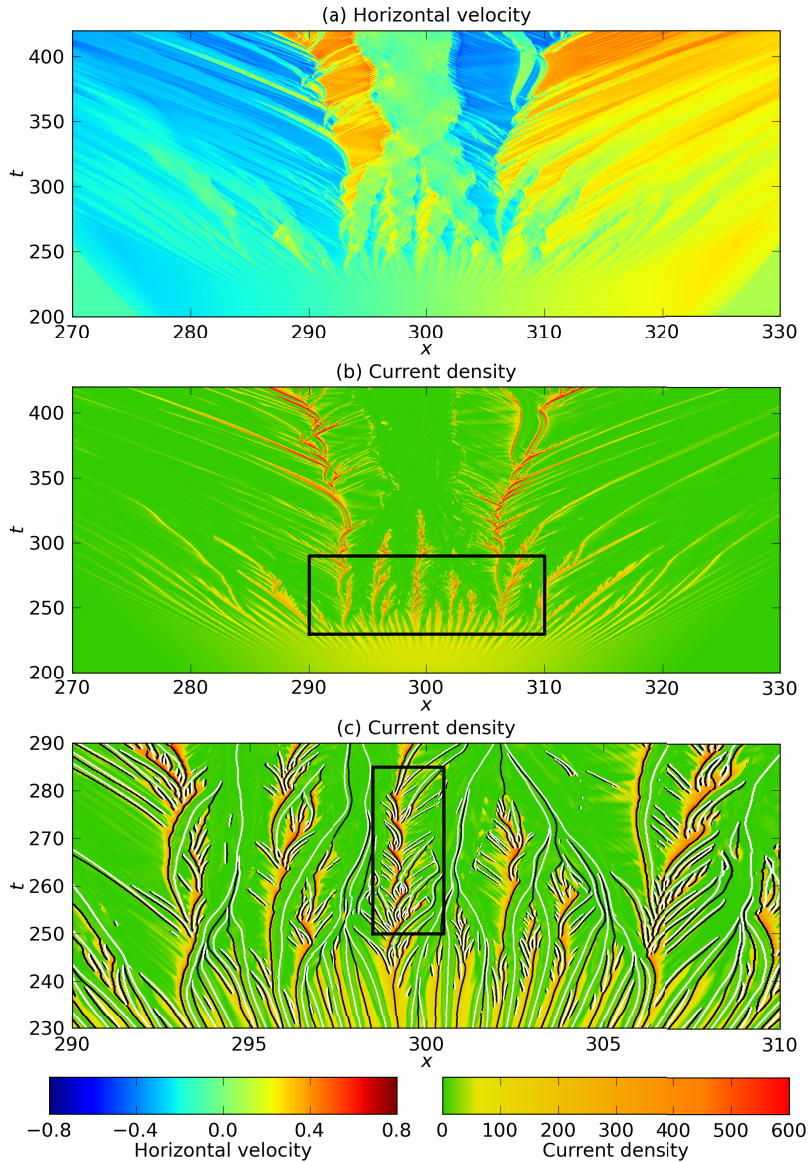


Figure 4.5: Time-distance diagram of the horizontal velocity and electric current at the equatorial plane ($z=0$) of the current sheet for $S_0 = 10^6$. Panel (c) is an enlarged plot of the area inside the rectangle on Panel (b). White and black thin solid lines on Panel (c) indicate locations of magnetic O-points and X-points respectively.

4.3 Discussion

Summarizing our findings, we suggest a novel regime of fast MHD magnetic reconnection, which can be called *dynamical Petschek reconnection*. Its essential elements are as follows:

1. Secondary tearing (plasmoid) instability of elongated reconnecting current sheet, which breaks it up into a chain of magnetic islands (plasmoids).

2. Nonlinear evolution and motion of plasmoids, which make possible spontaneous formation of small-scale slow-mode shocks (Petschek-type shocks).
3. Sporadic appearance of slow-mode shocks facilitate plasma ejection out of the current sheet. This allows higher velocity of the plasma inflow (up to 0.02 of the Alfvén speed) into the reconnection site, bringing about fast MHD reconnection.

Such a scenario is efficient enough to account for various natural phenomena presumably associated with magnetic reconnection. On the other hand, it can be explained by exploring a simple MHD model, without invoking more specific kinetic effects.

So far it was widely accepted that Petschek-type reconnection is possible only if the resistivity or viscosity of a fluid is localized (Forbes et al., 2013; Baty et al., 2014, 2009; Ugai and Tsuda, 1977; Kulsrud, 2001), which prevents elongation of the current sheet. Our simulations, however, clearly demonstrate that the required current localization can be provided by plasmoids, which are naturally formed due to the secondary tearing instability, even if resistivity and viscosity are uniform. Quite remarkably, it turns out that a higher Lundquist number is actually favorable for fast reconnection. This is seen from Fig.4.1, where transition to the regime of fast reconnection occurs earlier and more abruptly for the higher values of S_L .

The dynamical Petschek reconnection is intrinsically intermittent. Such a regime becomes established due to simultaneous action of two competing processes: the electric current strengthening at the front of plasmoids, and the current weakening by stretching of the interplasmoid current sheets. This brings about a sort of the dynamical self-organization in the system: the reconnection rate is capped at 0.01–0.02 while varying temporally with some characteristic time-scale (see Fig.4.1). Note that the respective variation time depends on the Lundquist number, being shorter for larger. Therefore, such a dependence can be used as a probing tool for the underlying dynamics of plasmoids.

5 Local Model

5.1 Model

To better understand the fundamental formation process of Petschek-type structure, we constructed a simple model employing time-dependent MHD simulation. The initial condition is the following Harris-type current sheet of width L_0 plus an initial perturbation [Harris \(1962\)](#):

$$\mathbf{B}(x, y) = \mathbf{B}_0 \tanh(y/L_0) \quad (5.1)$$

$$p(x, y) = p_0 \left[\cosh^{-2}(y/L_0) + \beta \right], \quad (5.2)$$

where $\mathbf{B}_0 = (B_0, 0)$, and β denotes the upstream plasma beta, i.e., the ratio between the upstream gas and magnetic pressures. In our modeling, we used $\beta = 0.2$. Since we construct this model to study the fundamental process of how a single diffusion region forms in the large-scale simulation [Shibayama et al. \(2015\)](#), we apply an initial condition and perturbation which are symmetry in both x and y directions to avoid the motion of the plasmoid. The numerical simulations are conducted only for the first quadrant. We apply two initial perturbations to study the dependence on the initial condition. The initial perturbations of magnetic field are given by the following vector potentials:

$$\mathbf{A}_1(x, y) = A_0 \left\{ \exp \left[- \left(\frac{x - x_0}{\lambda_x} \right)^2 - \left(\frac{y}{\lambda_y} \right)^2 \right] + \exp \left[- \left(\frac{x + x_0}{\lambda_x} \right)^2 - \left(\frac{y}{\lambda_y} \right)^2 \right] \right\} \hat{\mathbf{e}}_z, \quad (5.3)$$

or

$$\mathbf{A}_2(x, y) = -A_0 \exp \left[- \left(\frac{x}{\lambda_x} \right)^2 - \left(\frac{y}{\lambda_y} \right)^2 \right] \hat{\mathbf{e}}_z, \quad (5.4)$$

where $x_0 = 10L_0$, $\lambda_x = \lambda_y = 5L_0$, and $A_0 = 0.05$. Both of the perturbations correspond to single isolated plasmoid with double X-point at $\pm x_0$ or single O-point at the origin. The initial condition slightly differs from equilibrium due to the perturbation. The final expansion phase discussed in the latter sections is, however, almost independent of the details of the initial condition. The computational domain is $0 \leq x \leq L_x$, $0 \leq y \leq L_y$, where $L_x = 600L_0$, and $L_y = 50L_0$. Here L_x and L_y are set to be sufficiently large to minimize the effect of the boundary on the reconnection structure. As boundary conditions, reflection boundaries are set at $x = 0$, $x = L_x$ and $y = 0$, while the boundary at $y = L_y$ is a conducting wall. As the simulation proceeds, a plasmoid forms at the origin with its center (magnetic O point) fixed at the origin as a result of the boundary conditions, i.e., the symmetry of the system. This setup simplifies the analysis and evolutionary details of the diffusion region adjacent to the plasmoid. [Murphy \(2010\)](#) refers to the initial condition with \mathbf{A}_1 as a double perturbation.

The electric resistivity in the model is set at $\eta = 1/300$ to reproduce the local conditions in our previous large-scale simulation [Shibayama et al. \(2015\)](#) (See Discussion section for details). In the simulation, physical quantities are normalized to the following values: $B_0/\sqrt{4\pi}$, L_0 , upstream plasma density $= \rho_0$, and upstream Alfvén velocity, $V_{A0} = B_0/\sqrt{4\pi\rho_0}$. Accordingly, other quantities are normalized as follows: $t_0 = L_0/V_{A0}$, $p_0 = B_0^2/(8\pi)$, $J_0 = B_0/(\sqrt{4\pi}L_0)$, $F_0 = B_0^2/(4\pi L_0)$. We use non-uniform grid along the x and y directions that is almost uniform at $0 \leq x < 200$, $0 \leq y < 5$ and gradually expand in $+x$ and $+y$ direction in order to minimize numerical diffusion and reduce the computational cost. The simulation setups are summarized in [Tab.5](#). The largest grid number is 8192×2048 and the highest spatial resolution is $\Delta x = 3.5 \times 10^{-2}$ and $\Delta y = 5.1 \times 10^{-3}$ at around the origin (run 1). Most of the results in this paper are obtained from run 1. The results and discussions do not significantly change in the run with half grid number in both direction (run 2), whose difference of reconnection rate from run 1 is only less than 2%.

	Initial perturbation	Grid number
Run 1	\mathbf{A}_1	8192×2048
Run 2	\mathbf{A}_1	4096×1024
Run 3	\mathbf{A}_2	4096×1024

Table 5: Initial perturbations and grid settings.

5.2 Results

[Fig.5.1](#) shows the distribution of out-of-plane current density J_z , and outflow velocity V_x at $t = 500$. A Petschek-type bifurcated current structure is observed at $15 < x < 125$ ([Fig.5.1\(a\)](#)). This current density structure is quite similar to Petschek-type reconnection with anomalous resistivity [Zenitani and Miyoshi \(2011\)](#), although the resistivity is uniform and the plasmoid is located at the origin in our simulation. The diffusion region is localized adjacent to the plasmoid, from which it can be inferred that the localization is related to the plasmoid and the surrounding plasma condition. The entire structure is similar to the one in [Figure 3 of Shibayama et al. \(2015\)](#). Additionally, it is seen from [Fig.5.1\(b\)](#) that the width of the reconnection outflow increases with the outflow toward the positive x direction: this structure is another important characteristic of Petschek reconnection. In the latter phase ($t > 500$) after the formation of Petschek-type diffusion region, the system shows gradual, self-similar-like expansion. Note that in our simulation results only the right-hand side of the Petschek model is formed, while the steady-state Petschek model is symmetric across the diffusion region.

[Fig.5.2](#) shows the detailed flow structure around the diffusion region. It is seen from [Fig.5.2\(a\)](#) that the flow structure around the X-point is asymmetric, with the Petschek-type

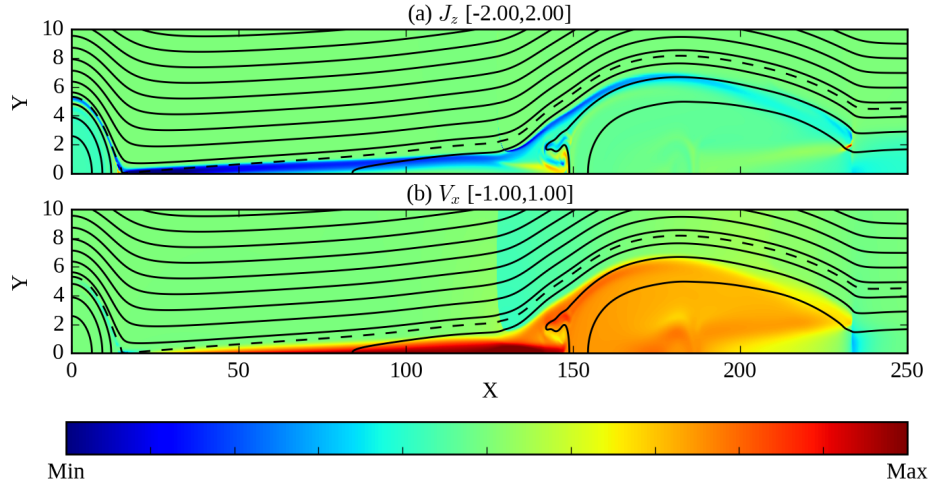


Figure 5.1: Spatial distribution of out-of-plane current density J_z and outflow velocity V_x at $t = 500$ for run 1. The color range is shown with the panel titles. Solid and dashed lines indicate magnetic field lines and separatrix, respectively.

structure appearing only just to the right of the X-point, while the leftward outflow is very short and connected to the plasmoid. Fig.5.2(b) shows a line integral convolution plot of the flow structure, in which each pattern is aligned with the local velocity vector. It is seen that the inflow is primarily inclined to the left. Fig.5.2(c) shows a profile of the outflow velocity and reconnected magnetic field strength along $y = 0$. At $t = 500$, the X- and S- points are located at $x = 16.3$ and 20.5 , respectively. The clear separation in x direction results in a strong plasma flow at nearly the Alfvén velocity in negative x direction at the X-point. The localization of the diffusion region is seen from Fig.5.2(d), which shows terms in the right hand side of Eq.3.6 along $y = 0$. The resistive term is dominant in $15.5 < x < 28.9$ and the diffusion region is localized compared to the distance between the plasmoids, which is about 10 times larger than the diffusion region length.

The temporal evolution of physical quantities are shown in Fig.5.3. Positions in the x direction of the X- and S- points (x^{XP} and x^{SP} respectively) show that the S-point overtakes the X-point at $t \sim 200$ (Fig.5.3(a)), which is also pointed out in Murphy (2010). The final expansion phase ($t > 500$) is, however, nearly independent of the initial behavior. Fig.5.4 shows the same plot for run 3, which shows qualitatively similar time evolution to that of run 1 except for the initial behavior of the X- and S- point location. Note that the range of the horizontal and vertical axis is different between Fig.5.3 and 5.4. Fig.5.3(b) denotes the plasma velocity at the X-point V_x^{XP} and the reconnection rate as functions of time. The reconnection rate is defined as ηJ_z at the X-point, which corresponds to the reconnection rate normalized by the initial upstream quantities. V_x^{XP} increases to ~ 0.4 at $t = 300$ and

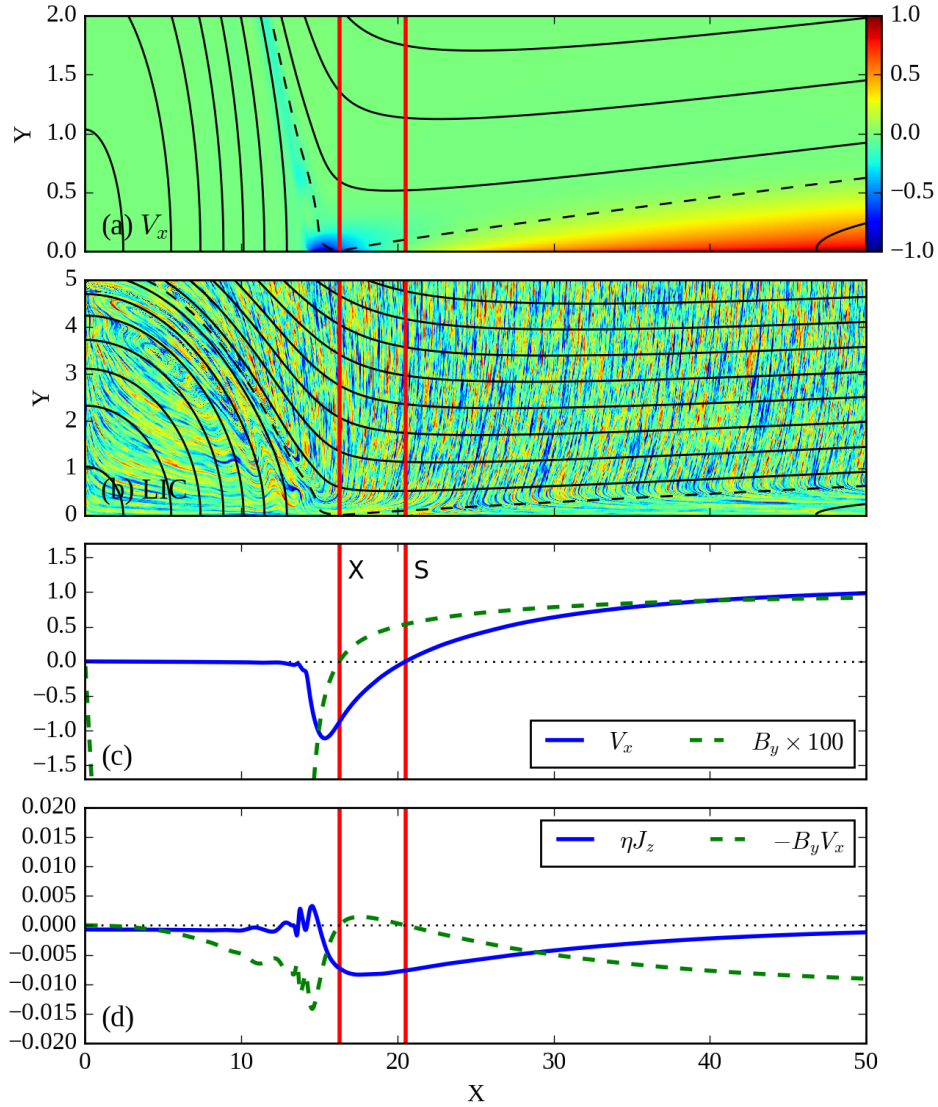


Figure 5.2: (a) Outflow structure, and (b) line integral convolution plot of the flow at $t = 500$ for run 1. (c) Outflow and reconnected magnetic field profile, and (d) terms in Ohm's law along $y = 0$ at $t = 500$ for run 1. All panels are aligned in the vertical direction. The vertical red solid lines in each panel show the location of the X- and S- points on the x-axis.

reaches almost 1 in the final expansion phase ($t > 500$). The reconnection rate increases up to about 0.008 and decreases as the structure expands. This reconnection rate is smaller than our previous results [Shibayama et al. \(2015\)](#). The difference may be explained by the asymmetry in the x -direction (see Discussion section for detail). Fig.5.3(c) shows geometry of the current sheet. The Current sheet is defined as the region where $\eta \mathbf{J}$ term is dominant in Eq.3.6 ($\eta |\mathbf{J}| > |\mathbf{V} \times \mathbf{B}|$). The length L_{CS} and the thickness δ_{CS} of the current sheet are measured from the X-point to x and y direction respectively. Since the current sheet is asymmetry in the x direction, L_{CS} and δ_{CS} are the full length and thickness of the current sheet. We do not define L_{CS} and δ_{CS} in the initial phase ($t < 80$) because the current sheet is

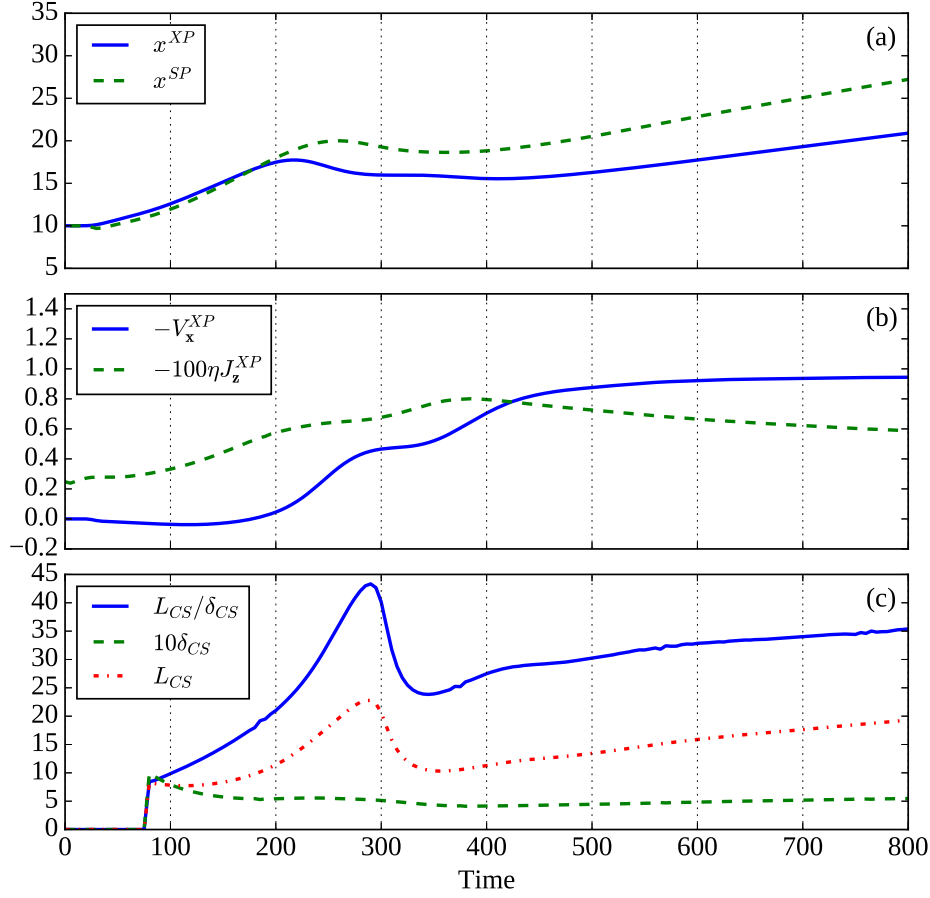


Figure 5.3: (a) location of the X- and S- points, (b) x -component of velocity at the X-point and the reconnection rate, (c) length L_{CS} , thickness δ_{CS} and aspect ratio of the diffusion region as functions of time for run 1.

not formed yet. The aspect ratio of the current sheet L_{CS}/δ_{CS} increases and peaks at $t \sim 300$, then decreases when $V_x^{XP} \simeq -0.4$.

If symmetry is assumed around the neutral line ($y = 0$), the x -component of the equation of motion and the y -component of the induction equation on the neutral line can be written as follows:

$$\rho d_t V_x = F_x^{PR} + F_x^L, \quad (5.5)$$

$$\partial_t B_y = -\partial_x (V_x B_y) + \eta \partial_x J_z, \quad (5.6)$$

where ∂_x and d_t represent the differential operators $\partial/\partial x$ and d/dt respectively, and F_x^{PR} and F_x^L are the pressure gradient force $F_x^{PR} = -\partial_x P$ and Lorentz force $F_x^L = -J_z B_y$, respectively. Fig.5.5 plots each term in Eqs.(5.5) and (5.6) against x . In Fig.5.5(a) it is seen that the

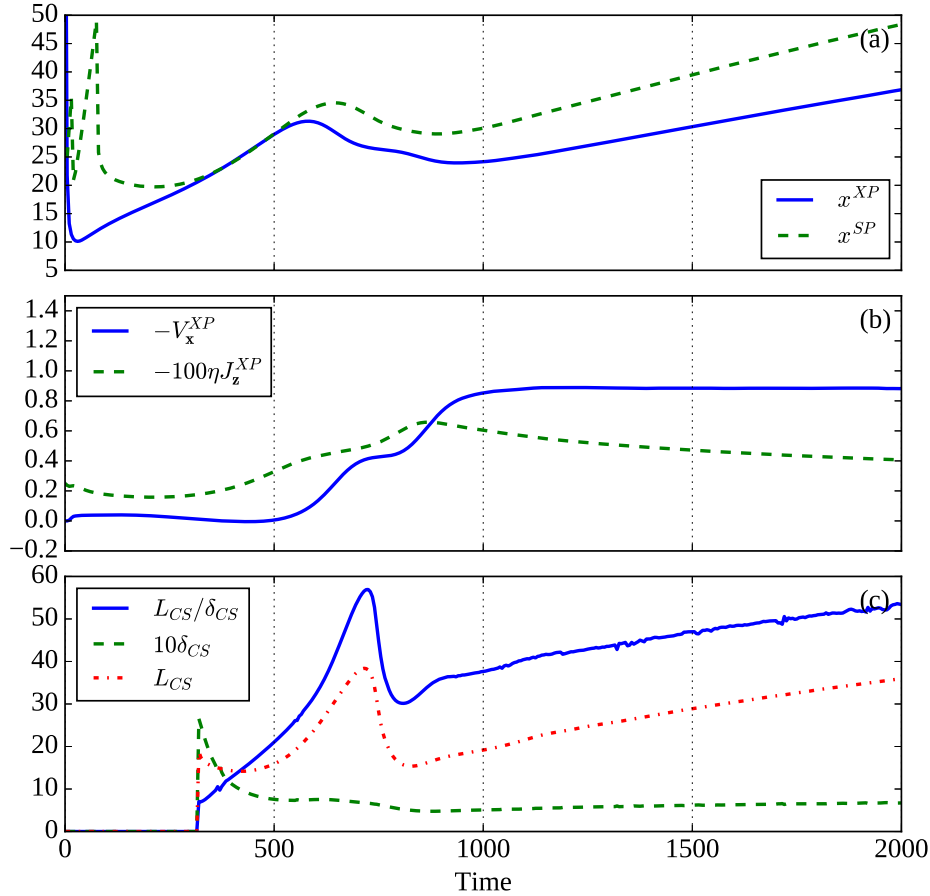


Figure 5.4: The same as Fig.5.3 but for run 3.

rightward outflow plasma is accelerated by the Lorentz force F^L , a characteristic of the Petschek model. By contrast, outward flow to the left is accelerated by the gas pressure gradient force F^{PR} , a characteristic of the Sweet-Parker model.

It is seen from Fig.5.5(b) that the terms on the right-hand side of Eq.(5.6) nearly cancel to the right of the X-point. As a result, the variation of B_y over time is minimal and the system is in a quasi-steady state. The evolution of the system actually shows a self-similar-type gradual expansion. These results suggest that the state is a close to self-similar solution of the MHD equations: Nitta (2007) noted that an existence of such a solution with a plasmoid at the origin.

5.3 Discussion on Local Model

In the preceding section, we presented simulation results indicating Petschek-type reconnection in a system with uniform resistivity, in which the the separation of the X-point from the

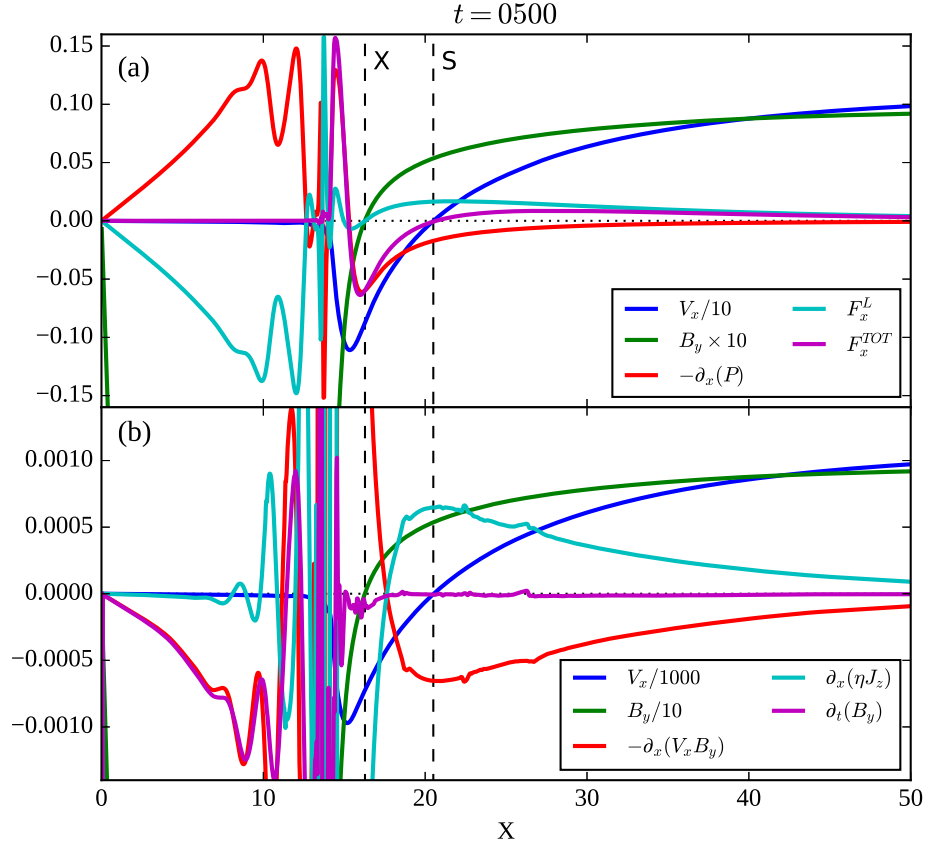


Figure 5.5: Each term of: (a) the x -components of the equation of motion, and (b) the y -components of the induction equation along the neutral plane $y = 0$ at $t = 500$ for run 1. The vertical dashed lines show the locations of the X- and S- points. Here, we note that there is a large fluctuation at $10 < x < 15$, as a result of the termination shock of the leftward outflow.

flow stagnation point is observed. In this section we discuss the evolution of the location of the X- and S- points and how this works as a localization mechanism in *dynamical Petschek reconnection* regime [Shibayama et al. \(2015\)](#).

According to [Murphy \(2010\)](#), the velocity of apparent motion of the X-point V_{XP} is determined by the following equation,

$$V_{XP} \simeq \left(V_x - \frac{\eta}{\partial_x B_y} \partial_y^2 B_y \right)_{X\text{-point}}. \quad (5.7)$$

The first term in the right-hand side of this equation corresponds to the ideal MHD contribution, while the other term is the resistive factor. In our simulation, plasma flow occurs at X-point as a result of the separation of the X- and S- points. This flow, which corresponds

to the first ideal term in Eq.(5.7), prevents the motion of the X-point. As the X-point is located near the plasmoid, this results in localization of the diffusion region. By contrast, in the classical symmetric reconnection case the X- and S- points coincide and therefore the plasma velocity is zero at the X-point. The separation of the X- and S- points is the key characteristic of Petschek-type reconnection under uniform resistivity.

In addition to the local flow structure discussed above, the global eddy structure in the inflow region plays an important role in the plasma dynamics. As the plasmoid instability evolves, large eddies form in the inflow region Lapenta (2008). It is seen from Fig.5.2(b) that the diffusion region is embedded in the eddy around the plasmoid: accordingly, the inflow velocity has a negative x component prior to entering the diffusion region. The eddy evolves as the plasmoid grows non-linearly, modifying both the velocity and magnetic field structure in the inflow region.

In our model, we use a spatially and temporally constant electric resistivity $\eta = 1/300$, current sheet with thickness $L_0 = 1$. This setting corresponds to the sheet occurring in our previous simulation Shibayama et al. (2015) following re-normalization. In the $S_0 = 10^4$ run ($\eta = 10^{-4}$), the typical current sheet thickness prior to the formation of the plasmoid and Petschek-type structure was 1/20–1/30.

It is well known that a resistive MHD system is characterized by a single non-dimensional number—magnetic Reynolds number $R_m = lv/\eta$. Using the initial current sheet thickness and upstream Alfvén speed as typical values, in our model $R_m = 300$. This specific value of the magnetic Reynolds number is related to Eq.5.7, in which the first ideal term has a value on the order of one owing to the outflow. By contrast, it is seen from Fig.5.2(a) that the speed of the X-point propagation is on the order of 0.01. The following resistive term in the formula must almost compensate for the ideal term when the system is in the slow expansion phase. The term contains η and spatial gradient of magnetic field. When η is small, and Lundquist number is large, the length scale of the structure should be proportionally small, resulting in R_m on the same order of magnitude, which is 300 in our results.

Although the Lundquist number, S , is also non-dimensional parameter, the global system size is used as the typical length. Even in high Lundquist number systems, the local magnetic Reynolds number can become as small as 300 when the current sheet is sufficiently thin, allowing the Petschek-type structure reported in this paper to appear. This mechanism determines the reconnection rate under *dynamical Petschek reconnection*, in which the rate is driven by the Petschek-type structure rather than Sweet-Parker model.

We next compare our results with those of a previous model of Petschek-type reconnection under uniform resistivity by Kulsrud (2001), in which the Petschek-type diffusion region cannot retain its structure in the steady state because the uniformly resistive system does not have a mechanism to localize the diffusion region. In our model, by contrast, the diffusion region is localized and Petschek-type reconnection is achieved even under uniform resistivity.

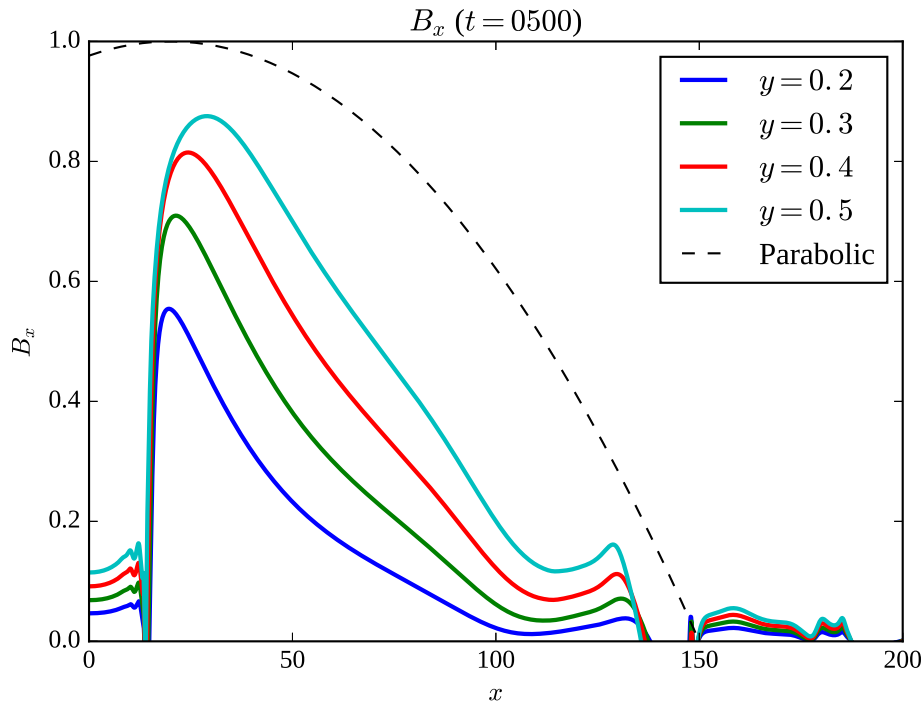


Figure 5.6: Profile of the reconnecting magnetic field B_x in the inflow region at different y at $t = 500$ for run 1, as well as a parabolic curve, which is the assumption in Kulsrud (2001).

There are a few differences between our results and the theory in Kulsrud (2001). The most important difference is in the profile of magnetic field strength in the inflow region. Kulsrud (2001) assumes an upstream profile $B_x = B_0(1 - x^2/L^2)$, where L denotes the global system size. This means that B_x gradually decays with system size. The profile of B_x in the inflow region is shown in Fig. 5.6. The dashed line is a parabolic curve of $B_x = 1 - (x - 20)^2/130^2$, which leads to Sweet-Parker reconnection according to Kulsrud (2001). In our numerical simulation the upstream profile of B_x decays more steeply especially around the center of the diffusion region $20 < x < 50$. The steep profile of B_x is formed in a self-consistent manner as a result of the evolution of the plasmoid and surrounding plasma flow, indicating that a Petschek-type diffusion region can spontaneously form in a non-steady system even under uniform resistivity. Baty et al. (2014) also discusses the stability of Petschek reconnection under spatially localized resistivity, and reports that asymmetric Petschek reconnection is stable in resistivity profiles that are flatter than Gaussian. Our results show that asymmetric Petschek reconnection is stable under uniform the resistivity, which is a flat limit of resistivity profile. Accordingly, our results are qualitatively consistent with the result in Baty et al. (2014).

Priest and Forbes (1986) proposed a generalized model of fast steady state magnetic

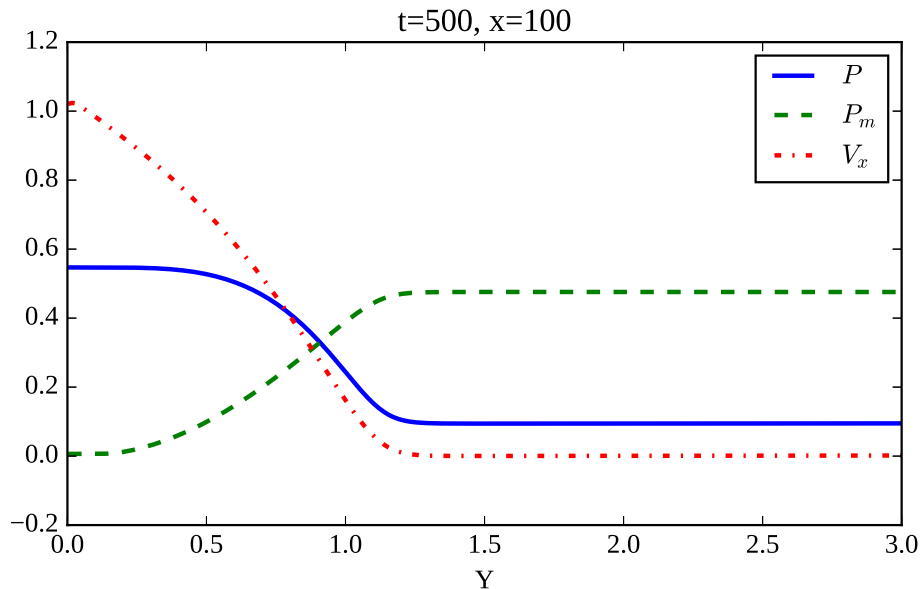


Figure 5.7: Profile of the gas pressure, magnetic pressure and V_x at $x = 100$ along y direction for run 1.

reconnection including Petschek model and Sonnerup model [Sonnerup \(1970\)](#) as special cases. [Fig.5.7](#) shows gas pressure, magnetic pressure and V_x along $x = 100$. It is seen that the profiles of gas and magnetic pressure show the same behavior as the Petschek model, which shows almost constant pressure in the inflow region (see [Fig.9 of Yan et al. \(1992\)](#)).

5.4 Conclusion of Local Model

Our model results demonstrate Petschek-type reconnection even under a spatially uniform resistivity. Using boundary conditions to fix the plasmoid, we successfully model the fundamental formation process of the Petschek-type structure which appears in our previous large-scale simulation [Shibayama et al. \(2015\)](#). In our plasma results, the X-point is adjacent to a plasmoid, which blocks any extension of the diffusion region because the X- and flow stagnation points are separated by the evolution of the plasmoid. As a result, a strong plasma flow is present at the X-point, the diffusion region is localized, and a Petschek-type reconnection region forms even under uniform resistivity. Prior to the formation of the Petschek-type structure, the local magnetic Reynolds number, R_m , of the current sheet is approximately 300.

6 Simulated Observation

6.1 Ionization Equation

Neutral Fe has 26 electrons. In a high temperature environment such as in the solar corona, Fe is in a ionization state where many of the electrons are ionized. Transitions between neighboring ionization states are described by ionization equation, which include ionization coefficient $S[cm^3/s]$ and recombination coefficient $\alpha[cm^3/s]$. These coefficients are approximated as a function of temperature in the coronal parameter range. Ionization coefficient consists of two components: Direct ionization rate coefficient C_{DI} and excitation auto ionization rate coefficient C_{EA} , while recombination coefficient also has two components: radiative recombination rate coefficient α_r and dielectronic recombination rate coefficient α_d . The approximate value of them are shown in [Arnaud and Rothenflug \(1985\)](#); [Arnaud and Raymond \(1992\)](#); [Mazzotta et al. \(1998\)](#) as follows.

$$\alpha_r = A \left(\frac{T}{10^4 K} \right)^{\alpha - \beta \log_{10} \left(\frac{T}{10^4 K} \right)} \quad (6.1)$$

$$\alpha_d = \frac{1}{T^{3/2}} \sum_{j=1}^4 c_j \exp \left(-\frac{E_j}{T} \right) \quad (6.2)$$

$$C_{DI} = \frac{6.69 \times 10^7}{(kT)^{3/2}} \sum_j \frac{\exp(-x_j)}{x_j} F(x_j) \quad (6.3)$$

$$C_{EA} = 6.69 \times 10^7 \exp(-x) \frac{F(x)}{\sqrt{kT}}, \quad (6.4)$$

where $x_i = I_i/(kT)$, and I_i is the ionization potential. Constants and functions included in these equations are shown in the references. In the coronal parameter, these coefficients are approximated as a function of electron temperature only. Using these parameters, ionization equation is

$$\frac{\partial n_i^{Fe}}{\partial t} = n_e [n_{i+1}^{Fe} \alpha_{i+1}^{Fe} + n_{i-1}^{Fe} S_{i-1}^{Fe} - n_i^{Fe} (\alpha_i^{Fe} + S_i^{Fe})], \quad (6.5)$$

where $\alpha = \alpha_r + \alpha_d$, $S = C_{DI} + C_{EA}$, n_i^{Fe} is the number density of Fe^{+i} ion, and n_e is the number density of electron.

6.2 Ionization Equilibrium

In this section, we will consider the property of ionization equilibrium. In the equilibrium, we get from Eq.6.5,

$$0 = n_{i+1}^{Fe} \alpha_{i+1}^{Fe} + n_{i-1}^{Fe} S_{i-1}^{Fe} - n_i^{Fe} (\alpha_i^{Fe} + S_i^{Fe}). \quad (6.6)$$

Using the following matrix and vector, this equation is expressed $Ax = 0$.

$$A = \begin{pmatrix} d_0 & \alpha_1 & & & 0 \\ S_0 & d_1 & \alpha_2 & & \\ & S_1 & d_2 & \ddots & \\ & & \ddots & \ddots & \alpha_{26} \\ 0 & & & S_{25} & d_{26} \end{pmatrix}, \quad x = \begin{pmatrix} n_0^{Fe} \\ n_1^{Fe} \\ \vdots \\ n_{26}^{Fe} \end{pmatrix}, \quad \text{where } d_i = -(\alpha_i + S_i). \quad (6.7)$$

This equation can be solved for x using ionization and recombination coefficients shown above. The number density of all Fe ions are derived. However, if x is a solution, Cx is also a solution, where C is an arbitrary constant. Here, let us normalize x so that $\sum n_i^{Fe} = 1$. After normalization, n_i^{Fe} is called population fraction, which is a set of non-dimensional numbers. Hereafter, we use the symbol n_i^{Fe} for the population fraction. Adding one line to A , we can express this equation with matrix representation and solve $A'x = b$ for x .

$$A' = \begin{pmatrix} d_0 & \alpha_1 & & & 0 \\ S_0 & d_1 & \alpha_2 & & \\ & S_1 & d_2 & \ddots & \\ & & \ddots & \ddots & \alpha_{26} \\ 0 & & & S_{25} & d_{26} \\ 1 & 1 & \dots & 1 & 1 \end{pmatrix}, \quad x = \begin{pmatrix} n_0^{Fe} \\ n_1^{Fe} \\ \vdots \\ n_{26}^{Fe} \end{pmatrix}, \quad b = \begin{pmatrix} 0 \\ \vdots \\ 0 \\ 1 \end{pmatrix}, \quad \text{where } d_i = -(\alpha_i + S_i). \quad (6.8)$$

Note that A' is a 27×28 matrix, which means $A'x = b$ have one redundant equation. We can exclude one equation from $A'x = b$ or solve the following normal equation. Technically speaking, all coefficients are numerically derived under a certain approximation, which means there can be no exact solution of $A'x = b$. Normal equation is equivalent to least squares method and we can obtain approximate solution x' of x .

$$\text{Normal equation} : A'^T A'x = A'^T b, \quad (6.9)$$

$$x' = (A'^T A')^{-1} A'^T b. \quad (6.10)$$

In this study with coronal parameter, we can solve the equation by both method with sufficient precision. Fig.6.1 shows population fraction of each ionization degree as a function of temperature.

Hence the ionization equilibrium is just a function of temperature, the plasma temperature is derived from a ratio of population fraction of any two Fe ion. Fig.6.2 shows the ratios of population fractions of various pairs of ions. It is seen that temperature is uniquely determined from the ratio.

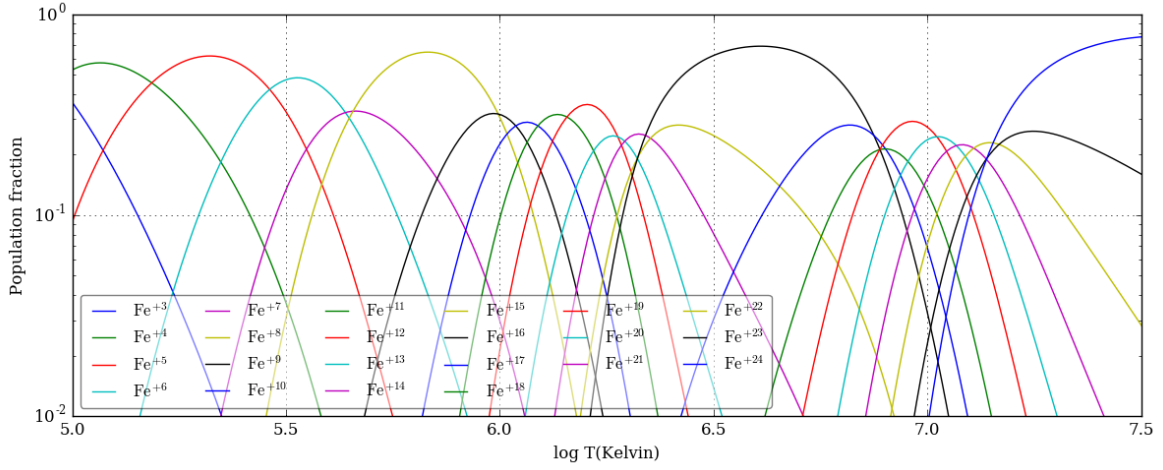


Figure 6.1: Ionization equilibrium of Fe ions for each temperature

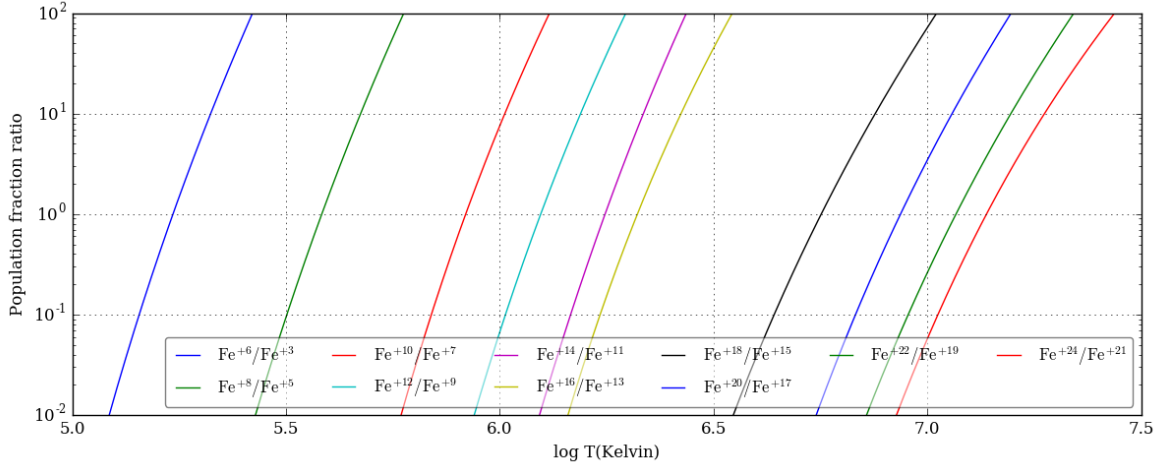


Figure 6.2: population fraction ratio of various ion pairs

6.3 Time Dependent Ionization

In this section we discuss the temporal evolution of ionization fraction, which is governed by Eq.6.5. Using matrix representation, we can rewrite the equation as follows:

$$\frac{\partial}{\partial t} x(t) = n_e A x(t). \quad (6.11)$$

Solving this equation implicitly or explicitly, we can get time evolution of population fraction of each Fe ions. Fig.6.3 shows transition of population fraction when a plasma blob with 1.5 MK is suddenly heated up to 31.3MK at $t = 0$. The electron density is assumed to be $2.45 \times 10^9 \text{ \#}/\text{cc}$. It is seen that it takes of the order of 100 seconds to reach the ionization

equilibrium. Fig.6.3 shows the ratio of the population fraction of various pairs of ions as a function of time. This figure demonstrates that measuring a pair of ions, we can obtain the information of the time after the plasma blob is heated. Note that the derived time is sensitive to electron density.

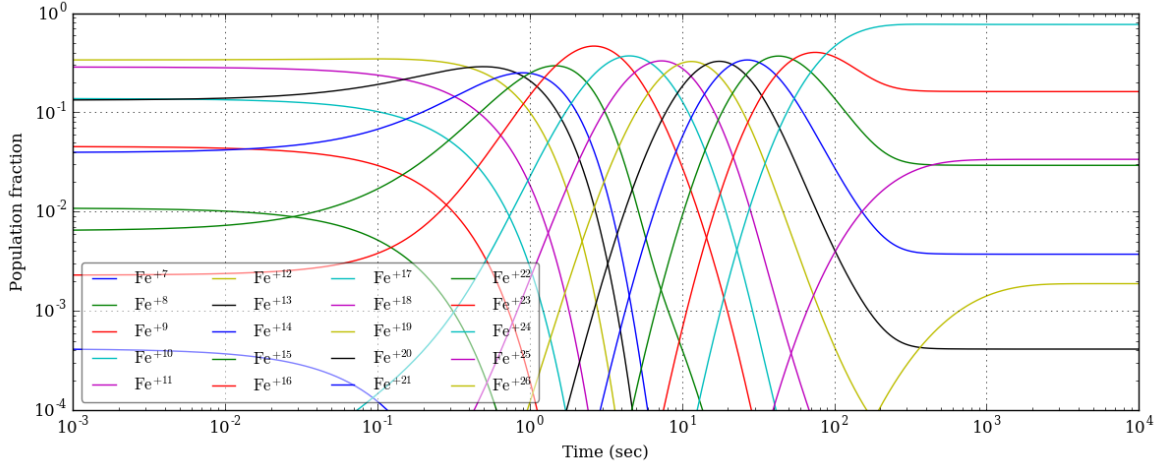


Figure 6.3: Temporal evolution of population fraction.

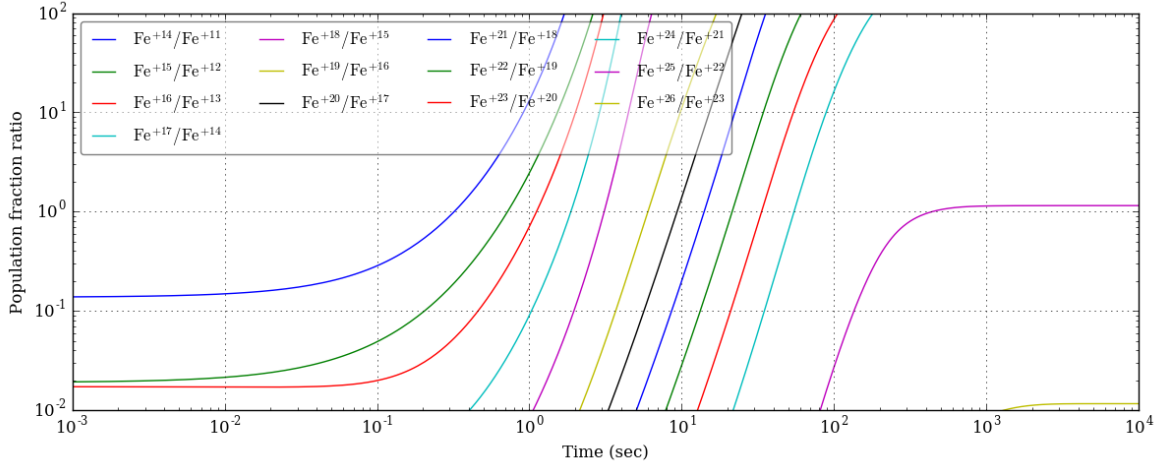


Figure 6.4: Temporal evolution of population fraction ratio.

Imada et al. (2011) shows how Petschek-type outflow region is observed under time dependent ionization. Discrepancy between non-equilibrium and equilibrium ionization is large especially in FeXX to FeXXII (see Fig.6.5). However, their model uses zero dimensional simulation of plasma parcel moving across and heated in a slow shock layer. Although there are limited number of studies solving ionization of ion as in the post process of MHD simulation (Shen et al., 2013), 2D simulation of time-dependent ionization together with MHD is not

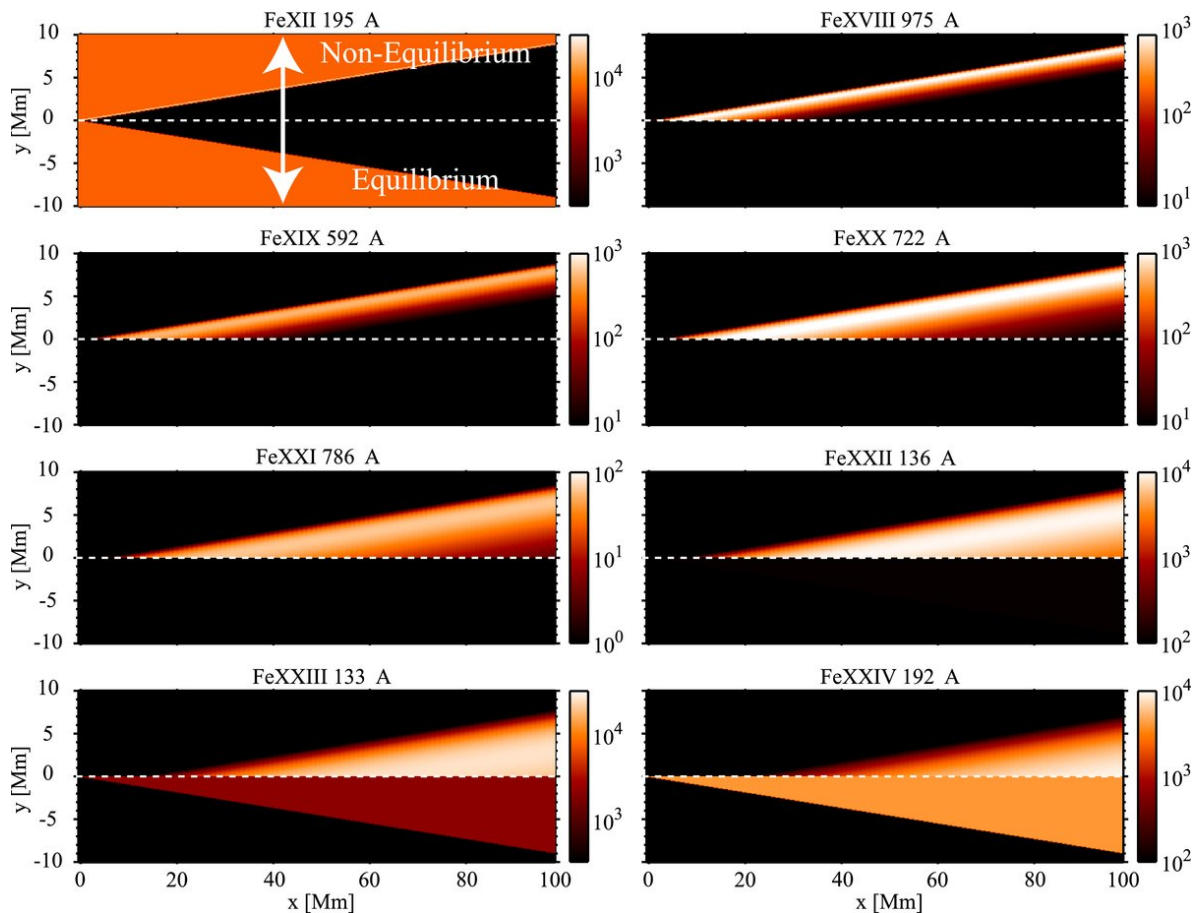


Figure 6.5: Figure 3 of [Imada et al. \(2011\)](#)

conducted. The time evolution of the distribution of each Fe ion in spontaneous formation of plasmoid or Petschek-type diffusion region is not elucidated yet.

6.4 Solar-C_EUVST

High temperature plasma with 1–10 million Kelvin in the solar corona is observed mainly in the UV wavelength. EUV imaging spectrometer (EIS) onboard Hinode satellite conducts spectroscopic observation of emission lines of ions such as Fe, and diagnose plasma property, velocity and so on. There is a plan of next generation satellite Solar-C_EUVST (here after EUVST), whose comparison with Hinode/EIS is shown in Tab.6. EUVST has significant improvements in temporal and spatial resolution as well as the wavelength and temperature coverage. Owing to the wide wavelength coverage, EUVST has ability to measure the electron temperature using different lines, in a manner independent on the ionization process. As is shown in the previous section, typical time scale of ionization process is a few hundred seconds, which is well resolved by EUVST. By comparing electron temperature and ionization state,

	Hinode/EIS	EUVST
Temporal resolution for a slit position	10-60 s for AR, 20-120 s for QS	0.2-5 s for AR, 0.2-20 s for QS
Spatial resolution	2-3"	0.4"
Field of view	$\pm 290'' \times 512''$	$\pm 150'' \times 280''$
Wavelength bands [\AA]		170-215
		463-542
	170-210	557-637
	250-290	690-850
		925-1085
Primary temperature coverage ($\log_{10} T$)	4.9, 5.6-7.2	4.2-7.2
		1115-1275

Table 6: Comparison between Hinode/EIS and EUVST

EUVST will allow us to discuss detailed evolution of reconnection region such as the history of heating.

6.5 Governing Equations and Numerical Method

We develop numerical simulation code which solves ionization equation along with resistive MHD equation aiming to simulate the current sheet observed by EUVST. In addition to MHD equations shown in Sec.2, we solve the following ionization advection equation as a passive quantities of MHD.

$$\frac{\partial n_i^{Fe}}{\partial t} + \nabla \cdot (n_i^{Fe} \mathbf{v}) = n_e [n_{i+1}^{Fe} \alpha_{i+1}^{Fe} + n_{i-1}^{Fe} S_{i-1}^{Fe} - n_i^{Fe} (\alpha_i^{Fe} + S_i^{Fe})] \quad (6.12)$$

The second term in the left-hand side represents the advection effect. Precisely, there are other effects such as ionization energy loss and gain, and radiative cooling, which is neglected because MHD dynamics is assumed to be dominant in the solar corona in this study.

We use HLL method to evaluate the second term of left-hand of Eq.6.12, while right-hand side is solved implicitly because the ionization time scale can become smaller than that of MHD. Fig.6.6 shows typical time scale of ionization process as a function of temperature, which is estimated from the eigen value of A . The electron density is assumed to be $n_e = 10^9 \# / cc$. The typical value is about 6×10^{-4} to 10^{-3} s, which can be a few order of magnitude smaller than MHD time scale. It is seen that the ionization time scale is not sensitive to temperature. In the range from $5.25 < \log_{10} T < 7$ the time scale changes only a factor of 2. By contrast, the time scale is inversely proportional to electron density n_e , which may change by order of magnitude.

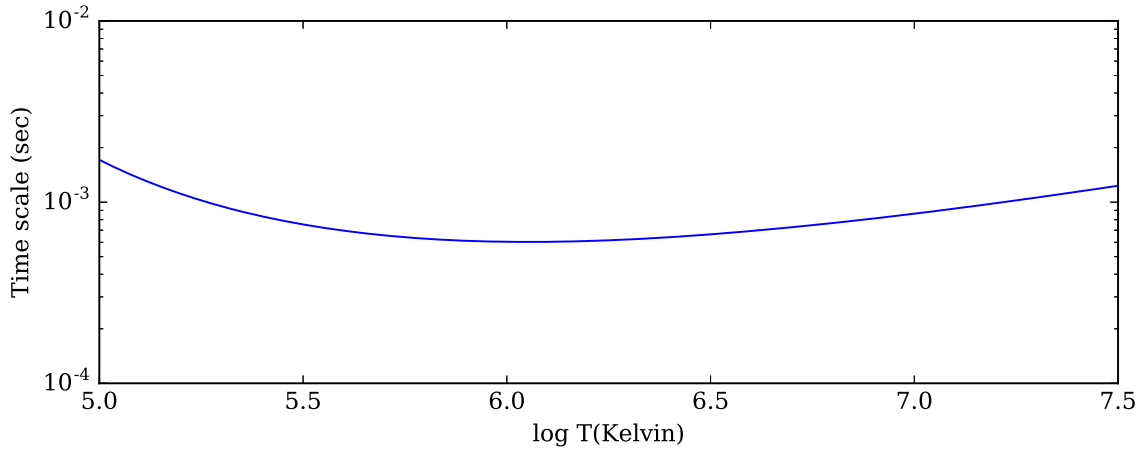


Figure 6.6: Typical time scale of ionization process for $n_e = 10^9 \text{ \#/cc}$

6.6 Initial Condition and Normalization

For the initial condition of the simulation, we use Harris-type equilibrium current sheet [Harris \(1962\)](#). For the calculation of ionization coefficients, temperature should be in the unit of Kelvin. The following parameters are used for the normalization of each physical quantities based on the coronal parameters. Note that the plasma beta is a few times larger than the

Quantity	Value	Unit
B_0	10	G
N_0	5.7×10^9	$\text{\#}/\text{cc}$
V_{A0}	287	km/s
L_0	0.1	Mm
τ_0	0.34	s
β_0	0.2	
T_0	2.5	MK

Table 7: Normalization of quantities

actual coronal value for the numerical stability. Hence, density in the simulation is larger than that in the corona, and ionization process is faster according to Eq.6.12. We can interpret this by giving a large value for the normalization of length scale L_0 . Adjusting the ratio between Alfvén time and ionization time, we can reconstruct the spatial distribution of each Fe ions close to the real parameter.

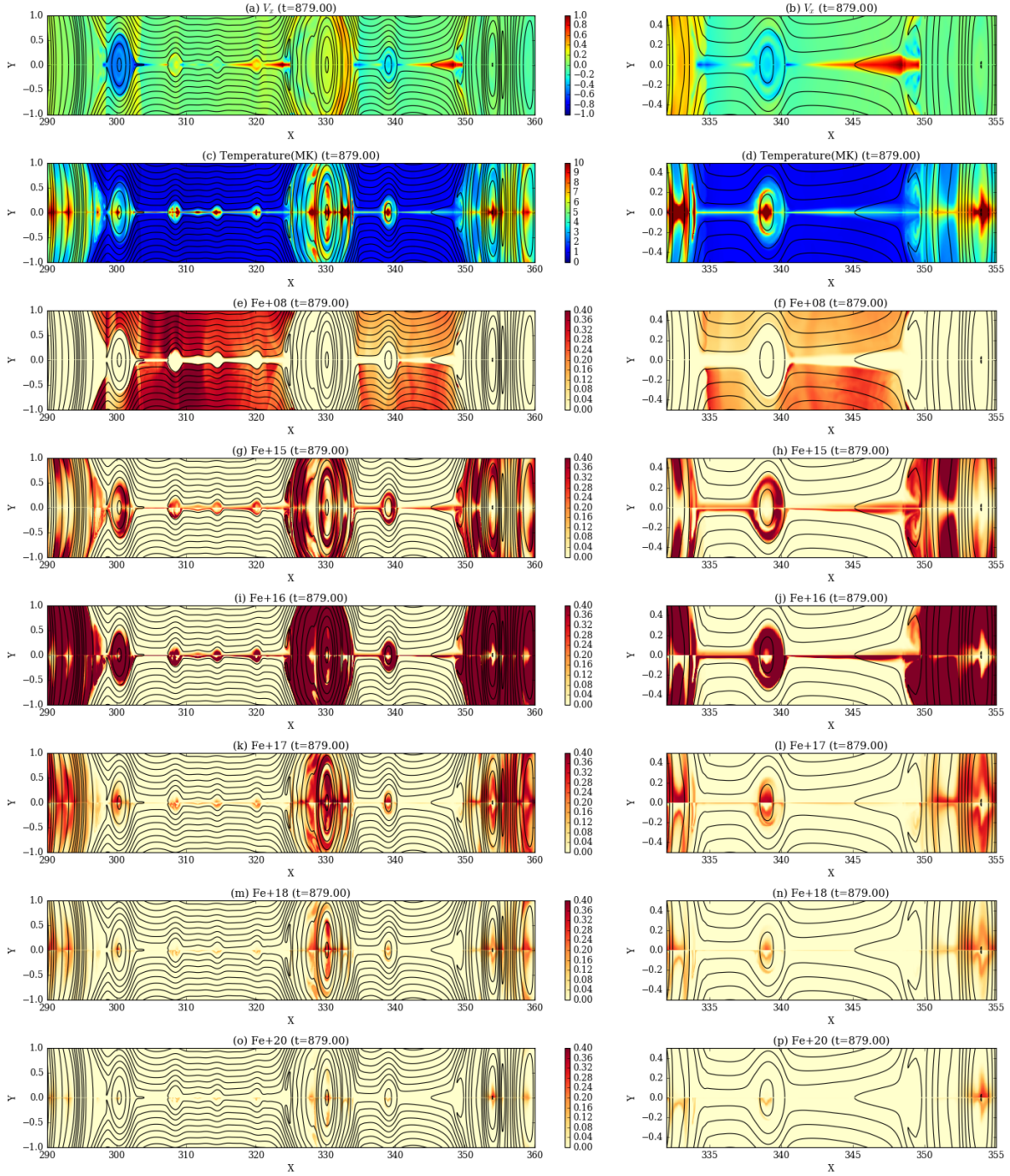


Figure 6.7: Pseudo-color plot of the simulation result. (e)-(p) show Fe ion density (population fraction times plasma density) of each ionization state in non-equilibrium ($y > 0$) and equilibrium ($y < 0$). Right panels are enlarged plots of Petschek-type region.

6.7 Results and Discussion

Fig.6.7 shows distributions of V_x , temperature, density of Fe^{+8} , Fe^{+15} , Fe^{+16} , Fe^{+17} , Fe^{+18} , and Fe^{+20} in equilibrium and non-equilibrium ionization. Density of ion is defined as population fraction times number density of plasma ($\rho_i = \rho n_i$). Lower half ($y < 0$) represents equilibrium and upper half shows non-equilibrium. It is seen from Fig.6.7(e)–(p) that small plasmoids show discrepancy between equilibrium and non-equilibrium, while large ones at both sides and the center show similar distribution of Fe ions in equilibrium and non-equilibrium ionization. It is seen from right panels that the plasmoid has shell-like distribution of Fe ions. This is partly because the core of the plasmoid is higher temperature, and also because outer plasma is newly reconnected one, which just started to ionize. Furthermore, small Petschek-type structure at $340 < x < 350$ is observed in ionization equilibrium but not in non-equilibrium clearly. We confirm the effect of non-equilibrium ionization pointed out by Imada et al. (2011) also in the case of dynamical Petschek diffusion region.

For a quantitative understanding of ionization state of each plasmoids, we evaluate total ionization fraction of each plasmoid. Fig.6.8 shows the ratio between the total amount of Fe^{+20} and Fe^{+17} ions inside each plasmoid. The ratio is calculated by an integral of density of each ion inside each separatrix.

$$r_{Fe+20/Fe+17} = \frac{\int \rho_{20} ds}{\int \rho_{17} ds} \quad (6.13)$$

It is clearly seen that the difference between equilibrium and non-equilibrium ionization is significant for small plasmoids, by contrast, large plasmoids in the both sides of the plot do not show large discrepancy. Small plasmoids contains plasmas which are just heated and do not reach equilibrium yet.

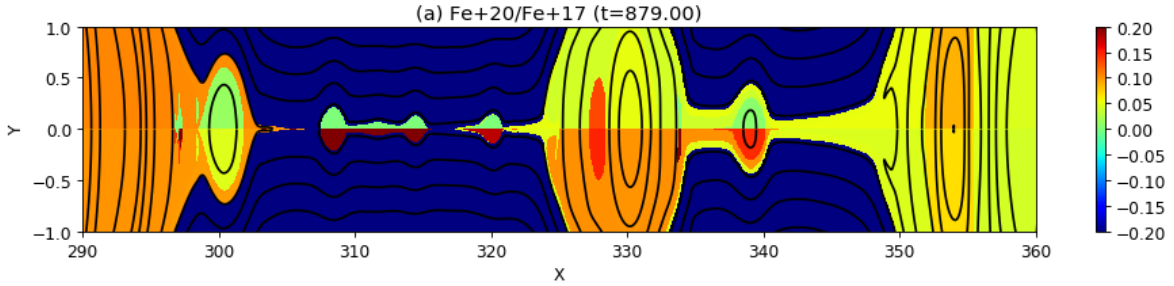


Figure 6.8: Ratio of total Fe ion number in each plasmoid in equilibrium and non-equilibrium ionization.

A quantitative comparison of Fig.6.8 is shown in the left panel of Fig.6.9, which illustrates difference of $r_{Fe+20/Fe+17}$ of non-equilibrium and equilibrium as a function of plasmoid area. We can see that the difference is large for small plasmoid whose area is roughly less than 0.1

Mm^2 . In other words, plasmoids larger than 0.1 Mm^2 can be treated as ionization equilibrium, whose temperature is derived from the line ratio of Fe ions. The threshold of plasmoid area is determined by the size of plasmoid that reach until the time plasma becomes ionization equilibrium. Right panel shows the same quantity but in a logarithmic scale. It is seen that major part can be fit with a line with negative slope, which means plasmoids exponentially reach ionization equilibrium. Note that the value of threshold can change when we change the normalization of length.

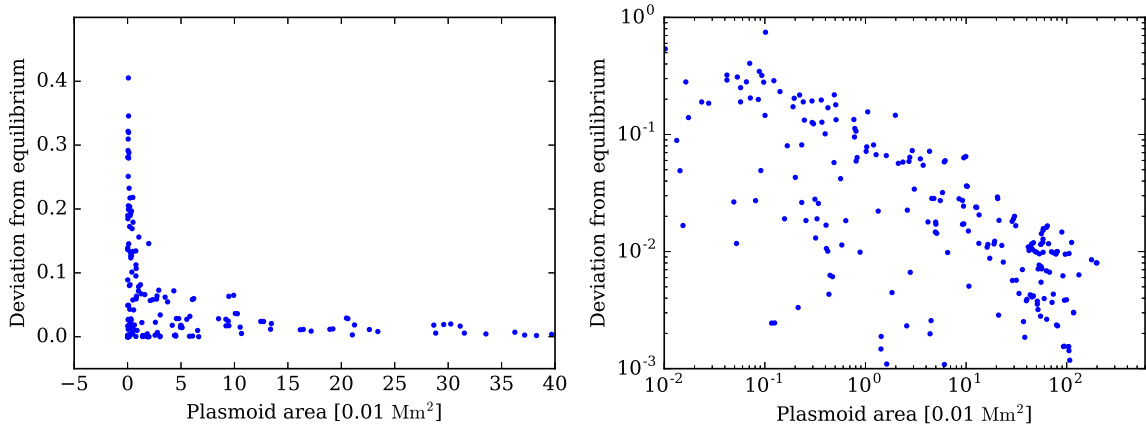


Figure 6.9: Comparison of ion number ratio of plasmoids as a function of its area.

Here we estimate the threshold value of the plasmoid width w_{crit} in solar flares. τ_{ion} , B_0 , M and V_A are typical time of ionization, upstream magnetic field strength, average reconnection rate and upstream Alfvén velocity respectively. The magnetic flux Φ of a plasmoid whose first plasma at the core reaches equilibrium is

$$\Phi \sim B_0 M V_A \tau_{ion}. \quad (6.14)$$

Assuming upstream plasma beta is very small and that of plasmoid is β_p , magnetic field strength of plasmoid is $B_0/\sqrt{\beta_p}$. We get the plasmoid width w of a plasmoid with magnetic flux Φ ,

$$w \sim \sqrt{\beta_p} M V_A \tau_{ion}. \quad (6.15)$$

Let's define $w_{crit} = 2w$ because half of such plasmoid is filled with ionization equilibrium plasma. using $\beta_p = 10$, $M = 0.01$, $V_A = 1000 \text{ km/s}$ and $\tau_{ion} = 100 \text{ sec}$,

$$w_{crit} \sim 6000 \text{ km}. \quad (6.16)$$

Fig.6.10 shows plasmoid chain structure observed by SDO/AIA (Takasao et al., 2012). The

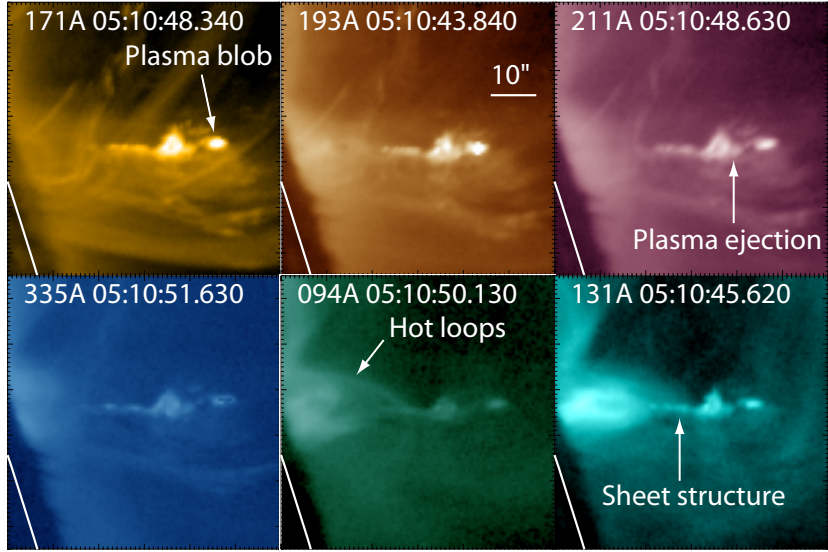


Figure 6.10: Observed plasmoid-like structure during a solar flare (Takasao et al., 2012).

size of the plasmoids, roughly $10''$ in the field of view, is about 7000 km, which is just around the threshold we discuss above. The half of the plasma in the plasmoids is, therefore, in the equilibrium and the rest is non-equilibrium. It is seen from the figure that the plasmoids are observed in many wavelength bands, which are sensitive to various temperature range. This can be because the Fe ions are not in the ionization equilibrium and emission lines do not reflect the correct plasma temperature.

Fig.6.11 shows two-dimensional ((b), (c)) and one-dimensional ((d), (e)) distribution of population fraction ratio in non-equilibrium (top half in 2D plots) and equilibrium (bottom half in 2D plots). For the one-dimensional distribution, ion density is integrated in y direction and the ratio is plotted as a function of x . We can see from Fig.6.11(b) and (d) that the plasmoid at $x \sim 330$ is almost in the equilibrium, while other smaller plasmoids at $x \sim 340$, $305 < x < 320$ are not observed in non-equilibrium. By contrast in Fig.6.11(c) and (e), plasmoids at $x \sim 330$, 340 are almost perfectly matches with equilibrium and ones at $305 < x < 320$ still have some difference from equilibrium. From these results, we can understand the plasmoid at $x \sim 330$ is the largest and oldest, the one at $x \sim 340$ is the second. Obtaining these quantities from the observation of EUVST, we may derive the information of size and age of plasmoids, which leads us to understand the mode of tearing instability of coronal plasma and local reconnection parameters.

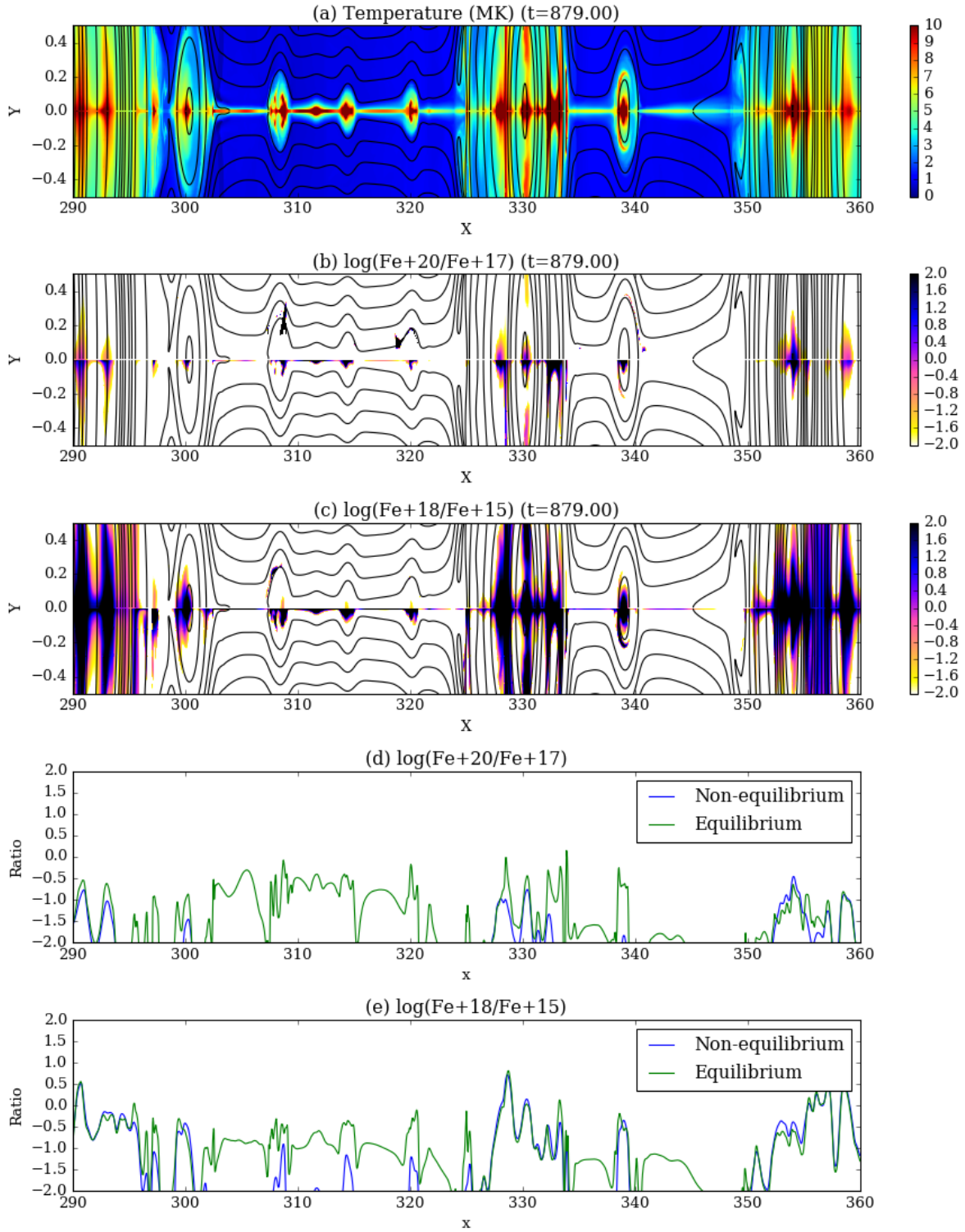


Figure 6.11

7 3D Models

7.1 Introduction to 3D Magnetic Reconnection

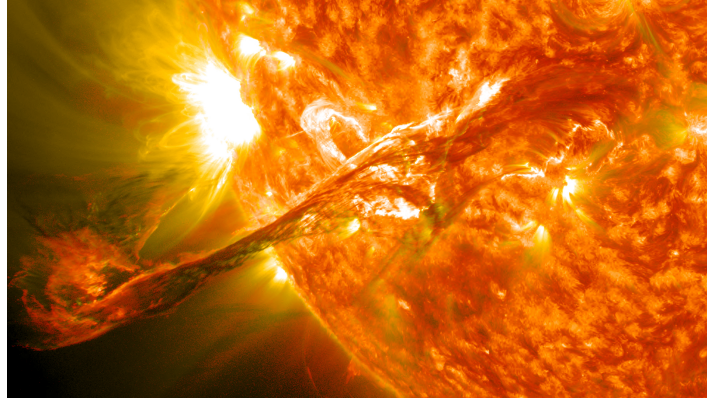


Figure 7.1: Flux rope in the solar eruption

The discussions so far are based on two-dimensional models, the real space is, by contrast, three-dimensional. The three-dimensional counterpart of 2D plasmoid is called flux rope, which appears in the CSHKP flare model as a top helical magnetic field (see Fig.2.2). Flux ropes are observed in the solar corona as a dark filaments, which are manifestation of cold plasma stacked at the core of flux ropes. Dark filaments sometimes erupt into interplanetary space. This phenomenon is called filament eruption. Fig.7.1 shows a filament eruption event observed by SDO satellite. It is seen that the filament has a helical structure.

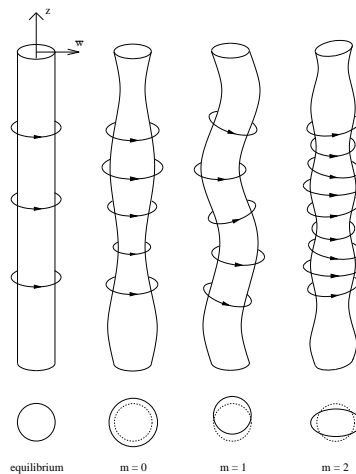


Figure 7.2: Instabilities of flux tube Braithwaite (2006)

There are instabilities that appear in 3D space but not in 2D space. Kink and oblique

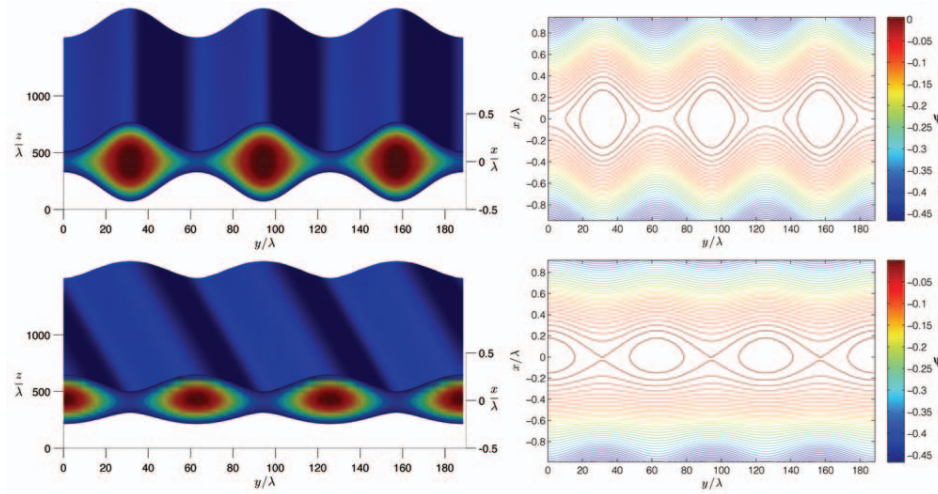


Figure 7.3: Oblique tearing instability Baalrud et al. (2012)

tearing instabilities are related to 3D magnetic reconnection and plasmoid. Leftmost figure of Fig.7.2 illustrates equilibrium flux rope, which is unstable to various modes shown on the right. The second one from the right is called kink instability. Observations suggest that flux ropes in the solar corona sometimes erupt as a result of kink instability. A flux rope is unstable to kink instability when its guide field, magnetic field along the axis of flux rope, is not sufficiently strong compare to the poloidal field, magnetic field around the axis. It is possible that kink-unstable flux rope form in current sheet. Fig.7.3 illustrates oblique tearing instability. Magnetic islands of two-dimensional tearing instability have the axis on the neutral plane and the structure is aligned with z -axis as shown by the top panel. By contrast, oblique tearing plasmoids are shifted in y direction (x direction in Fig.7.3) and the structure is inclined in $x - z$ plane ($y - z$ plane in Fig.7.3). This tearing mode can grow in multiple layers in a current sheet. The resultant plasmoid is aligned to the local magnetic field direction of the layer ($\mathbf{k} \perp \mathbf{B}_0$), which leads to a strong guide field of the plasmoid (Baalrud et al., 2012).

Recent super computers allow us to perform three-dimensional fluid simulation of magnetic reconnection. Oishi et al. (2015) conducts numerical simulation of 3D Harris-type current sheet and shows that within the range of $3.2 \times 10^3 < S < 3.2 \times 10^5$, fast reconnection realize because of 3D instabilities, which has different structure from 2D current sheets. In the study they use non-guide field Harris-type equilibrium as the initial condition, which does not have oblique tearing instability. As a result of the turbulent evolution, the reconnection rate increases in a different reason from two-dimensional plasmoid chain reconnection. However, non-guide field initial condition is very symmetric which is difficult to realize in reality. Huang and Bhattacharjee (2016) conduct similar numerical simulation with guide field, whose value is 0.1 times of the reconnection field. Fig.7.4 shows a snapshot of 3D magnetic field and

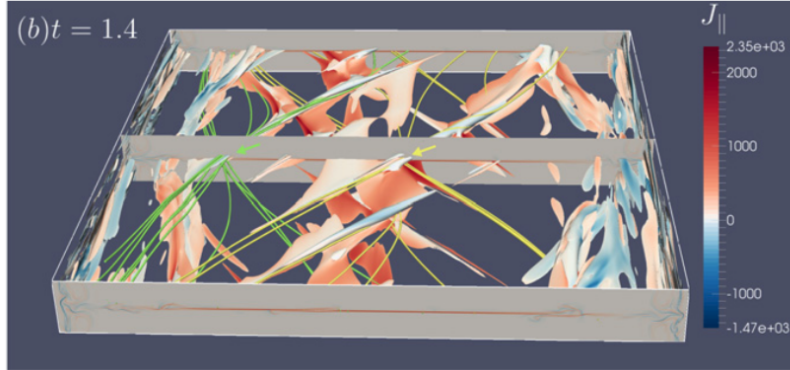


Figure 7.4: Huang and Bhattacharjee (2016)

current density structure.

7.2 Simulation Settings

We conduct three-dimensional numerical simulation of Harris-type equilibrium current sheet with guide field. The initial condition of 3D system is the following,

$$\mathbf{B}(x, y, z) = (B_0 \tanh(y/L_0), 0, B_z) \quad (7.1)$$

$$p(x, y, z) = p_0 [\cosh^{-2}(y/L_0) + \beta], \quad (7.2)$$

which is a simple extension to 2D initial condition to 3D space. Fig.7.5 illustrates the system, which has the dimension of $(L_x, L_y, L_z) = (600L_0, 100L_0, 100L_0)$. The number of grid point is $(N_x, N_y, N_z) = (8192, 1024, 1024)$. The boundary condition of x, z direction is periodic boundary, while we use conducting wall for y direction. We perform several runs with different guide field: $B_z = 0, 0.1B_0$ and B_0 . The resistivity η is set $10^{-3.5}$, which corresponds to $S \sim 3 \times 10^5$ to 1.2×10^6 using the current sheet extent as the length scale. Three-dimensional simulation of current sheet with $S > 10^6$ is not performed yet by other groups.

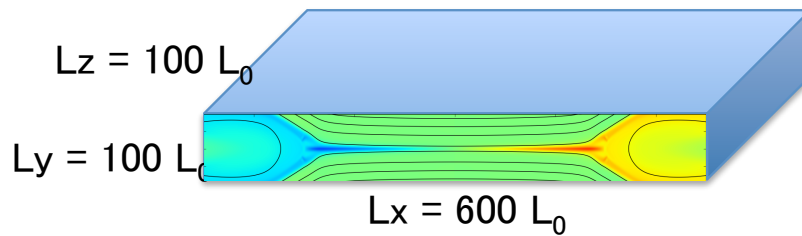


Figure 7.5: Schematic figure of 3D system

7.3 Results and Discussions

The time evolution of the each energy in the whole system is plotted in Fig.7.6 as a function of time ($B_z = 0.1B_0$ run). We use the same grid size and initial setting for the 2D and 3D cases except for the initial noise. It is seen that magnetic energy decrease and converted to thermal and kinetic energy. In 2D, dynamical Petschek reconnection starts from $t \sim 600$ and contributes to the fast energy conversion. By contrast in 3D, the energy conversion rate is almost constant as a result of turbulent evolution. The energy conversion rate is small in 3D compared to 2D.

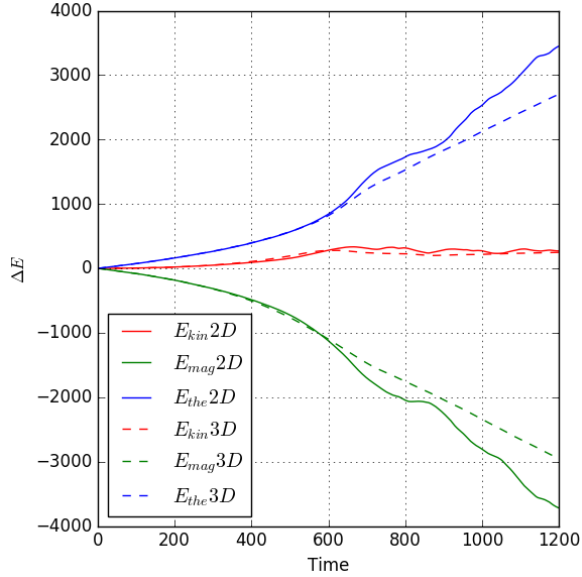


Figure 7.6: Total energy of the system as a function of time in the $B_z = 0.1B_0$ case.

Fig.7.7 is the top view of three-dimensional reconnection region in the initial stage of evolution ($t = 350$). The horizontal axis is x direction and the vertical axis is z direction. A flux rope forms at around the center, which has a small-scale kink-instability like structure in z direction. At this moment, the structure is still coherent in z direction in to a certain extent. Fig.7.6 also shows the difference of energy conversion rate in 2D and 3D is similar.

Fig.7.8 shows a slice of B_x , J_z and V_x on the initial neutral plane ($y = 0$) at $t = 900$ when the reconnection is sufficiently evolved. It is seen from Fig.7.8(a) that oblique plasmoids, which are seen as a red and blue region, crosses each other at neutral plane. These plasmoids form in different layers in $+y$ and $-y$ sides. Current density in Fig.7.8(b) shows patchy distribution of strong current. The current is weak in the plasmoid and strong between plasmoids.

Fig.7.9 shows x - y slice of the same quantities at $z = 50$. It is seen from Fig.7.9(a) that plasmoids form both in $y > 0$ and $y < 0$ sides, which are larger than typical plasmoid in 2D system. These oblique plasmoids have strong guide field, which makes magnetic pressure

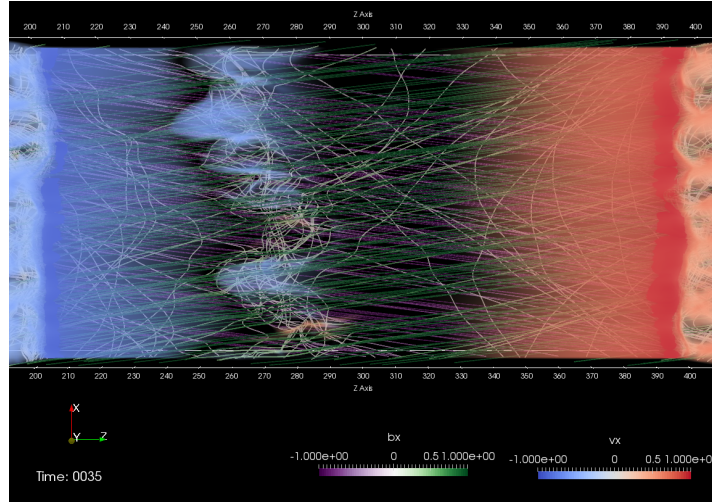


Figure 7.7: Initial stage of the evolution at $t = 350$. Thin lines show magnetic field line and volume rendering shows outflow velocity.

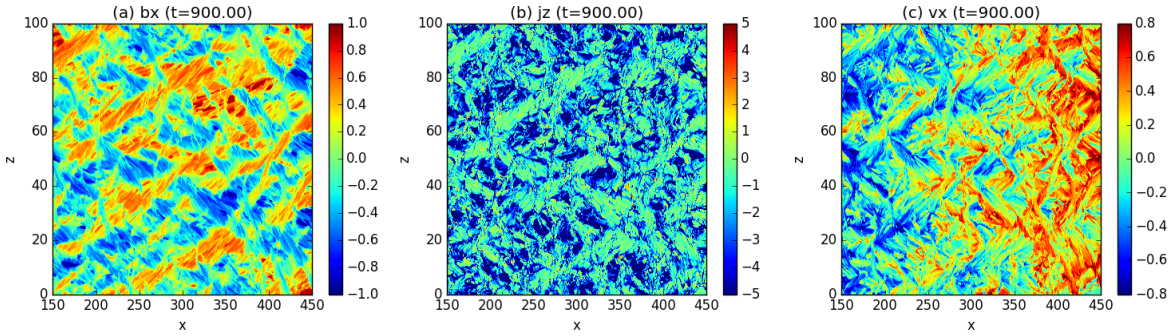


Figure 7.8: x - z slice at the initial neutral plane ($y = 0$.)

inside plasmoids stronger and difficult to compress. The guide field is generated as a result of oblique tearing mode and stabilizes kink instability. Therefore, structure of three-dimensional current sheet is generated mainly by oblique tearing instability, not by kink instability. Small-scale Petschek type structure is not clearly observed in the x - y plot.

In the context of turbulence, mean field approach is often used. In this system, we define mean field $\langle B_x \rangle$ and turbulent field \tilde{B}_x of B_x as follows (see also [Huang and Bhattacharjee \(2016\)](#)),

$$\langle B_x \rangle(x, y) = \frac{1}{L_z} \int_0^{L_z} B_x dz, \quad (7.3)$$

$$\tilde{B}_x(x, y, z) = B_x(x, y, z) - \langle B_x \rangle(x, y). \quad (7.4)$$

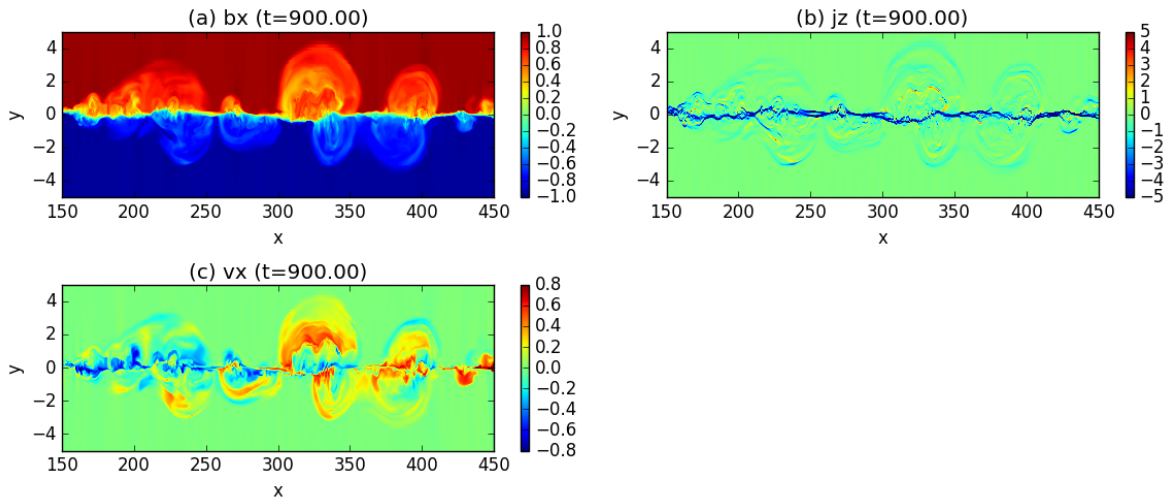


Figure 7.9: x - y slice at the middle of the system ($z = 50$.)

Fig.7.10 shows mean field of B_x , J_z and V_x . Although the three dimensional structure in

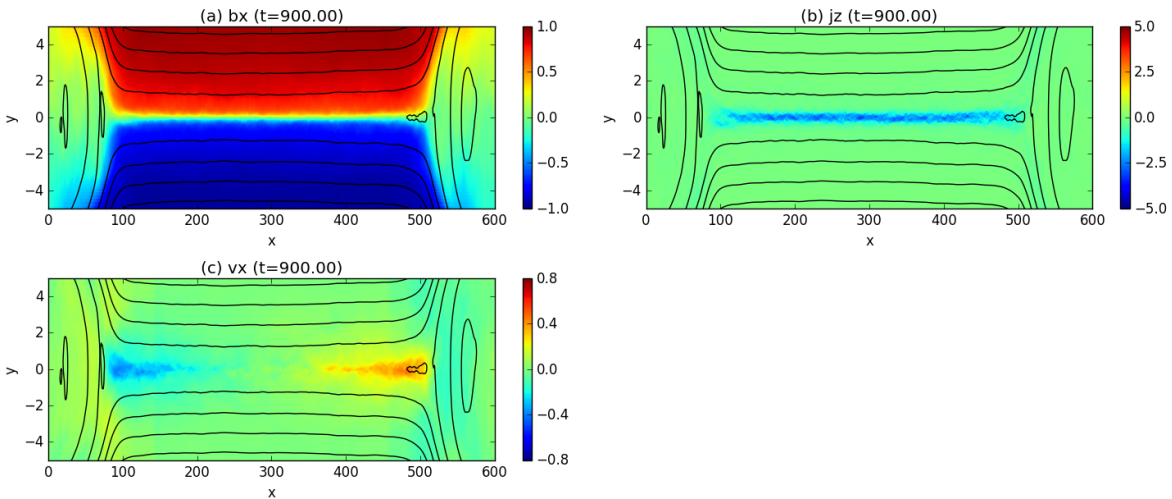


Figure 7.10: Mean field of the current sheet at $t = 900$

Fig.7.7, 7.8, 7.9 show the evolution of plasmoids, such structure is averaged and not seen in mean field. Mean field structure resembles to a single Sweet-Parker type diffusion region, which is also discussed in Huang and Bhattacharjee (2016). It is often discussed that observations of coronal current sheets suggest that the structures are laminar rather than plasmoid chain like, even though the Lundquist number is very large such as 10^{12} . This can be because of the similar effect. In the solar corona, since plasma is tenuous and optically thin, plasma information is integrated in the line of sight direction, which is similar to the mean field quan-

tity. Our results show oblique plasmoids are not observed by the mean field quantities. This can be the reason it is difficult to observe plasmoid-like structure in coronal current sheets. As the second mean field approach, we took the integration path of Eq.7.3 along the oblique plasmoid. Fig.7.11 shows the magnetic field of the mean field. Plasmoid structure is captured by mean field quantities in this case, but only the oblique plasmoids in the upper layer are observed. When the line-of-sight direction of coronal observation matches plasmoid direction, it is possible that we can observe plasmoid structure like this.

Taking the mean field of Eq.3.3, we get

$$\langle \mathbf{E} \rangle(x, y) = -\langle \mathbf{V} \rangle \times \langle \mathbf{B} \rangle - \langle \tilde{\mathbf{V}} \times \tilde{\mathbf{B}} \rangle + \eta \langle \mathbf{J} \rangle. \quad (7.5)$$

Fig.7.12 shows each term of this equation. In the inflow region, $-\langle \mathbf{V} \rangle \times \langle \mathbf{B} \rangle$ term has major part of the electric field, while $-\langle \tilde{\mathbf{V}} \times \tilde{\mathbf{B}} \rangle$ term is large near the center of the diffusion region. $\eta \langle \mathbf{J} \rangle$ is not large but have coherent structure along the neutral plane.

Fig.7.13 shows profile of Eq.7.5 along y direction. The values are averaged in $200 < x < 400$. This profile is different from the similar plot in Huang and Bhattacharjee (2016), which shows flat profile of $\langle E_z \rangle$. Our result shows $\langle E_z \rangle$ is larger at neutral plane because of the strong electric current.

As we discussed with Fig.7.9, we did not find small scale Petschek like structure in the three-dimensional numerical simulation. The possible explanations are the following. One of them is a turbulent evolution of the current sheet, which can destroy shock structure. The

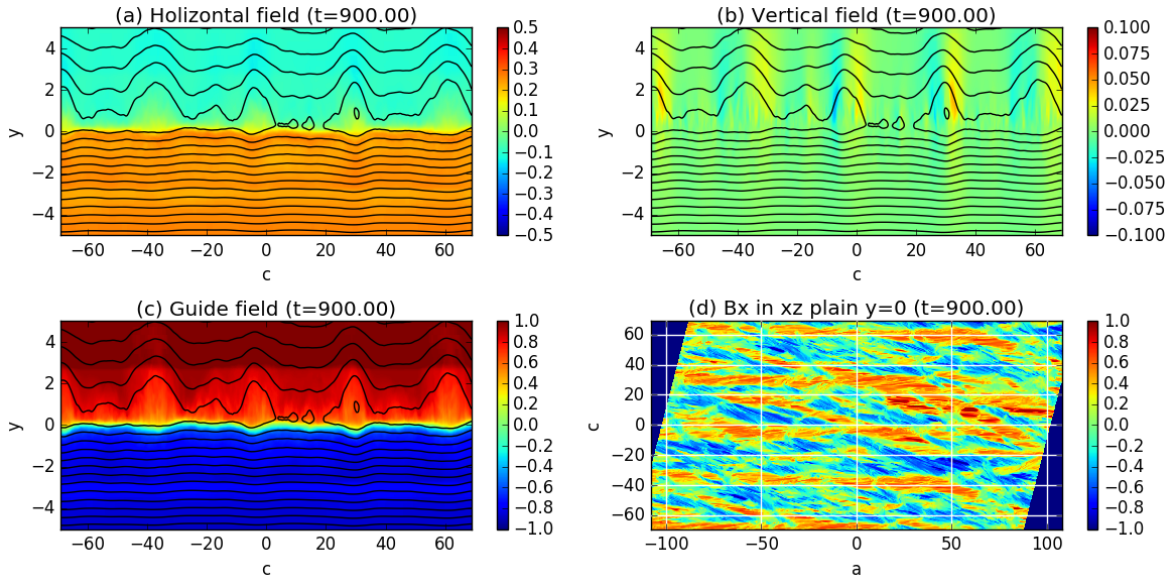


Figure 7.11: Mean field magnetic field obtained by integration along oblique plasmoid.

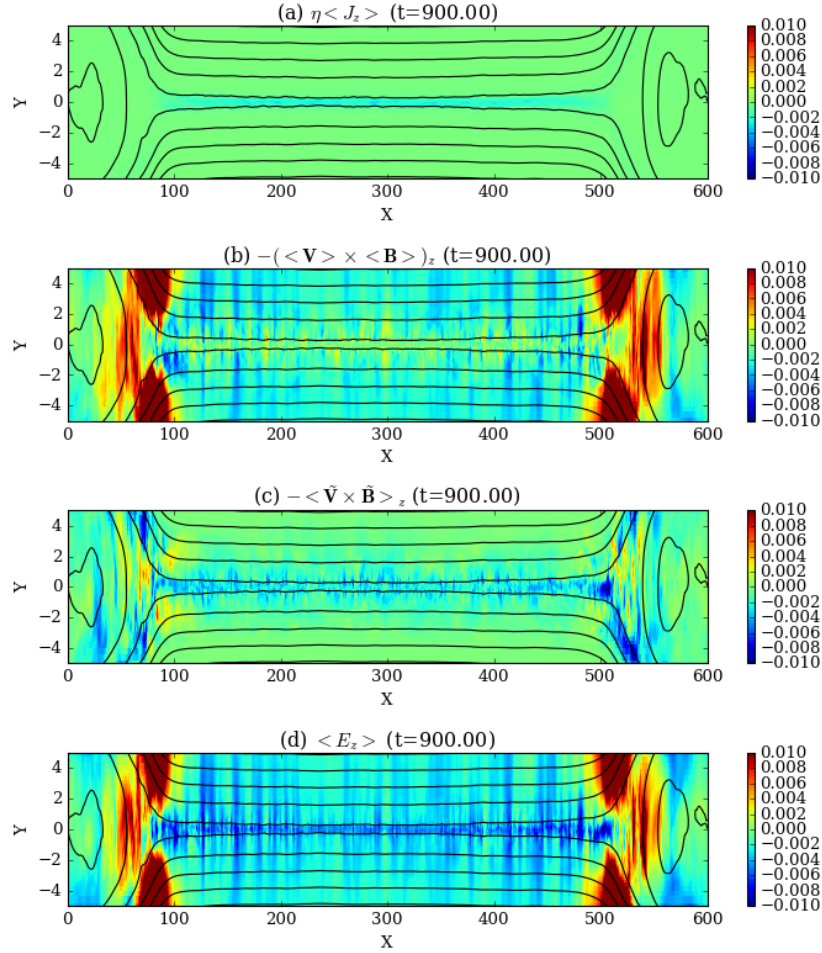


Figure 7.12: Mean and turbulent terms in the Ohm's law

other reason is asymmetry in y direction. The oblique plasmoids are forming apart from neutral plane. We took the mean field integration along oblique plasmoids (Fig.7.11), which shows the mean horizontal magnetic field strength is different in upper half and lower half of current sheet. The structure is similar to asymmetric reconnection at day-side magnetosphere. In this case the asymmetry is in the transverse (y) direction of the current sheet. It is reported that X- and O- points are separated in y direction for asymmetric reconnection. This new degree of freedom can affect the discussion of 2D dynamical Petschek reconnection. As a next step of the study, it is interesting to conduct a high-Lundquist number numerical simulation of an asymmetric current sheet for the application of 3D reconnecting current sheet. The mean field should be taken along the fastest growing oblique tearing mode. If the separation of X- and O- points sufficiently evolve, X- point is pushed to the plasmoid and diffusion region is localized in the same way as the 2D case and Petschek-like diffusion region appear. The

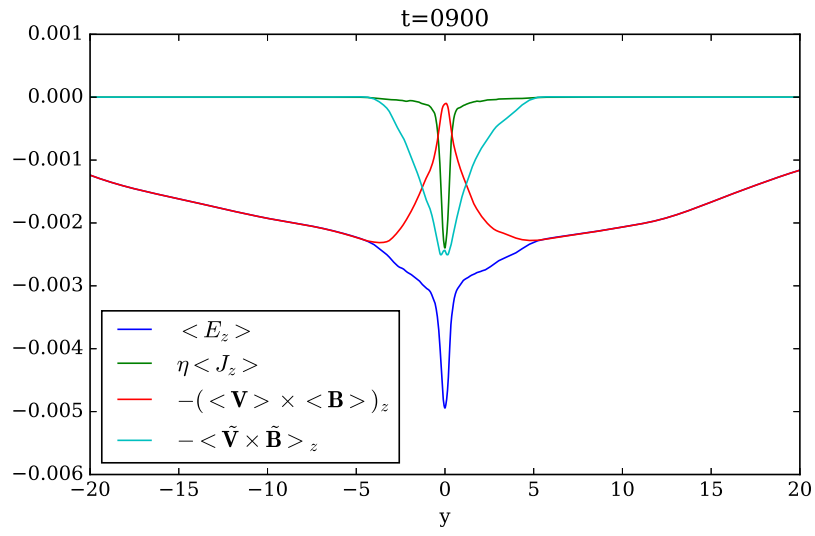


Figure 7.13: Profile of each terms of the Ohm's law along y

shock angle will be different in $+y$ and $-y$ sides because of the asymmetry of upstream.

8 Discussion

8.1 Scenario of Dynamical Petschek Reconnection

We reported the result of non-linear resistive MHD simulation of large current sheet system with uniform resistivity in Sec.4. We discovered Petschek-type diffusion region form accompanied by a formation of small plasmoid. The reconnection rate is almost independent on Lundquist number as a result. Petschek-type reconnection is previously thought not to realize under uniform resistivity. In Sec.5, we reproduce a single Petschek type diffusion region discussed in Sec.4 with a simple initial condition. In the process, separation of X-point and flow stagnation point increases along with the formation of a plasmoid. We pointed out that this process is important for the localization of diffusion region. In this section, we will discuss how to connect these two models.

The significant differences between the global and local models are the size of the system and boundary conditions. Ideal MHD equation does not have typical length scale (scale free). Even if actual system size of the application is different, if the shape is the analogous, evolution of the system is the same after normalization. By contrast, resistive MHD equations have the other time scale, resistive time. The ratio between resistive time and Alfvén time is Lundquist number S .

$$S = \frac{V_A L}{\eta}. \quad (8.1)$$

It is seen from this equation that changing typical length scale L is essentially the same with changing η . η in the global and local models are 10^{-4} and $1/300$ respectively. The thickness of the initial current sheet is, however, L_0 in the both cases. In other words, local model is equivalent to a initial current sheet thickness of $\sim 0.03L_0$ with the same electric resistivity with global model $\eta = 10^{-4}$. Consequently, the local model is corresponding to a part of global model. In the global model, the thickness of the current sheet before the formation of Petschek-type structure actually ranges from 0.03 to 0.05.

Plasmoids in global model form around the center of the simulation box and these plasmoids can move and merge. It is difficult to conduct a precise analysis under such a dynamic evolution. In the local model we fixed a plasmoid with a boundary condition and discussed physical condition of the diffusion region. As a result we successfully reproduced a stable Petschek-type diffusion region. One of the difference between Petschek-type structures in local and global models was that Petschek-type diffusion region appeared in the both sides of a plasmoid in local model, due to the symmetry about the origin. This is probably because physical condition is not symmetric about a plasmoid in global model. In the dynamic evolution, one of the both sides of a plasmoid becomes preferable for the formation of Petschek-type structure due to the motion of plasmoid itself or surrounding plasma motion and so on. It is often observed that Petschek-type diffusion regions form leading side of the plasmoid motion.

We speculate this is due to the relative motion of inflow plasma toward the diffusion region as shown in Fig.8.1. This flow contributes to the first term in the right-hand side of Eq.5.7, which is the important effect for the diffusion region localization. The speed of the plasmoid motion may affect the reconnection rate. The localization effect is strengthened when the speed of plasmoid motion is large, which result in the stronger localization of diffusion region and larger reconnection rate.

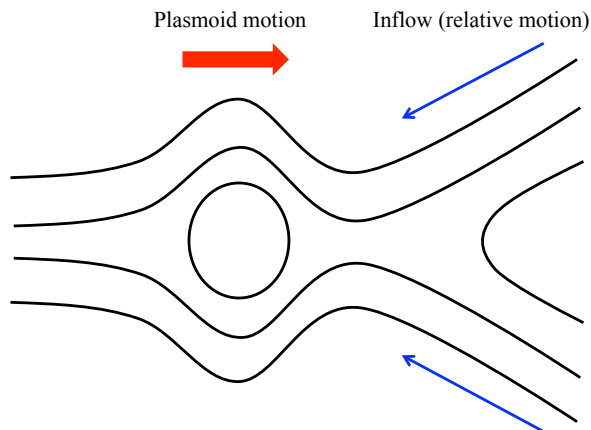


Figure 8.1

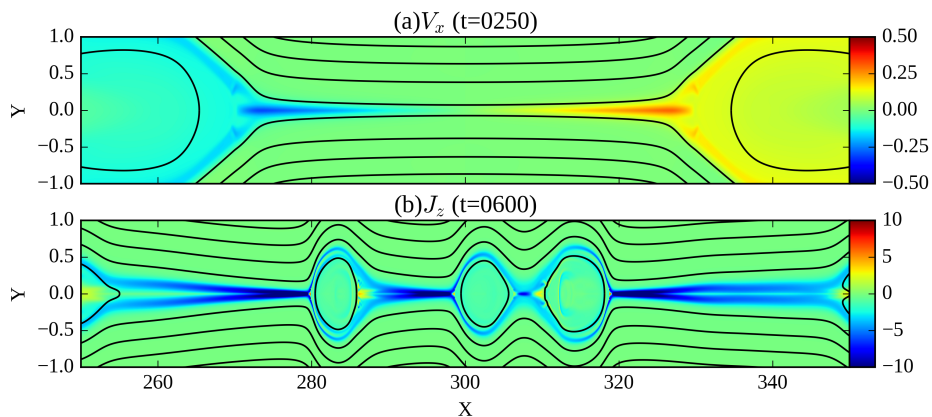


Figure 8.2: (a) Initial Sweet-Parker outflow from a high-Lundquist number simulation [Shibayama et al. \(2015\)](#). (b) Plasmoids and Petschek-type current structure formed in the outflow.

In the local model, asymmetry between diffusion regions grows as a result of the initial and boundary conditions. In general, this asymmetry can be initiated and sustained for several reasons, e.g., initial or boundary conditions, unidirectional flow or plasmoid motion. A similar process also occurs in plasmoid reconnection at high Lundquist numbers [Shibayama](#)

et al. (2015). Fig.8.2 shows the outward flow velocity and current density before and after the formation of plasmoids under the simulation at $S_0 = 10^4$ in Shibayama et al. (2015). A chain of three plasmoids is visible, with Petschek-type structures forming on both sides of the plasmoid chain at around $x = 280$ and 320 , although not on both sides of all plasmoids. In this case, the plasma flow serves as the origin of asymmetry. Prior to formation of the plasmoids (Fig.8.2(a)), a Sweet-Parker reconnection region is present. Although the outward flow structure is globally symmetric, when the plasmoids form within the system the flow in the current sheet is directed to either the left or the right. In this case, the downstream side of the plasmoids are preferable for the formation of Petschek-type diffusion regions (Fig.8.2(b)). In the frame of reference of the plasmoid, the ambient plasma is flowing against the plasmoid in the downstream side. This opposing flow strengthens the ideal term of Eq.5.7 and facilitates the localization of the diffusion region. The opposing flow also affects the reconnection rate, which is 0.008 in this paper and 0.02 in our previous results. This effect, which is caused by the asymmetry in the x -direction, is a candidate of the reason explaining the difference of reconnection rate. By contrast in the upstream side, the ambient flow weakens the localization of the diffusion region. From Fig.8.2(b) it is also seen that the curvature radius of the magnetic field at around $x = 280$ is smaller on the left-hand side of the nearby plasmoid because the leftward motion of the plasmoid leads to a steepening of the left-hand face of the plasmoid. These are plausible explanations for the appearance of a Petschek-type structure at only the left-hand side of the plasmoid.

We fixed a plasmoid with boundary condition in local model, by contrast in global model, it is seen from Fig.4.4 that plasmoid moves. As reconnection proceeds, outflow from Petschek-type diffusion region pushes plasmoid away. As a result, plasmoids with Petschek-type structure shows typical turn over motion. These three plasmoids and neighboring Petschek-type diffusion region drive fast reconnection for some period but these three plasmoids eventually collide and fast reconnection is terminated until the next plasmoids and Petschek-type diffusion region appear. Quasi-periodic modulation of reconnection rate is generated by a sequence of formation and coalescence of plasmoids.

8.2 Observation of Magnetic Reconnection in the Solar Corona

We proposed non-steady reconnection model which include small Petschek-type diffusion regions raise reconnection rate in Sec.4 and 5. In this section, we discuss possible contributions from solar physics to plasma physics. Observation of the solar corona is conducted using electromagnetic wave emission from heavy ions such as iron. As we discussed in Sec.6 ,since it takes on the order of 100 seconds to reach ionization equilibrium of iron, information from emission lines do not necessarily reflect the parameters of plasma. Fig.6.7 shows that dynamical Petschek structure is difficult to observe directly from ion distribution. By contrast, we may derive more information from emission lines such as the history of plasma heating. If

there is a gradient of elapsed time after heating in the space between plasmoids, this suggests diffusion region, where heating occurs, is localized in a part the space. Although it is difficult to resolve plasmoids and diffusion, this method using ionization process may infer the heating history of unresolved structure. We can discuss the local information of reconnection process. Fig.6.4 shows sensitive ion pair in different elapsed time after heating. Although we need to assume upstream parameter and characteristics of heating, we can analyse the intermittency of heating event using this property. Comparing this analysis with the results of Fig.4.1, we can discuss the dynamical property of plasmoid motion.

The other important effect of observation is the line-of-sight integration due to the optically thin character of coronal plasma. It is shown in Sec.7 that internal structure of current sheet is averaged out and not observed depending on the direction of the observation. Although recent discussion on onset of reconnection is mainly based on two-dimensional theory of magnetic reconnection, our numerical simulation of three-dimensional system shows structure formation of three-dimensional modes. Such modes should be taken into account for the discussion of onset of magnetic reconnection. Related to the discussion in the previous paragraph, it should be possible to analyse the statistical property of heating history even after the line-of-sight integration. Statistics such as size distribution of plasmoid and change in heating rate are important information for reconnection theory. Providing such observational constraints to the theory, solar physics will have a significant contribution to plasma physics.

9 Conclusion

Using large-scale MHD numerical simulation, we demonstrate that Petschek-type small diffusion regions spontaneously appear in the dynamic evolution of plasmoid reconnection even under uniform resistivity. Petschek-type reconnection is previously considered to be impossible to realize in a system with uniform resistivity due to the lack of localization mechanism of diffusion region. This regime appear especially in high Lundquist number case. The reconnection rate is almost independent on Lundquist number.

We further construct a model of the elementary process of the Petschek-type diffusion region formation to reveal the mechanism of the localization of diffusion region. We successfully find an initial condition to reproduce a single Petschek-type diffusion region associated with a plasmoid. For the localization, the separation of the magnetic null point and flow stagnation point plays an important role. The reconnection rate in the large-scale simulation is independent on Lundquist number because the similar diffusion-scale process realize in systems with different Lundquist number. According to these results, we propose the *dynamical Petschek reconnection* regime, in which small Petschek-type diffusion regions appear in close contact with the ends of plasmoids and drive fast reconnection. In plasmoid reconnection model, it is believed that reconnection rate is 0.01 because it corresponds to the rate of critical diffusion region. By contrast in our model, reconnection rate is determined by the localized diffusion region of dynamical Petschek. Motion of plasmoid further increases the reconnection rate in the leading side of the plasmoid.

For applying of our reconnection model to the observation of solar flares, we developed numerical solver of ionization process of Fe ions. We performed MHD numerical simulation of plasmoid reconnection along with ionization process for the first time, and pointed out that there is a threshold of plasmoid area under which we can not use an assumption of ionization equilibrium. Although dynamical Petschek structure appeared in the simulation, it was difficult to observe the heated plasma in the outflow region directly from Fe distribution because plasma does not stay long time there. We pointed out that there is a possibility that we can analyse the history of heating using different pairs of ions, which have different sensitivity to the elapsed time after the heating. This method can be also applied to unresolved or line-of-sight integrated observation to derive the statistical property. Using next-generation satellite Solar-C.EUVST and our method, we may obtain the detailed information of magnetic reconnection process such as a history of heating or size distribution of plasmoids, which are important information for basic plasma physics.

We also performed largest three-dimensional MHD simulation of current sheet, whose Lundquist number is more than 10^6 , and reconfirmed that oblique tearing instability dominate the system. In the observation of the solar corona, there is an effect of line-of-sight integration, which is similar to the mean field approach of three-dimensional system. We

demonstrated that observability of plasmoid depends on the line-of-sight direction. The qualitative characteristics of mean field Ohm's law is different from previous 3D simulation with lower Lundquist number. We do not find the evolution of Petschek-type diffusion region in the 3D current sheet. However, the Lundquist number of the three-dimensional simulation is smaller than that of two-dimensional models due to the limitation of computational power. If the separation of reconnection point and flow stagnation point sufficiently evolve in a larger system, it is possible that the motion of X-point is restricted and the diffusion region is localized in the same way as two-dimensional case.

Acknowledgement

Firstly, I would like to express my sincere gratitude to my advisor Prof. Kanya Kusano for the continuous support of my Ph.D study and related research, for his patience, motivation, and immense knowledge. His guidance helped me in all the time of research and writing of this thesis. Besides my advisor, I would like to thank the rest of my thesis committee: Prof. Tomohiko Watanabe, Dr. Takaaki Yokoyama, and Dr. Takayuki Umeda, for their insightful comments and encouragement, but also for the hard question which incited me to widen my research from various perspectives. My sincere thanks also goes to Dr. Takahiro Miyoshi, Dr. Grigory Vekstein, Dr. Amitava Bhattacharjee, and Dr. Shinsuke Imada who provided me an opportunity to join their team as a collaborator. Without their precious support it would not be possible to conduct this research. I thank all the lab members for the stimulating discussions. I'd like to thank also secretaries and technician of the lab for supporting daily life and maintaining the research environment such as computers of the lab. The research is conducted by using the K computer at the RIKEN Advanced Institute for Computational Science, FX100 supercomputer system at the Information Technology Center, Nagoya University, also on the Earth Simulator with the support of JAMSTEC. Most of the data analysis is performed using the computational resource of the Center for Integrated Data Science, Institute for Space-Earth Environmental Research, Nagoya University. Last but not the least, I would like to thank my family: my parents and my sister for supporting me spiritually throughout writing this thesis and my life in general.

References

- M. Arnaud and J. Raymond. Iron ionization and recombination rates and ionization equilibrium. *Astrophysical Journal*, 398:394–406, October 1992. doi:[10.1086/171864](https://doi.org/10.1086/171864).
- M. Arnaud and R. Rothenflug. An updated evaluation of recombination and ionization rates. *Astronomy and Astrophysics Supplement Series*, 60:425–457, June 1985. URL <http://adsabs.harvard.edu/abs/1985A%26AS...60..425A>.
- M.-J. Aschwanden. *Physics of the Solar Corona. An Introduction*. Praxis Publishing Ltd, August 2004.
- S.-D. Baalrud, A. Bhattacharjee, and Y.-M. Huang. Reduced magnetohydrodynamic theory of oblique plasmoid instabilities. *Physics of Plasmas*, 19(2):022101, February 2012. doi:[10.1063/1.3678211](https://doi.org/10.1063/1.3678211).
- H. Baty. On the onset of the plasmoid instability. *Physics of Plasmas*, 19(9):092110, September 2012. doi:[10.1063/1.4752744](https://doi.org/10.1063/1.4752744).
- H. Baty, E.-R. Priest, and T.-G. Forbes. Petschek-like reconnection with uniform resistivity. *Physics of Plasmas*, 16(6):060701, June 2009. doi:[10.1063/1.3155087](https://doi.org/10.1063/1.3155087).
- H. Baty, T.-G. Forbes, and E.-R. Priest. The formation and stability of Petschek reconnection. *Physics of Plasmas*, 21(11):112111, November 2014. doi:[10.1063/1.4901918](https://doi.org/10.1063/1.4901918).
- A. Bhattacharjee, Y.-M. Huang, H. Yang, and B. Rogers. Fast reconnection in high-Lundquist-number plasmas due to the plasmoid instability. *Physics of Plasmas*, 16(11):112102, November 2009. doi:[10.1063/1.3264103](https://doi.org/10.1063/1.3264103).
- J. Birn, J.-F. Drake, M.-A. Shay, B.-N. Rogers, R.-E. Denton, M. Hesse, M. Kuznetsova, Z.-W. Ma, A. Bhattacharjee, A. Otto, and P.-L. Pritchett. Geospace Environmental Modeling (GEM) magnetic reconnection challenge. *Journal of Geophysical Research*, 106:3715–3720, March 2001. doi:[10.1029/1999JA900449](https://doi.org/10.1029/1999JA900449).
- J. Braithwaite. The stability of toroidal fields in stars. *Astronomy and Astrophysics*, 453:687–698, July 2006. doi:[10.1051/0004-6361:20041282](https://doi.org/10.1051/0004-6361:20041282).
- L. Comisso and F.-A. Asenjo. Thermal-Inertial Effects on Magnetic Reconnection in Relativistic Pair Plasmas. *Physical Review Letters*, 113(4):045001, July 2014. doi:[10.1103/PhysRevLett.113.045001](https://doi.org/10.1103/PhysRevLett.113.045001).
- T.-G. Forbes, E.-R. Priest, D.-B. Seaton, and Y.-E. Litvinenko. Indeterminacy and instability in Petschek reconnection. *Physics of Plasmas*, 20(5):052902, May 2013. doi:[10.1063/1.4804337](https://doi.org/10.1063/1.4804337).
- H.-P. Furth, J. Killeen, and M.-N. Rosenbluth. Finite-Resistivity Instabilities of a Sheet Pinch. *Physics of Fluids*, 6:459–484, April 1963. doi:[10.1063/1.1706761](https://doi.org/10.1063/1.1706761).
- E.-G. Harris. On a plasma sheath separating regions of oppositely directed magnetic field. *Il Nuovo Cimento*, 23:115–121, 1962. doi:[10.1007/BF02733547](https://doi.org/10.1007/BF02733547). URL <http://link.springer.com/article/10.1007/2FBF02733547>.
- T. Hayashi and T. Sato. Magnetic reconnection - Acceleration, heating, and shock formation. *Journal of Geophysical Research*, 83:217–220, January 1978. doi:[10.1029/JA083iA01p00217](https://doi.org/10.1029/JA083iA01p00217).
- Y.-M. Huang and A. Bhattacharjee. Scaling laws of resistive magnetohydrodynamic reconnection in the high-Lundquist-number, plasmoid-unstable regime. *Physics of Plasmas*, 17(6):062104, June 2010. doi:[10.1063/1.3420208](https://doi.org/10.1063/1.3420208).

- Y.-M. Huang and A. Bhattacharjee. Turbulent Magnetohydrodynamic Reconnection Mediated by the Plasmoid Instability. *Astrophysical Journal*, 818:20, February 2016. doi:[10.3847/0004-637X/818/1/20](https://doi.org/10.3847/0004-637X/818/1/20).
- S. Imada, I. Murakami, T. Watanabe, H. Hara, and T. Shimizu. Magnetic Reconnection in Non-equilibrium Ionization Plasma. *Astrophysical Journal*, 742:70, December 2011. doi:[10.1088/0004-637X/742/2/70](https://doi.org/10.1088/0004-637X/742/2/70).
- H. Isobe, H. Takasaki, and K. Shibata. Measurement of the Energy Release Rate and the Reconnection Rate in Solar Flares. *Astrophysical Journal*, 632:1184–1195, October 2005. doi:[10.1086/444490](https://doi.org/10.1086/444490).
- H. Ji and W. Daughton. Phase diagram for magnetic reconnection in heliophysical, astrophysical, and laboratory plasmas. *Physics of Plasmas*, 18(11):111207, November 2011. doi:[10.1063/1.3647505](https://doi.org/10.1063/1.3647505).
- R.-M. Kulsrud. Magnetic reconnection: Sweet-Parker versus Petschek. *Earth, Planets, and Space*, 53:417–422, June 2001. doi:[10.1186/BF03353251](https://doi.org/10.1186/BF03353251).
- R.-M. Kulsrud. Intuitive approach to magnetic reconnection. *Physics of Plasmas*, 18(11):111201, November 2011. doi:[10.1063/1.3628312](https://doi.org/10.1063/1.3628312).
- G. Lapenta. Self-Feeding Turbulent Magnetic Reconnection on Macroscopic Scales. *Physical Review Letters*, 100(23):235001, June 2008. doi:[10.1103/PhysRevLett.100.235001](https://doi.org/10.1103/PhysRevLett.100.235001).
- N.-F. Loureiro, A.-A. Schekochihin, and S.-C. Cowley. Instability of current sheets and formation of plasmoid chains. *Physics of Plasmas*, 14(10):100703, October 2007. doi:[10.1063/1.2783986](https://doi.org/10.1063/1.2783986).
- P. Mazzotta, G. Mazzitelli, S. Colafrancesco, and N. Vittorio. Ionization balance for optically thin plasmas: Rate coefficients for all atoms and ions of the elements H to NI. *Astronomy and Astrophysics Supplement Series*, 133:403–409, December 1998. doi:[10.1051/aas:1998330](https://doi.org/10.1051/aas:1998330).
- T. Miyoshi and K. Kusano. A multi-state HLL approximate Riemann solver for ideal magnetohydrodynamics. *Journal of Computational Physics*, 208:315–344, September 2005. doi:[10.1016/j.jcp.2005.02.017](https://doi.org/10.1016/j.jcp.2005.02.017).
- T. Miyoshi and K. Kusano. A Comparative Study of Divergence-Cleaning Techniques for Multi-Dimensional MHD Schemes. *Plasma and Fusion Research*, 6:1124, August 2011. doi:[10.1585/pfr.6.2401124](https://doi.org/10.1585/pfr.6.2401124).
- N. A. Murphy. Resistive magnetohydrodynamic simulations of X-line retreat during magnetic reconnection. *Physics of Plasmas*, 17(11):112310–112310, November 2010. doi:[10.1063/1.3494570](https://doi.org/10.1063/1.3494570).
- S.-y. Nitta. Continuous Transition from Fast Magnetic Reconnection to Slow Reconnection and Change of the Reconnection System Structure. *Astrophysical Journal*, 663:610–624, July 2007. doi:[10.1086/518104](https://doi.org/10.1086/518104).
- J.-S. Oishi, M.-M. Mac Low, D.-C. Collins, and M. Tamura. Self-generated Turbulence in Magnetic Reconnection. *Astrophysical Journal Letter*, 806:L12, June 2015. doi:[10.1088/2041-8205/806/1/L12](https://doi.org/10.1088/2041-8205/806/1/L12).
- E.-N. Parker. Sweet’s Mechanism for Merging Magnetic Fields in Conducting Fluids. *Journal of Geophysical Research*, 62:509–520, December 1957. doi:[10.1029/JZ062i004p00509](https://doi.org/10.1029/JZ062i004p00509).
- H.-E. Petschek. Magnetic Field Annihilation. *NASA Special Publication*, 50:425, 1964.
- E. R. Priest and T. G. Forbes. New models for fast steady state magnetic reconnection. *Journal of Geophysical Research*, 91:5579–5588, May 1986. doi:[10.1029/JA091iA05p05579](https://doi.org/10.1029/JA091iA05p05579).
- R. Samtaney, N.-F. Loureiro, D.-A. Uzdensky, A.-A. Schekochihin, and S.-C. Cowley. Formation of Plasmoid Chains in Magnetic Reconnection. *Physical Review Letters*, 103(10):105004, September 2009. doi:[10.1103/PhysRevLett.103.105004](https://doi.org/10.1103/PhysRevLett.103.105004).

- C. Shen, K. K. Reeves, J. C. Raymond, N. A. Murphy, Y.-K. Ko, J. Lin, Z. Mikić, and J. A. Linker. Non-equilibrium Ionization Modeling of the Current Sheet in a Simulated Solar Eruption. *Astrophysical Journal*, 773:110, August 2013. doi:[10.1088/0004-637X/773/2/110](https://doi.org/10.1088/0004-637X/773/2/110).
- K. Shibata and S. Tanuma. Plasmoid-induced-reconnection and fractal reconnection. *Earth, Planets, and Space*, 53:473–482, June 2001. doi:[10.1186/BF03353258](https://doi.org/10.1186/BF03353258).
- T. Shibayama, K. Kusano, T. Miyoshi, T. Nakabou, and G. Vekstein. Fast magnetic reconnection supported by sporadic small-scale Petschek-type shocks. *Physics of Plasmas*, 22(10):100706, October 2015. doi:[10.1063/1.4934652](https://doi.org/10.1063/1.4934652).
- B. U. Ö. Sonnerup. Magnetic-field re-connexion in a highly conducting incompressible fluid. *Journal of Plasma Physics*, 4:161–174, February 1970. doi:[10.1017/S0022377800004888](https://doi.org/10.1017/S0022377800004888).
- P.-A. Sweet. The Neutral Point Theory of Solar Flares. In B. Lehnert, editor, *Electromagnetic Phenomena in Cosmical Physics*, volume 6 of *IAU Symposium*, page 123, 1958.
- T. Tajima and K. Shibata, editors. *Plasma astrophysics*, 1997.
- S. Takasao, A. Asai, H. Isobe, and K. Shibata. Simultaneous Observation of Reconnection Inflow and Outflow Associated with the 2010 August 18 Solar Flare. *Astrophysical Journal Letter*, 745:L6, January 2012. doi:[10.1088/2041-8205/745/1/L6](https://doi.org/10.1088/2041-8205/745/1/L6).
- M. Ugai and T. Tsuda. Magnetic field-line reconnection by localized enhancement of resistivity. I - Evolution in a compressible MHD fluid. *Journal of Plasma Physics*, 17:337–356, June 1977. doi:[10.1017/S0022377800020663](https://doi.org/10.1017/S0022377800020663).
- D.-A. Uzdensky, N.-F. Loureiro, and A.-A. Schekochihin. Fast Magnetic Reconnection in the Plasmoid-Dominated Regime. *Physical Review Letters*, 105(23):235002, December 2010. doi:[10.1103/PhysRevLett.105.235002](https://doi.org/10.1103/PhysRevLett.105.235002).
- M. Yamada, R. Kulsrud, and H. Ji. Magnetic reconnection. *Reviews of Modern Physics*, 82:603–664, January 2010. doi:[10.1103/RevModPhys.82.603](https://doi.org/10.1103/RevModPhys.82.603).
- M. Yan, L. C. Lee, and E. R. Priest. Fast magnetic reconnection with small shock angles. *Journal of Geophysical Research*, 97:8277–8293, June 1992. doi:[10.1029/92JA00170](https://doi.org/10.1029/92JA00170).
- T. Yokoyama, K. Akita, T. Morimoto, K. Inoue, and J. Newmark. Clear Evidence of Reconnection Inflow of a Solar Flare. *Astrophysical Journal Letter*, 546:L69–L72, January 2001. doi:[10.1086/318053](https://doi.org/10.1086/318053).
- S. Zenitani and T. Miyoshi. Magnetohydrodynamic structure of a plasmoid in fast reconnection in low-beta plasmas. *Physics of Plasmas*, 18(2):022105–022105, February 2011. doi:[10.1063/1.3554655](https://doi.org/10.1063/1.3554655).

Supplementary Papers

1. Shibayama, T., Kusano, K., Miyoshi, T., Nakabou, T., Vekstein, G. (2015), Fast magnetic reconnection supported by sporadic small-scale Petschek-type shocks., *Physics of Plasmas*, **22**, 10, 100706
2. Shibayama, T., Kusano, K., Miyoshi, Bhattacharjee, A. (2019), Mechanism of Non-Steady Petschek-Type Reconnection with Uniform Resistivity. , submitted